DESIGN AND DEVELOPMENT OF NANOPARTICLES FOR IMAGING AND X-RAY INDUCED PHOTODYNAMIC THERAPY

by

GEOFFREY Dong Song WANG

(Under the Direction of JIN XIE)

ABSTRACT

The development of nanomaterials and nanosystems for biomedical applications is an area of considerable current interest in chemistry, materials science, and medicine. The basic rationale is that nanometer-sized particles have unique optical, electronic, or magnetic properties that are not available from either discrete molecules or bulk solids. Also, nanosized structures or scaffolds are well suited for covalent attachment and/or noncovalent encapsulation of multiple diagnostic and therapeutic agents, leading to theranostic (both therapy and diagnostic) and related multi-modal systems. In this context, the primary objective of this dissertation was to design and develop innovative nanoparticles for cancer imaging and therapy. For optical and MRI cancer imaging, we have developed dual-modality inorganic/organic nanostructures by embedding gadolinium (a magnetic contrast agent) into fluorescent carbon dots or europium-doped metal-organic frameworks (MOF). These nanoparticle probes show excellent in-vivo stability, strong fluorescence emission and improved magnetic contrast, moreover the gadolinium carbon dots are small enough (about 12 nm in diameter) for rapid renal clearance. For cancer therapy, we have developed x-ray induced photodynamic nanoparticles by coating a nanoscintilator core with mesoporpous silica and photosensitizers. In comparison with traditional

photodynamic therapy (PDT), the use of x-ray to activate photosensitizing drugs allows greater tissue penetration and photodynamic treatment of deeply buried tumors. Also, in-vivo therapeutic studies using orthotopic cancer models have shown that x-ray induced PDT is a combination of photodynamic therapy and radiotherapy that synergistically target the cellular membrane and cellular DNA. Taken together, these findings provide important insights into the design and development of multi-modal nanoparticles for cancer molecular imaging and targeted therapy.

INDEX WORDS: Cancer, Contrast Agent, Fluorescence, Gadolinium, Imaging, Metal-Organic Framework (MOF), Magnetic Resonance Imaging (MRI), Multi-Modal, Nanomedicine, Nanoscintillator, X-Ray Induced Photodynamic Therapy

DESIGN AND DEVELOPMENT OF NANOPARTICLES FOR IMAGING AND X-RAY INDUCED PHOTODYNAMIC THERAPY

by

GEOFFREY D. S. WANG

B.S., GEORGIA INSTITUTE OF TECHNOLOGY, 2001

M.S., GEORGIA INSTITUTE OF TECHNOLOGY, 2006

A Dissertation Submitted to the Graduate Faculty of The University of Georgia in Partial Fulfillment of the Requirements for the Degree

DOCTOR OF PHYLOSOPHY

ATHENS, GEORGIA

April, 2017

DESIGN AND DEVELOPMENT OF NANOPARTICLES FOR IMAGING AND X-RAY INDUCED PHOTODYNAMIC THERAPY

by

GEOFFREY D. S. WANG

Major Professor: JIN XIE

Committee: JIANFU CHEN

JASON LOCKLIN

Electronic Version Approved:

Suzanne Barbour
Dean of the Graduate School
The University of Georgia
May 2017

DEDICATION

TO

My father Professor Youqi Wang

My mother Dr. Yunzhi Li

For their love and faith in me

ACKNOWLEDGEMENTS

I greatly appreciate Professor Jin Xie for serving as my PhD advisor. His vision, high standard, and guidance have enabled me to improve my research ability, and to become who I am today. I am also truly grateful for my doctoral committee members, Professor Jianfu (Jeff) Chen and Professor Jason Lockli, who discussed with me about my project whenever I needed. A special thank goes to Dr. Hongmin Chen, who I enjoy working closely over the past five years day and night in the chemistry or the animal labs.

I would like to thank my colleagues Dr. Zipeng Zhen, Dr. Trever Todd, Dr. Wei Tang, and Dr. Taku Cowger for collaboration on various projects, and many members from the University of Georgia and the Augusta University – Drs. Aaron Beedle, Khan Hekmatyar, Richard B. Hubbard, Koichi Nagata, Ha Nguyen, John Stickney, Chu Tsang, Lianchun Wang, Zhonglin Hao and Jianyue Jin and my student Phillip Cox.

My sincere thanks go to the Department of Chemistry who have provided financial support during my PhD study; and to our friendly staffs, Lauren Bowman, Kristie Huff, Genet Kibreab, Kistie Manders and many others who helped me solve many problems along the way.

I would like to acknowledge several friends, Robert Gilliard, Gloria Heard and Hui Tang, for sharing their wisdom during lunch breaks.

I would like to thank all my family members for their unconditional love and support. Specifically, I want to thank my wife Ha Nguyen who went through the entire PhD journey together with me and received her own PhD, and my son Richard Wang who brought so much joy and hope.

TABLE OF CONTENTS

Page

LIST OF FIGURES

Page

CHAPTER 1

INTRODUCTION

Purposes of the Study

The primary objective of this research was to design and develop novel nanoparticles for cancer imaging and therapy. In comparison with individual molecules or bulk solids, materials on the nanoscale often exhibit unique physical, optical, electrical, or magnetic properties such as quantum size confinement and superparamagnetism. Recent advances have led to the development of advanced nanomaterials for agricultural [3, 4], biomedical [5, 6], renewable energy [6, 7] and environmental [8, 9] applications. The rapid development of novel nanomaterials is also bringing major benefits to biology and medicine. Fundamental biological units range from a few to a few hundred nanometers, such as DNA polymerases (about 7 nm in size), double stranded DNA (3.4 nm per turn), and the influenza virus (about 100 nm) [10]. Indeed, the integration of nanomaterials with biology and medicine has resulted in the creation of nanomedicine where it applies nanoscience and nanotechnology (the engineering of tiny nanoparticles) to the prevention and treatment of disease in the human body. This evolving discipline has brought dramatic changes in the medical science, such as disease diagnosis, targeted drug delivery, and cancer therapy. Towards these goals, this dissertation aims to design and develop innovative nanoparticles based on inorganic/organic materials for cancer imaging and therapeutic applications.

Background

Cancer and cancer treatment

Cancer, or malignant neoplasms, is a major public health problem worldwide and continues to be one of most common diseases that lead to death among adult worldwide. The estimated cancer led deaths in 2012 were about 8.2 million by world health organization [11]. From 1930 to 2012, in U.S. alone, mortalities (male only) resulted from the advanced tumors have remained unchanged for colorectal, liver and prostate cancer, have increased slightly for leukemia and pancreatic cancer while have boosted dramatically for lung and bronchus cancer [12]. These are the results from the advanced forms of tumors. Therapeutic success of cancer highly relies on early detection and efficient treatment through various stages of tumor progression. Most cancer diagnoses are carried out by physical examination, biopsy, and diagnostic imaging. Subsequently the traditional treatment strategies, surgery, chemotherapy and radiotherapy are applied. However, overall progresses in treating cancers have been slow, and major advancement in the future can only come from more efficient diagnosis and novel therapeutics.

Applications of nanotechnology principles on cancer diagnosis and therapy could offer profound transformative potentials that allow the detection of cancers at early stage and provide new therapy regimen. Remarkable progresses have been made in nanomedicine, and have helped improving the imaging contrast and cancer treatment regimens. To facilitate the design of the clinical applicable cancer imaging contrast agents with minimal toxicity and/or the noninvasive therapeutic agent with enhanced treatment effect, the MRI imaging, photodynamic therapy and related nanocomposites will be briefly described here.

MRI imaging

As a noninvasive and real-time diagnosis imaging modality, magnetic resonance imaging (MRI) has attracted enormous attentions. Since Damadian discovered the signal relaxation time differences between the healthy tissue and cancerous tissues [13], the research on the MRI contrast imaging have grown dramatically. For medical diagnosis, MRI makes use of hydrogen nuclei (proton) from the watery content (around 60% of human body) in human. When patient's body is immersed into the strong static homogenous magnetic field, generated by the permanent magnet, it excites hydrogen nuclei spins with the Larmor precession (corresponding to the magnetic field). When the external radio wave (energy) is applied perpendicular to the magnetic field, the Larmor precession is perturbed. After the external radio wave is removed, the protons will re-align to the magnetic field and emit radio-frequency signals. These radio wave signals from emitted from hydrogen nuclei can be recognized by the field sensors as MR signals, and tissue images can be constructed by interpretation of these radio wave signals. The generated MR signals represent the proton density level and ability to fall back (relaxation) to the ground state in the 3D space (body tissues). How the protons relax back to its Larmor precession alignment can be used to generate diagnostics images of body with the resolution of up-to 500nm. Macroscopically, relaxation can be measured in the longitudinal return in the direction of main magnetic field and transverse return in the perpendicular direction of main magnetic field. The longitudinal relaxation is defined as T_1 and the transverse relaxation is defined as T_2. T_1, correlates to the interaction between the proton and its local surroundings, is time required for the magnetization vector to recover to 63% of its original state, also is called spin-lattice relaxation. Spins are 96% relaxed after three T_1 periods. T_2, correlates to phase coherence loss after excitation, is time required for the transverse magnetization decay/dephase to 37% of its

original signal where energy may or may not transport to the surroundings. Surroundings of the proton contribute to the static local field disturbance and in turn also contribute to the MRI tissue imaging.

Factors involving in the enhancement of the relaxation include intrinsic tissue T_1 and T_2 relaxation properties, radiofrequency waveform and proton density in tissues. While coping with pulses sequence and gradient waveform can improve the MRI imaging keenness, it is of general interests to improve the imaging contrast with contrast agents instead.

Image contrast is generated by discrimination of healthy tissues and cancer tissues based on the richness of the watery (hydrogen) contents where tumors generate more signals from more water content. However, the differentiation of the MRI imaging without the contrast agents cannot resolute the similarities of the relaxation between healthy tissues and tumors. The contrast agents generally stimulate the recovery process for the proton to return to its ground state that distinct the signal-to-noise ratio, such as paramagnetic ions (ions with unpaired electrons or paramagnetic species) facilitate the proton ions to return to the ground state faster than the surrounding water molecules, but they will not generate the signal themselves, such as, paramagnetic contrast agents generate a magnetic field can be one thousand times stronger than water protons. In the biological environment, the addition of a paramagnetic solute increases both $1/T_1$ and $1/T_2$ relaxation rates [14-16] and in turns increase the observable solvent relaxation $(1/T_i)$obs, such as,

$$1/(1/T_i)_{obs} = 1/(1/T_i)_d + 1/(1/T_i)_p \qquad (i = 1,2)$$

where d and p represent diamagnetic contribution and paramagnetic contribution, respectively [14]. In the absence of interactions between solutes, the solvent relaxation rate is directly proportional to the paramagnetic agent concentration, such as,

$$1/(1/T_i)_{obs} = 1/(1/T_i)_d + R_i\,[C] \qquad (i = 1,2)$$

where R_i is the relaxivity of the paramagnetic species with units of $mM^{-1}s^{-1}$ and [C] is the concentration of paramagnetic species. There are two types of MRI contrast agents, T_1 contrast agents, such as Gd(III) chelating agents, and T_2 contrast agents, such as supermagnetic iron oxide.

Gadolinium T_1 contrast agent and synthesis

Typical paramagnetic contrast agents could be synthesized from the elements in the lanthanides group, such as the chelates of paramagnetic elements in this group. There are 15 elements located in the sixth period and IIIB group with the electronic configuration of $[Xe]4f^{n-1}5d^{0-1}6s^2$ where the elements with unpaired electrons occupied on the 4f orbitals that provide peculiar angular momentum. This especially applicable for trivalent gadolinium ions (Gd^{3+}) in a stable oxidation state who has isotropic electron ground state with 7 unpaired electrons providing weak spin–orbit coupling and thus long relaxation properties, about 4 to 5 folds of other Lanthanide elements [17]. Clinically the chelating agents are used to stabilize the toxic Gd^{3+} ions. Due to rigid crystalline structure and high payload Gd ions, the Gd^{3+} chelates present high local T_1 contrast [18]. There are more than one hundred T_1 (Gd) contrast agents that their pharmacokinetic responses are directly related to the particle size and surface characteristics [19, 20]. Gd(III) based nanocomposites can provide a platform facile surface modification.

Gd^{3+} based nanoparticles are prepared mainly by the wet chemical based synthesis (wet chemistry) methods. The wet chemical synthesis methods can be optimized by altering the precursors' concentration, pH, surfactants and temperature to obtain the desired morphology, size and structures. Wet chemical synthesis methods include hydrothermal/solvothermal method, precipitation/coprecipitation method, microwave and microemulsion-assisted synthesis, thermal

decomposition and etc. Among these synthesis approaches, thermal decomposition and hydrothermal/solvothermal methods are the most popular ones.

Precipitation/Coprecipitation method: Precipitation and coprecipitation reaction is a classical wet chemical synthetic method where several ions are mixed together simultaneously for precipitation into nanoparticles. However, different precipitation rate of difference ions will bring out diverse results. In general, additional coordinating surfactants and cosolvents will be added to the reaction for synchronicity of coprecipitation process. The reaction can be carried out in the aqueous solution and organic solution.

Hydrothermal/Solvothermal method: The hydrothermal/solvothermal synthesis are the reaction $Gd^{(III)}$ precursors in the superheated solvents with high pressure autoclaves that are generally resulted in good crystallinity with good solubility and reactivity. The precursors include Gd^{3+}-based oxides, chlorides, nitrates, and acetylacetonates.

Thermal Decomposition method: In general, thermal decomposition starts with decomposition of the Gd^{3+}-based organic salts as precursors in high-boiling-point organic solvents in the oxygen-free environment where octadecene is the common high-boiling-point organic solvents. Oleic (carboxylic group) acid and oleylamine (amine group) can be used to control the size and morphology of nanoparticles by adsorption. As the temperature elevates, C–F bond break and nucleation could happen toward target nanoparticles. In general, the crystal nucleation and growth processes can be manipulated by modulating the reaction parameters such as the concentration of precursors, heating steps and temperature to initialize the nucleation and from uniform nanoparticles. This method can produce very monodispersed nanoparticles with narrow size distribution.

Other Synthetic Procedures: There are additional synthesis methods of Ga^{3+} nanoparticles such as ionic liquid-based synthesis, microemulsion-based and microwave-assisted synthesis.

Photodynamic Therapy and X-ray induced Photodynamic Therapy

Photodynamic therapy (PDT) is a noninvasive medical treatment modality that generates reactive oxygen species to kill the cancer cells. PDT induces low systematic toxicity with little intrinsic or acquired resistance [21-23]. It consists of three essential components: light, oxygen, and photosensitizers. Often the vascularization of solid tumors have the unevenly developed proliferating endothelial cell layers with irregular basement membrane that result in enhanced permeability and retention (EPR) effect [24]. Photosensitizers are pharmacologically inactive without illumination, can be retained in the tumor tissues due to EPR effect, and can be activated by light. The mechanism of PDT involves activation of the ground state photosensitizer, after it absorbs a photon energy, the photosensitizer will be escalate to a triple state level, then transfer energy to nearby oxygen molecules. In turn, it can either go through an electron transfer process to generate cytotoxic reactive oxygen species (ROS), or most importantly, an energy transfer process with an oxygen molecule to generate singlet oxygen ($^1O_2$). Singlet oxygen is a higher energy state of molecular oxygen. Singlet oxygens can oxidize the amino acids, such as histidine, and damage proteins thus in turn destroy many enzymes. Subsequently, they halt the cellular function and result in cell death.

Traditional light source utilizes laser, the tumor region is illuminated with the laser emission wavelength coincides with the photosensitizer absorption peak. However, for the first generation of PDT, such as Photofrin, the patients suffered from prolonged skin photosensitivity with limited light penetration depth (up to 1cm) and the inability to treat widely disseminated disease. Tumor ablation will generally happen in a few days. Even though additional light

sources have been used, such as xenon arc lamps or slide projectors equipped with red filters, lasers and LEDs [25-27], the major limitations of treatment depth due to light penetration limitations cannot be overcome. Nevertheless, X-Ray has known good penetration depth. Mediating by the scintillator materials, X-ray could provide new light source to overcome the PDT limitations.

X-radiation is a form of electromagnetic radiation that when high energy electrons collide with an electron from inside orbitals of the element, they are ejected from the atom leaving empty orbitals in the inner atom shell. In turn, the outer orbital electrons move into inner orbital, the energy differences are emitted as X-ray photons. X-ray and scintillator materials have been used in the medical imaging diagnostic field for ages. When they are irradiated by the X-ray, scintillator materials can release photon with visible wavelength and qualify it as a light source for the photosensitizer. There are plenty known photosensitizers that can be activated by scintillation, subsequently, contribute to PDT process.

Scope and Organization

The goal for my PhD research is to develop nanoparticle based system to improve cancer imaging diagnostic modality and enhance the non-invasive photodynamic therapy. To achieve the imaging enhancement, a strategy was developed by calcination of gadopentetic acid (Gd-DTPA) that results in a formulation of Gadolinium encapsulated carbon dots (Gd@C). The gadolinium incorporated carbon dots system has exhibited high r_1 relaxivity (5.88 $mM^{-1}s^{-1}$) and photostable fluorescence. The 12 nm Gd@C nanospheres have an inert carbon coating with efficiently renal clearance (Chapter 2). The in vivo stability, pharmacokinetics and cancer MRI T_1 imaging can be observed (Chapter 2). In addition, a T_1-T_2 dual modal contrast agent was developed based on Metal-Organic framework. The resulting Eu,Gd-NMOF@SiO_2 nanoparticles

presented high fluorescent, high MRI longitudinal (38 $mM^{-1}s^{-1}$) and MRI transversal (222 $mM^{-1}s^{-1}$) relaxivities. In vitro and in vivo MRI studies have confirmed that Eu,Gd-NMOFs could avidly induce both hyperintensities on T_1-weighted images and hypointensities on T_2-weighted images (Chapter 3). To enhance the non-invasive cancer therapy, a novel X-ray inducible photodynamic therapy (X-PDT) approach was plotted that allows PDT to be regulated by X-ray. Upon X-ray irradiation, the integrated nanosystem, comprised of a core of a nanoscintillator and a mesoporous silica coating loaded with photosensitizers, converts X-ray photons to visible photons to activate the photosensitizers and cause efficient tumour shrinkage (Chapter 4). In addition, X-PDT was further studied in vivo on an orthotopic cancer mouse model. The results have shown that X-PDT is a combination of more than just a PDT derivative but is essentially a PDT and RT combination. The two modalities target different cellular components (cell membrane and DNA, respectively) synergistically and give rise to enhanced therapy effects (Chapter 5).

This dissertation research has explored nanoparticle based imaging enhancement and X-ray induced photodynamic therapy in vitro and in vivo. I hope the results will ultimately benefit the field and provide valuable lessons for the researchers in revolutionizing individual and population-based health in the near future.

CHAPTER 2

GD-ENCAPSULATED CARBONACEOUS DOTS WITH EFFICIENT RENAL CLEARANCE FOR MAGNETIC RESONANCE IMAGING [1]

[1] Hongmin Chen, Geoffrey D. Wang, Yen-Jun Chuang, et al. 2014. Adv. Mater., 26:6761–6766. Reprinted here with permission of the publisher.

Keywords: Carbonaceous dots, gadolinium, MRI, T1 contrast agent, renal clearance

Introduction

Gadolinium(III)-based contrast probes have been widely used in clinical MRI. So far, there are at least nine formulations of Gd-containing contrast agents approved for human use in the states, and they are assisting more than 10 million magnetic resonance imaging (MRI) scans per year [28]. Free Gd is known to have a high toxicity profile, hence clinically used Gadolinium agents are all in the form of Gd-chelator complexes. Despite the complexation, however, these contrast agents are found to cause severe nephrogenic systemic fibrosis (NSF), especially for patients with renal diseases or poor renal functions [29-31]. For this reason, the FDA has issued warnings on the use of several Gd-based contrast agents in patients with kidney dysfunction [32-34]. This status underscores the significance of developing alternative contrast agents with more favorable safety profiles. One approach that has been intensively investigated is to load or imbed Gd(III) into a nanoparticle capsule/carrier that can suppress the Gd release while maintaining the T1-shortening capacity. Examples along this line include Gd_2O_3 nanoparticles [35], Gd-loaded silica nanoparticles [36], and Gd-doped Fe_3O_4 nanoparticles [37]. Due to their relatively large sizes, however, these nanoparticles are heavily accumulated in the reticuloendothelial (RES) organs after systemic injection, most prominently the liver. Subsequent particle degradation may cause release of free Gd(III) cations to the surroundings, and the long-term impact to the host is largely unknown.

Experiments and Results

Here we report Gd encapsulated carbon dots (hereafter referred to as Gd@C-dots) that may solve the dilemma. Gd@C-dots are prepared by simple calcination of gadopentetic acid (Gd-DTPA) in the air. Stemming from the inert carbon coating, Gd@C-dots remain stable even

in harsh biological environments with minimal Gd leakage [38]. Gd@C-dots afford not only a high r1 relaxivity (5.88 $mM^{-1}s^{-1}$), but also strong and photostable fluorescence, enabling them to act as dually functional imaging probes that can assist both real-time MR imaging and immunofluorescence histology. More excitingly, despite having dimensions (~12 nm) exceeding the commonly recognized threshold for renal clearance [39], systematically injected Gd@C-dots were found to be efficiently excreted via urine, a feature that further minimizes toxicity risks and may permit the use of the particles for repeated scans. All these qualities suggest the great potential of Gd@C-dots in clinical translation as MRI/fluorescence dually functional imaging probes. In the present study, we coupled c(RGDyK) as a model targeting ligand onto Gd@C-dots and examined, both in vitro and in vivo, the conjugates' colloidal stability, toxicity, tumor targeting, and imaging quality.

For Gd@C-dot synthesis, Gd-DTPA was first dried on a crucible and then calcined at 300 °C for 2 h in air. The raw products were dispersed in water and purified using centrifugal filter units (MWCO = 100K and 3K, which removed aggregations of nanoparticles and unreacted precursors, respectively). The yielded Gd@C-dots were spherical, with an average size of ~ 12 nm and relatively narrow size distribution (Figure 2.1a). High-resolution TEM (Figure 2.1b) found low diffraction contrast and no obvious lattice fringes with the particles, indicating that the carbon was amorphous. This correlates with previous observations that calcination at low pressure typically yields amorphous structures [40, 41]. Elemental mapping revealed that Gd was distributed evenly within the carbon particles with no signs of crystallization (Figure 2.1c, S2.1). This was also confirmed by scanning transmission electron microscopy (STEM) on individual C-dot particles (Figure 2.1d), revealing that Gd was well encased within the carbon shell (Figure 2.1e). X-ray photoelectron spectroscopy (XPS) analysis found peaks corresponding to both Gd4d

(143 and 148 eV) and Gd3d (1187 eV) [42, 43], suggesting that the oxidation state of Gd remains +3 in Gd@C-dots (Figure S2.2).

The as-synthesized Gd@C-dots were highly dispersible in aqueous solutions, maintaining colloidal stability for months without visible precipitation in PBS and at least 24 hours in 1 M NaCl (Figure S2.3a and Figure S2.3b). Dynamic light scattering (DLS) analysis showed a single

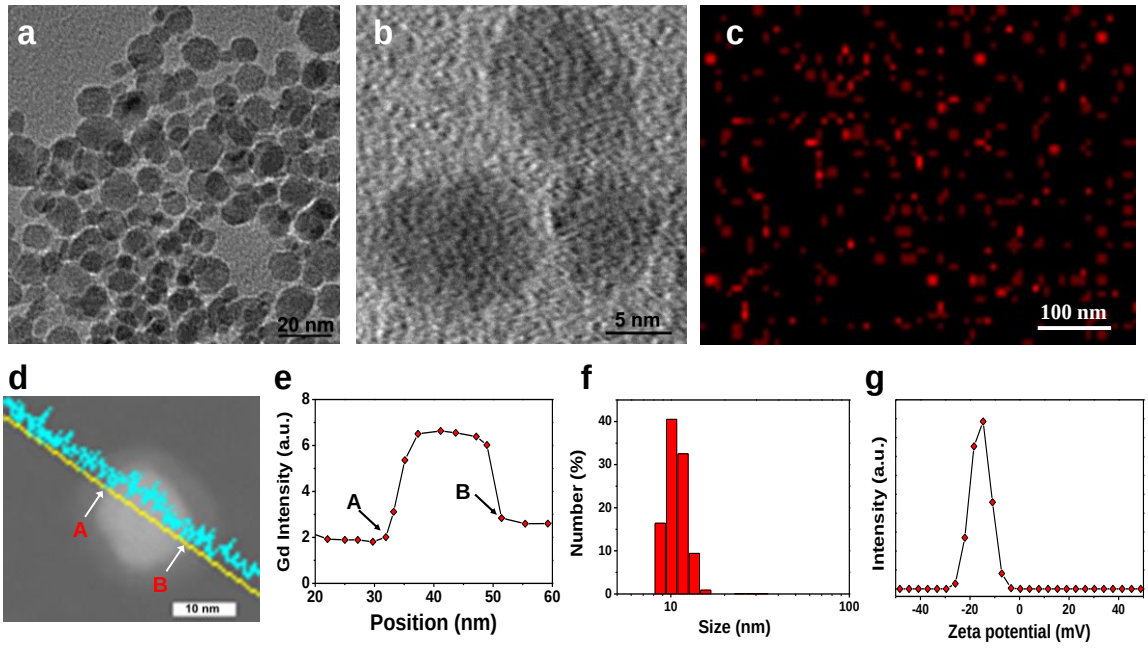

Figure 2.1 Characterizations of Gd@C-dots. (a) TEM and (b) HRTEM images of Gd@C-dots. (c) Elemental mapping (Gd) of Gd@C-dots. (d) STEM image of a single Gd@C-dot. (e) EDX line profile across the nanoparticle in d. Points "A" and "B" corresponded to those labeled **respectively** in d. (f) DLS analysis result of Gd@C-dots. (g) Zeta potential of Gd@C-dots.

narrow peak at ~ 12 nm, which is well correlated with the TEM result (Figure 2.1f, S2.4). The surface of Gd@C-dots was slightly negatively charged (-16.4 ± 0.6 mV, Figure 2.1g, S2.5), attributed to carboxyl groups that were either inherited from the DTPA precursors and/or

generated during the calcination. This is supported by FT-IR analysis, finding peaks at 3300 and 1600 cm^{-1} that are characteristic absorptions of OH and C=O, respectively (Figure S2.6) [44, 45]. Despite the charged surface, however, there was little size increase when the nanoparticles were incubated in the bovine serum (Figure S2.4b), indicating a minimal level of opsonization.

Gd@C-dots showed a broad absorption band between 200 to 500 nm, with a shoulder appearing at ~ 280 nm (Figure 2.2a). The spectrum resembles those published previously of pure C-dots [41, 45-47]. The Gd@C-dots are also highly fluorescent, and can be excited by light of a wide range of wavelengths to emit strong photoluminescence (Figure 2.2a). Such wavelength-dependent fluorescence is also similar to conventional C-dots [40, 44]. Impressively, there was almost no drop of photoluminescence intensity of Gd@C-dots even after 24 hours of continuous UV illumination (Figure 2.2b). This photostability is vastly superior to organic dye molecules, and even better than CdSe/ZnS quantum dots [48, 49], both of which were completely bleached within hours of UV exposure (Figure 2.2c). The T1 contrast ability was investigated on a 7T magnet with agarose samples of Gd@C-dots. Gd@C-dots showed an r1 of 5.88 $mM^{-1}s^{-1}$ on a Gd basis (Figure 2.2d,e), which is significantly higher than Gd-DTPA (3.10 mM-$1s^{-1}$) [50, 51]. The enhanced r1 was mainly attributed to the increase in the rotational correlation time (τR) as a result of binding Gd to a nanoparticle [52].

The inert carbon coating was anticipated to effectively block the leakage of Gd into the surroundings. To investigate, we incubated Gd@C-dots in phosphate buffered saline of pH 5 or 7.4 at 37 ˚C for 72 h. At both pH values, we observed no drop of luminescence intensity and negligible Gd leakage from the nanoparticles over time (Figure 2.3a, b). We also studied the cytotoxicity of Gd@C-dots, and for better assessment, we added 2.5 mM Ca(II) into the cell incubation medium. This was to test the particles' stability against transmetallation, which is the

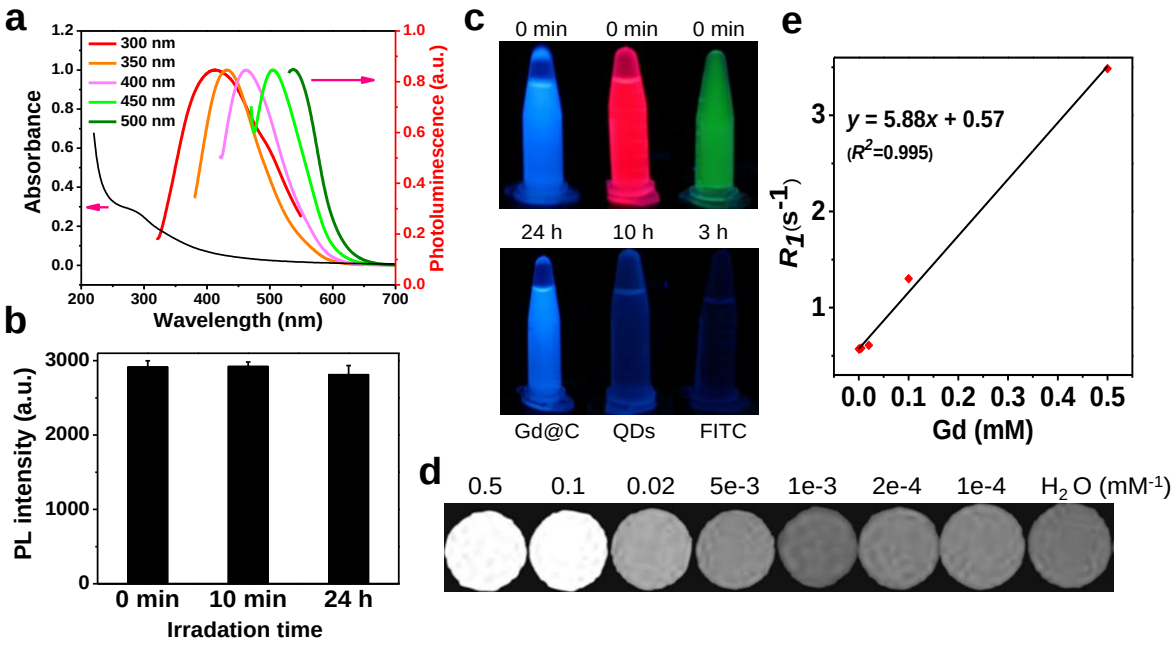

Figure 2.2 Optical and magnetic properties of Gd@C-dots. (a) Absorption and photoluminescence spectra of Gd@C-dots. (b) Photostability study. Gd@C-dots were under continuous irradiation by UV light (30 W, 254 nm) and the photoluminescence (ex/em 360/425 nm) intensity was monitored over time. (c) Comparison of photostability among FITC, CdSe/ZnS QDs, and Gd@C-dots. The three solutions were under continuous irradiation by UV light (30 W, 254 nm) for different amounts of time. (d) T1-weight MR images of Gd@C-dot agarose samples of different Gd concentrations. (e) Linear correlation between R1 (T1-1) and Gd concentration, based on readings from d. The r1 relaxivity, which is the slope of the curve, was determined to be 5.88 $mM^{-1}s^{-1}$.

major cause of toxicity for conventional Gd contrast agents [53]. Despite the presence of calcium, there was no significant drop of cell viability even at high nanoparticle concentrations (0–100 μg

Gd/mL, Figure 2.3c). This is in stark contrast to Gd-DTPA, whose toxicity is dramatically increased when incubated with calcium, showing an IC50 of 33.1 µg/mL (Figure 2.3c) [54, 55].

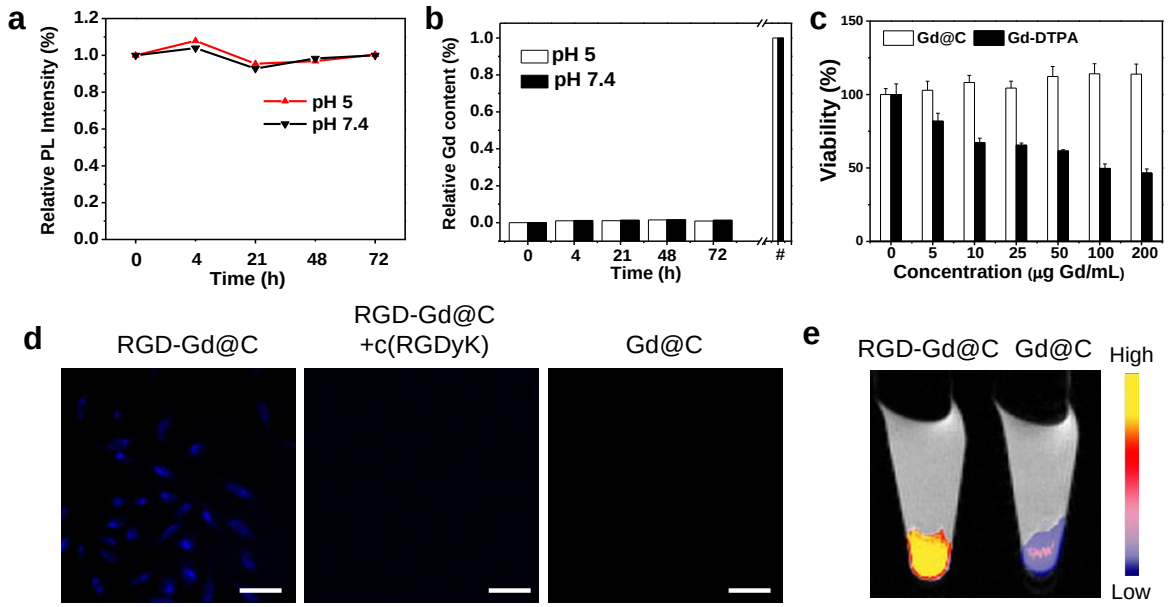

Figure 2.3 Cytotoxicity and cell targeting. (a) Photoluminescence intensity (ex/em 360/425 nm) change when Gd@C-dots were incubated in buffers of different pH values. (b) Gd release from Gd@C-dots over time. The nanoparticles were incubated in solutions with pH 5 or 7.4. #: The overall Gd concentrations in the solutions. (c) Cell viability, evaluated by MTT assays with U87MG cells. 2.5 mM Ca(II) was added in the incubation medium. (d) Cell targeting study. RGD-Gd@C-dots were incubated with U87MG cells for 30 min and the cells were then imaged under a fluorescence microscope (scale bar, 10 µm). For controls, cells were incubated with Gd@C-dots at the same Gd concentration or with RGD-Gd@C-dots in the presence of free c(RGDyK) (30×). (e) T1-weighted MR images of cell pellets, where cells had been incubated with either RGD-Gd@C-dots or Gd@C-dots.

The carboxyl groups on the particle surface offer a facile means to tether functional bio-species. In the present study, we coupled c(RGDyK), a tumor targeting peptide, onto the Gd@C-

dots. A cyclic RGD derivative, c(RGDyK) holds strong binding affinity toward integrin $\alpha_v\beta_3$, a biomarker that is seen overexpressed on neoplastic blood vessels and many types of cancer cells [56]. After the coupling, the nanoparticles' zeta potential increased slightly to -12.0 ± 0.4 mV, and the size to ~16.0 nm (Figure S2.4c). The targeting specificity of the resulting c(RGDyK) conjugated Gd@C-dots (hereafter referred to as RGD-Gd@C-dots) was investigated with U87MG cells, which are integrin $\alpha_v\beta_3$ positive. After 30 min incubation, there was a high level of nanoparticle uptake (ex/em: 360/460 nm), with many signals concentrated in the cell endosomes/lysomes (Figure 2.3d). The cell uptake was dramatically suppressed when Gd@C-dots were co-incubated with free c(RGDyK) (30×), indicating that the uptake was mostly mediated by RGD-integrin interaction. Such difference in cell uptake can also be discerned by MRI. Figure 2.3e shows a T1-weighted MR image of 10^5 U87MG cells that had been incubated with either RGD-Gd@C-dots or Gd@C-dots. Compared to the control, significantly enhanced signals were observed in the cells incubated with RGD@C-dots (Figure 2.3e).

In vivo MRI was first investigated with Gd@C-dots in normal nude mice. The particles were intravenously (i.v.) injected (0.8 mg Gd/kg) into the animals, and T1-weighted images were acquired before and 10, 30, 60 min and 4 h post the particle injection (p.i.). There was an initial signal increase throughout the body, followed by a signal decay starting from 60 min. After 4 h, signals in most of the organs had subsided to the pre-injection levels, indicating excretion of the particles from the circulation (Figure 2.4a). Interestingly, the signal change in the liver was found to be small throughout the course of the experiment (Figure 2.4a, b). Instead, there was a dramatic increase of signals in the bladder, a sign of renal clearance of the injected nanoparticles. Similar pharmacokinetics was also observed with RGD-Gd@C-dots at the same dose (Figure 2.4a, b).

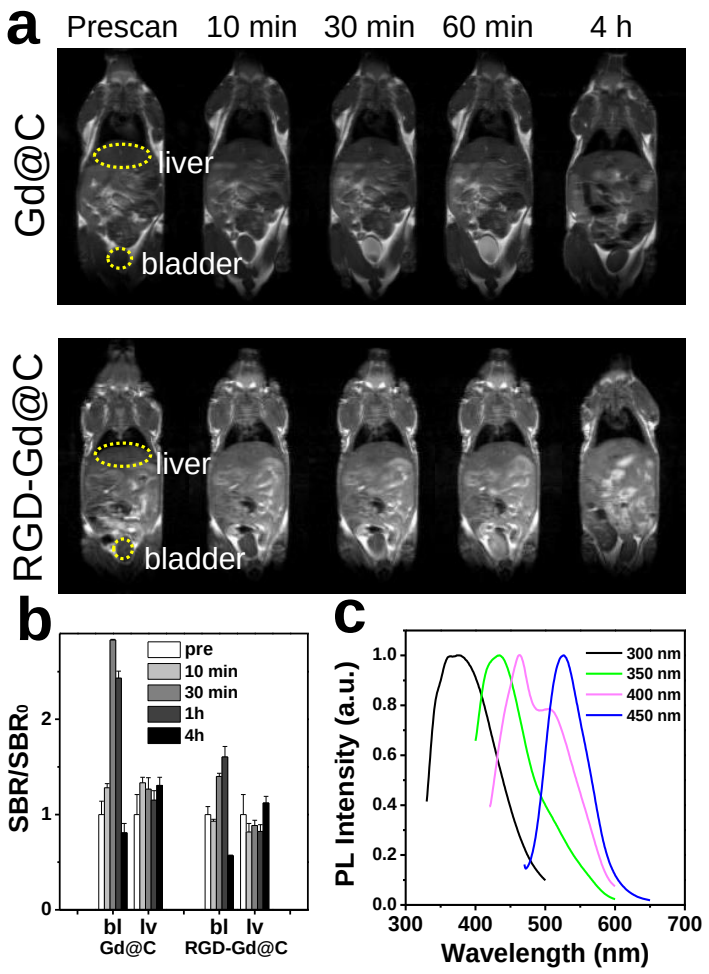

Figure 2.4 (a) T1-weighted MR images, acquired at different time points after injection of Gd@C-dots or RGD-Gd@C-dots. (b) Signal change in the bladder (bl) and liver (lv), based on region of interest (ROI) analysis on images from a). (c) Photoluminescence analysis on urine samples, taken 60 min after the injection of RGD-Gd@C-dots.

To further investigate, we collected urine samples from the animals ~60 min after the injection, and by centrifuging, harvested nanoparticles (Figure S2.7a). Analysis on the fragment found a

large amount of Gd (by inductively coupled plasma mass spectroscopy, or ICP-MS), along with strong photoluminescence that is characteristic of C-dots (Figure 2.4c, Figure S2.7b). On the other hand, no Gd was detected in the supernatant. This result confirmed that the Gd was still well encapsulated within the carbon shell at the time of excretion.

We next evaluated RGD-Gd@C-dots as tumor imaging probes in U87MG tumor-bearing mice. Briefly, RGD-Gd@C-dots at 3.2 mg Gd/kg were intravenously injected into the animals (n = 3). Images were acquired before and 10, 30, and 60 min after the nanoparticle injection. In a control group, Gd@C-dots at the same Gd dose were injected. Similarly, there was efficient renal clearance of RGD-Gd@C-dots, evidenced by strongly enhanced intensities in the bladder (Figure 2.5a). After 4 h, signals in the normal tissues had receded to the normal level for both RGD-Gd@C-dots and Gd@C-dots injected animals. Meanwhile, there was a signal enhancement of 42.6 ± 0.08% in tumours of in animals injected with RGD-Gd@C-dots compared to those injected with Gd@C-dots (Figure 2.5b,c). Harnessing the strong fluorescence of Gd@C-dots, we conducted immunofluorescent studies with the tumor tissues. Indeed, there was a good correlation between RGD-Gd@C-dots and positive integrin β3 staining (Figure 2.5d), confirming that the tumour retention was mainly mediated by RGD-integrin interaction.

An ideal imaging probe can home efficiently to the diseased area (e.g. a tumour) after systemic injection, with the unbound rapidly excreted from the host. This, however, has proven to be challenging for nanoparticles, most of which have a relatively large size, a high tendency of opsonization, and as a result, a high level of liver accumulation [57, 58]. Previous studies by the Frangioni group showed that when the overall size was controlled below 5.5 nm, nanoparticles could be excreted by renal clearance, thereby avoiding extended durations in the host [59]. This size criterion, however, is difficult to meet for nanomaterials, including most Gd-containing

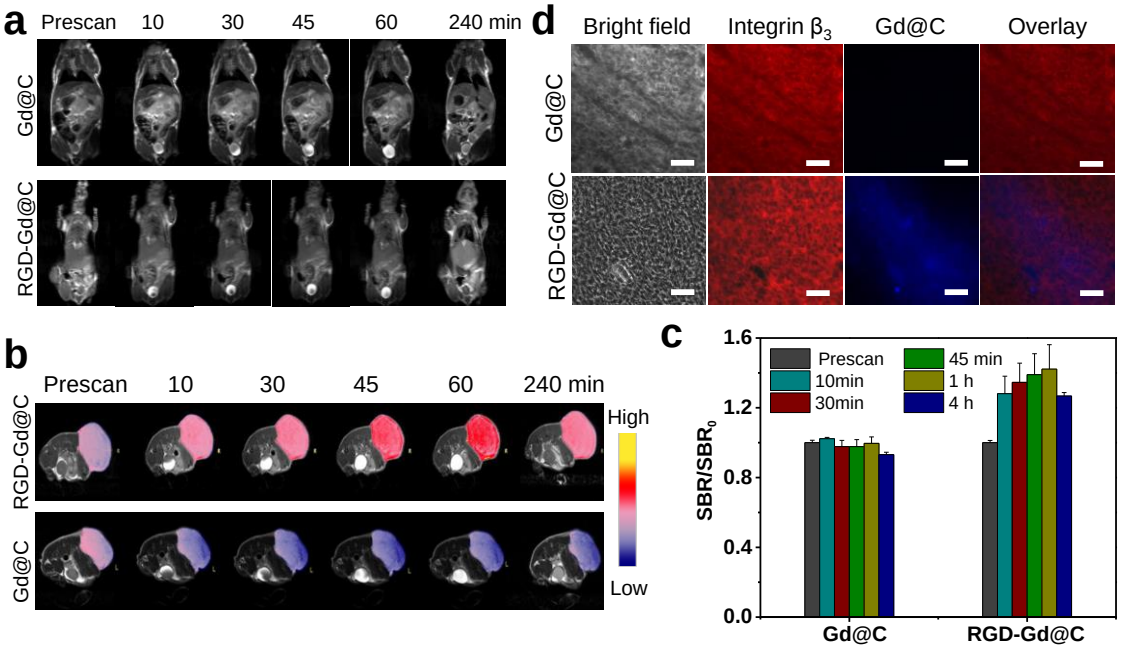

Figure 2.5 (a) T1-weighted transverse MR images. Gd@C-dots or RGD@C-dots (3.2 mg/kg) were intravenously injected into U87MG tumor bearing mice. Images were acquired at 0, 10, 30, 45, 60 and 240 min. For both types of nanoparticles, strong signals in the bladder were observed soon after the particle injection, indicating fast renal clearance. (b) T1-weighted coronal MR images. Significant signal enhancement was observed in tumors of animals injected with RGD@Gd-dots. (c) Relative signal change at different time points, based imaging results from b). (d) Immunofluorescence histology study with tumor samples. Good overlap was observed between RGD-Gd@C-dots and positive integrin β3 staining. As a comparison, Gd@C-dots showed minimal tumor uptake. Red, integrin β3 (Cy5); blue, fluorescence from C-dots. Scale bars, 50 μm.

nanoparticles under investigation. It is in this sense that the current observation is intriguing. Despite a size well above the recognized threshold for renal clearance, both RGD-Gd@C-dots and Gd@C-dots are able to be efficiently excreted via urine. Though the exact mechanism is

unknown, it is believed that the unique surface of Gd@C-dots may have played a role. With a shell made of amorphous carbon but decorated with carboxyl groups, the surface of Gd@C-dots lies between hydrophobic and hydrophilic. This affords the particles with good colloidal stability and meanwhile, may give them the capacity to cross certain types of biological barriers.

When Gd@C-dots were conjugated with ethylenediamine, the resulting conjugates, after i.v. injection into normal mice, showed no renal clearance (Figure S2.7b). Notably, the conjugation did not significantly increase the nanoparticle size but rendered the surface charge almost neutral. This observation, while confirming the significance of surface properties on renal clearance, indicate that the parameters required for clearance can be very delicate. Recently, there was a study by Gao et al. showing that 11.8 nm QDs had efficient renal clearance [60], which the authors also attributed to the unique surface coating (a dendron polymer). Also, Liu et al. discussed nanoparticle renal clearance in a recent review article and concludes that, in addition to particle size and shape, the surface may sometimes facilitate renal clearance, though the mechanism is unknown [61]. It is certainly important in future investigations to systematically study the topic and employ the knowledge for better design of nanoparticle-based imaging and drug delivery reagents [61].

Gd@C-dots show a quantum yield (QY) of 19.7% (Supporting Information), which is comparable to some of the highest reported QYs of C-dots [45]. Notably, such strong luminescence was obtained through a one-step synthesis, in contrast to conventional approaches that often require a post-synthesis surface passivation step to illuminate C-dots [46, 62, 63]. According to Sun et al., surface passivation is critical to the luminescence of C-dots and can be imparted not only through deliberate conjugation, but also by physical adsorption during synthesis [38]. Indeed, thermogravimetric analysis (TGA) on Gd@C-dots suggests that there is a

trace amount of DTPA left on the surface of Gd@C-dots (Figure S2.8), even after multiple rounds of washing. It is believed that the surface-bound DTPA contributes, at least in part, to the surface passivation and thereby the high luminescence of Gd@C-dots.

Interestingly, when calcining DTPA, 11 nm C-dots can be obtained but their QY was "only" ~12.0%. This difference in QY suggests that the encased Gd(III) could have played a role in the luminescence of the nanosystem. Meanwhile, since DTPA can form complexes with a wide range of transition metals, the current synthetic method can be easily extended to prepare other metal-containing C-dots, including those encapsulated with Mn^{2+}, Nd^{3+}, Y^{3+}, and Eu^{3+}. The yielded nanoparticles are all highly fluorescent in the visible range, but the positions of their peak luminescence are varied to a certain degree (Figure S2.9). This again indicates a dopant impact on the luminescence. It is postulated that the metallic center affects the electron distribution on the carbon shell and in turn enhances or shifts the luminescence. It is possible that leveraging the dopant effect could achieve C-dot derivatives possessing more favorable optical and/or magnetic properties, and the related investigation is underway.

Conclusions

Overall, we have developed a novel and straightforward methodology to prepare Gd@C-dots. Stemming from the inert carbon coating, Gd@C-dots are immune to the issue of Gd leakage that is often observed with complex-based Gd agents. Gd@C-dots afford good r1 relatixivity and strong photoluminescence, making them appealing MRI/fluorescence dually functional imaging probes. This potential is strengthened by the fact that Gd@C-dots and their conjugates can be efficiently excreted through renal clearance after systematic injection. Our observations suggest great potential of Gd@C-dots in clinical translation as safe and efficient imaging probes.

Supplemental Methods

Synthesis of Gd@C-dots

Gadolinium-DTPA solution (BioPAL, Inc.) was dried and then calcined at 300 ^{o}C for 2 h. This yielded black foam-like powder. The raw products were dispersed in water and subjected to centrifugation using centrifugal filter units (Millipore filter units: MWCO 100K, 3K). The soluble portion through the filter was collected. In a typical synthesis, we used 1 mL of Gd-DTPA solution (486 mg Gd-DTPA/mL) as precursors. After calcination and purification, we can obtain ~20 mg of 11 nm Gd@C-dots.

Physical characterizations

Optical measurements were performed at room temperature under ambient air conditions. UV-Vis absorption spectra were recorded on a Shimdzu 2450 UV-Vis spectrometer. Photoluminescence (PL) measurements were performed on a Hitachi F-7000 fluorometer. Fourier transform infrared (FT-IR) spectra were recorded on a Nicolet iS10 FT-IR Spectrometer. The PL quantum yield (QY) was estimated using quinine sulfate in 0.1 M H_2SO_4 (literature quantum yield: 58% at 354 nm excitation) as a reference standard, which was freshly prepared to reduce the measurement error [45]. The formula used for QY measurements is as follows:

$$\left(\mathrm{QY}\right)_{\mathrm{sm}} = \left(\mathrm{QY}\right)_{\mathrm{st}} \times \left[\left(\mathrm{PL}_{\mathrm{area}}/\mathrm{OD}\right)_{\mathrm{sm}} / \left(\mathrm{PL}_{\mathrm{area}}/\mathrm{OD}\right)_{\mathrm{st}}\right] \times \eta^2_{\mathrm{sm}}/\eta^2_{\mathrm{st}}$$

where Sm indicates the sample, St indicates the standard, η is the refractive index of the solvent, and PL area and OD are the fluorescence area and absorbance value, respectively. TEM and HR-TEM samples were prepared by dispersing the sample onto carbon-coated copper grids with the excess solvent evaporated. The TEM/HR-TEM overview images were recorded using a FEI

Tecnai20 transmission electron microscope operating at 200 kV. Energy Dispersive Spectroscopy (EDS) and element mapping was characterized using Hitachi HD2000 Dedicated Scanning Transmission Electron Microscope (STEM). Dynamic light scattering (DLS) analysis was performed on a Zetasizer Nano S90 size analyzer (Malvern Corp, U.K.). Fluorescence images were acquired on an Olympus X71 fluorescence microscope (ex/em: 360/420 nm). Thermogravimetric analysis (TGA) was carried out on a Mettler TGA/SDTA851 with a STAR software, version 8.10. The chemical environment of the Gd@c-dots was confirmed by X-Ray Photoelectron Spectroscopy (XPS), Al $K_{\alpha 1,2}$ X-ray source, Hemispherical Analyzer (Leybold Heraeus).

Bioconjugation with c(RGDyK)

Gd@C-dots were dispersed in a borate buffer (pH 8.3). Into the solution, carbodiimide (EDC) and N-hydroxysuccinimide (NHS) (10×) in DMSO was added, and the mixture was magnetically stirred for 30 min. The intermediate was purified by centrifugation, and redispersed in PBS (pH 7.4). Into the solution, c(RGDyK) in DMSO (20×) was added and the mixture was incubated for 2 h with gentle agitation. The product was collected using a centrifugal filtration unit (Millipore filter unit: MWCO 3K) and redispersed in PBS (pH = 7.4).

Physical- and photo-stability of Gd@C-dots.

Gd@C-dots were incubated in solvents of different pH and in fetal bovine serum (FBS) at 37 °C, and their fluorescence intensity changes were monitored (ex/em: 360/425 nm). The amount of Gd(III) concentration released from Gd@C-dots was measured by inductively coupled plasma mass spectrometry (ICP-MS). For photostability, Gd@C-dot, FITC, or CdSe@ZnS

quantum dot solutions were irradiated continuously by a UV lamp (254 nm, 30W), and their peak fluorescence emissions were monitored.

Cell toxicity

Cell viability was studied with U87-MG cells using standard MTT assays [41]. The cells were first seeded in 96-well plates (1×10^4 cells per well). After 24 h, Gd@C-dots at different concentrations were added. Incubation was carried out for 24 h with or without 2.5 mM $CaCl_2$. For comparison, Gd-DTPA at the same Gd concentrations were also tested.

MRI phantom study

Gd@C-dots with Gd concentrations ranging from 5×10^{-5} to 0.2 mM were suspended in 1% agarose gel in 300 µl PCR tubes. These tubes were then embedded in a home-made tank designed to fit the MRI coil. T_1-weighted MR images of the samples were acquired on a 7 T Varian small animal MRI system using the following parameters: TR/TE = 500/12 ms (T_1), 128×128 matrices, and repetition times = 4. To measure the longitudinal relaxation time of each sample, an inversion recovery FSE sequence with TR of 5000 ms, TE of 12 ms and ETL of 8 was used to obtain images at inversion times (TI) of 5, 10, 30, 50, 80, 200, 500, 700, 900, 1200 and 3000 ms, respectively.

In vitro cell uptake studies.

U87MG cells were grown in a petri dish of a sterile glass bottom at 37 °C in 5% CO_2. For cell uptake studies, cells were incubated in 1 mL media containing Gd@C-dots (50 µg) with and without the presence of c(RGDyK) (1 mg) for 1 hour. Cells were washed three times with PBS (pH 7.4), and then imaged under an Olympus X71 fluorescence microscope. For MRI

studies, 10^5 cells treated under similar conditions were collected in 300 μL PCR tubes and subjected to T_1-weighted MRI.

In vivo MRI with normal nude mice

Animal studies were performed according to a protocol approved by the Institutional Animal Care and Use Committee (IACUC) of University of Georgia. Before *in vivo* experiments, the Gd@C-dots and RGD-Gd@C-dots were filtered through sterilized membrane filters (pore size 0.22 μm) and stored in sterilized vials. For *in vivo* MRI studies, whole body transverse images of normal athymic nude mice were first acquired. The mice were then intravenously injected with 100 μL Gd@C-dots and RGD-Gd@C-dots (0.8 mg Gd/kg). Transverse and coronal T_1-weighted MR images were acquired at 10, 30, 45 min, 60 min and 4 h post the nanoparticle injection. The images were acquired using the following parameters: TR/TE= 500/12 ms, field-of-view (FOV) = 70 × 70 mm^2, matrix size = 256 × 256, slice = 4, and thickness = 1 mm.

Tumor imaging

Tumor models were developed in 5-6 week athymic nude mice (Harlan) by subcutaneous implantation of 10^6 human glioblastoma U87MG cells suspended in 100 μl of serum-free DMEM to the right lower flank of a mouse. Imaging studies were conducted 3-4 weeks later. Specifically, the tumor-bearing mice were intravenously injected with Gd@C-dots and RGD-Gd@C-dots (3.2 mg Gd/kg). Transverse and coronal T_1-weighted images were acquired at 15, 30, 60, 120, and 240 min post injection using the following parameters: TR/TE= 500/12 ms, field-of-view (FOV) = 70 × 70 mm^2, matrix size = 256 × 256, slice = 4, thickness = 1 mm. To quantify the signal change, we calculated the signal-to-background ratio (SBR) by finely analyzing regions of interest (ROIs) of the MR images and calculated the values of SBR/SBR_0 to represent the signal

changes [64, 65]. Signal intensity (SI) of normal live, kidney, brain, and muscle were measured before and after injection of Gd@C nanoparticles. The mean SI measurements of 3 mice per group were used for statistical analysis. Because of slight changes in the position of the mice at different imaging stages, pre and post ROIs were determined manually on each image as reproducible as possible. For each animal, 3-5 ROIs were selected to measure the SI of the liver, kidney, brain and muscle. The SBR values were calculated according to SBR= SI_{organ}/SI_{muscle} for coronal plane, and $SBR/SBR_0 = SI_t/SI_0$ for transverse plane.

Statistical analysis

Quantitative data were expressed as mean ± s.e.m.

Supplemental Figures

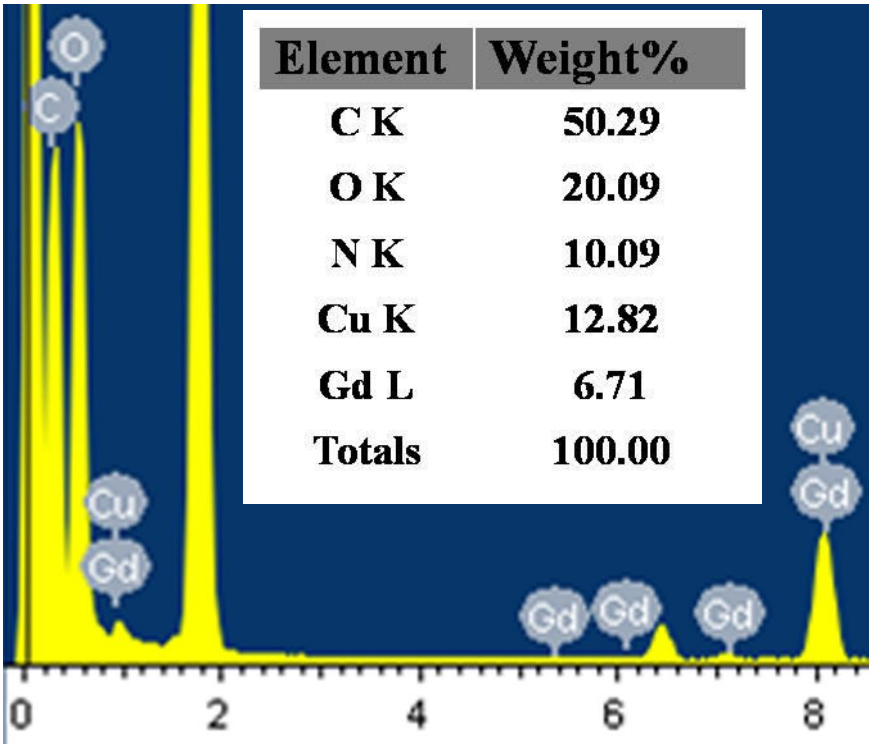

Figure S2.1. EDX pattern of Gd@C-dots. Table in the inset presents the elemental ratios (weight percentages) calculated by the EDX software.

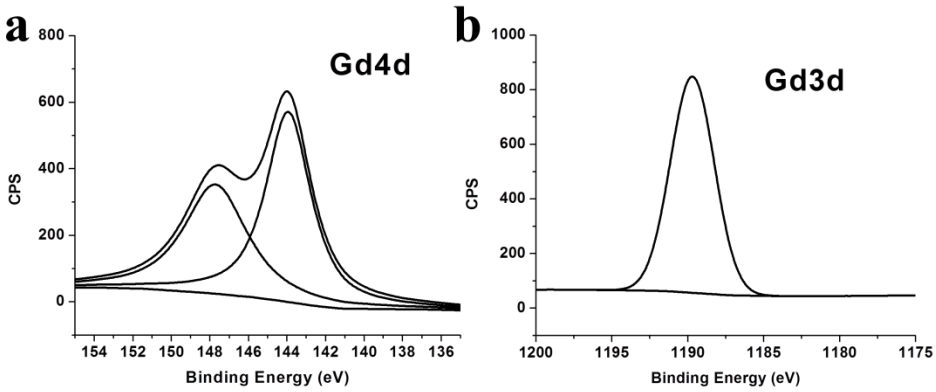

Figure S2.2. XPS spectra of Gd@C-dots. Binding energy peaks corresponding to both Gd4d (143 and 148 eV) and Gd3d (1187 eV) were observed, suggesting that the oxidation state of Gd remains +3 in Gd@C-dots.

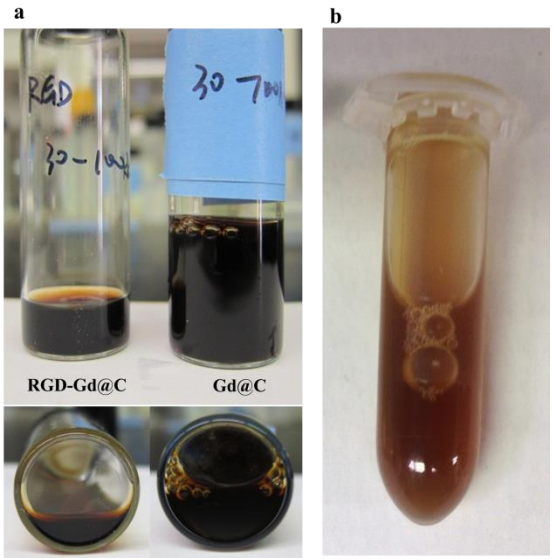

Figure S2.3. (a) Colloidial stability of Gd@C-dots and RGD-Gd@C-dots. The particles remained stable for 6 months in solution and there was no visible precipitate. (b) Storage stability of Gd@C-dots in 1 M NaCl. No particle aggregation was observed for at least 24 h.

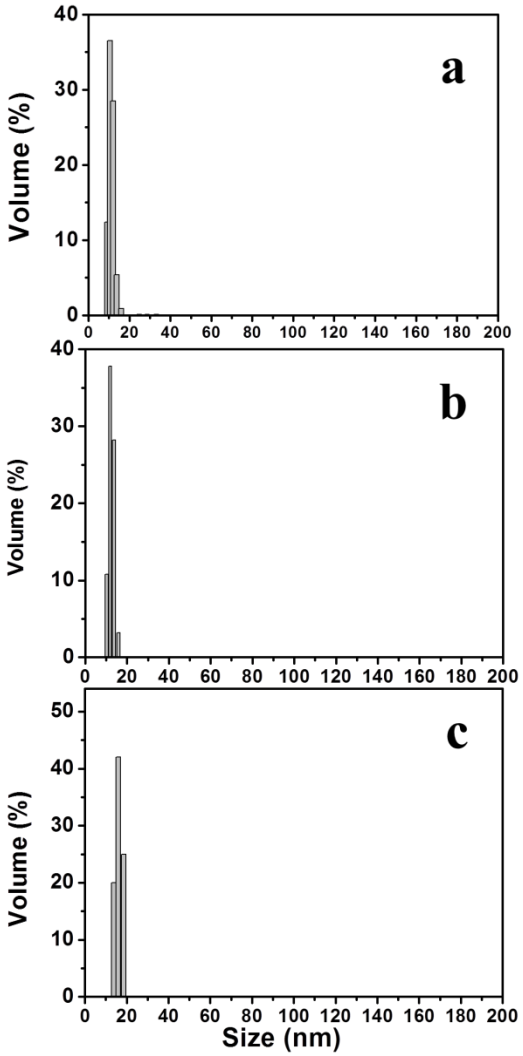

Figure S2.4. Dynamic light scattering analysis of (a) Gd@C-dots, (b) RGD-Gd@C-dots, and (c) Gd@C-dots after incubation in fetal bovine serum for 24 h.

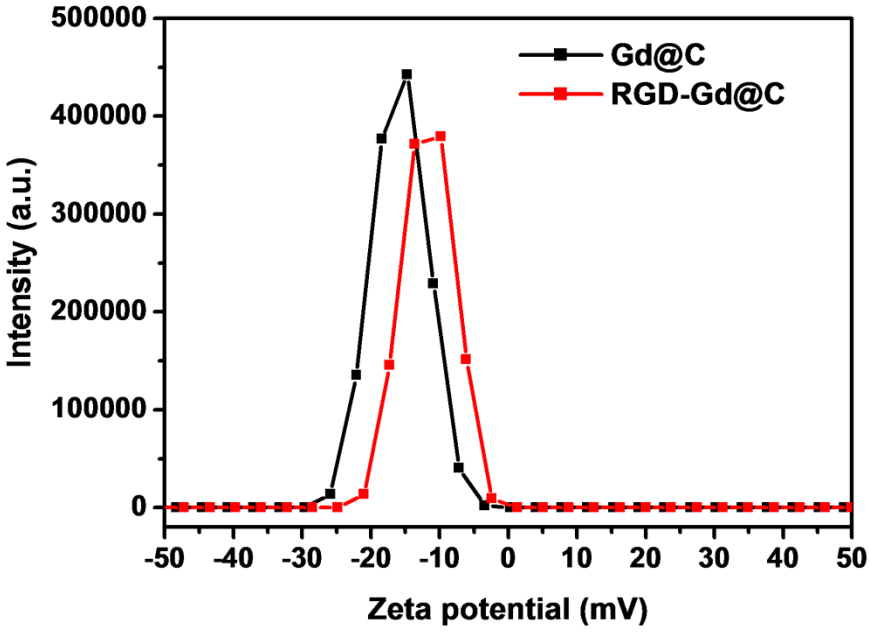

Figure S2.5. Zeta potentials of Gd@C-dots and RGD-Gd@C-dots.

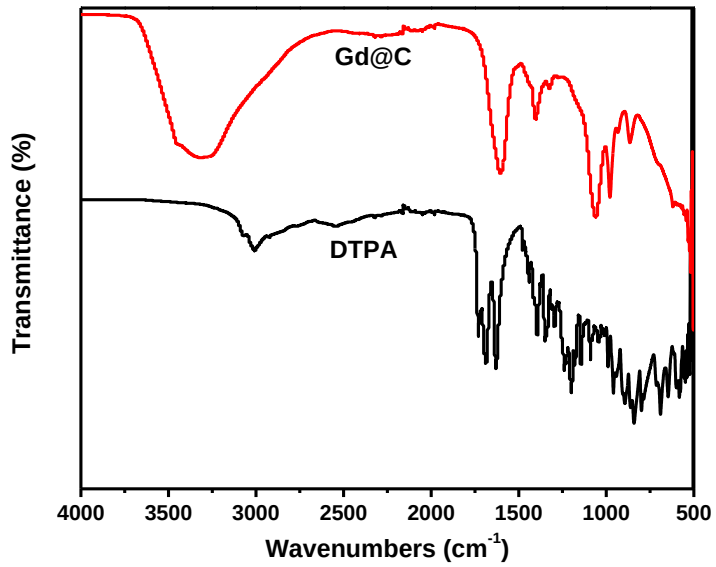

Figure S2.6. FTIR spectra of Gd@C-dots and DTPA.

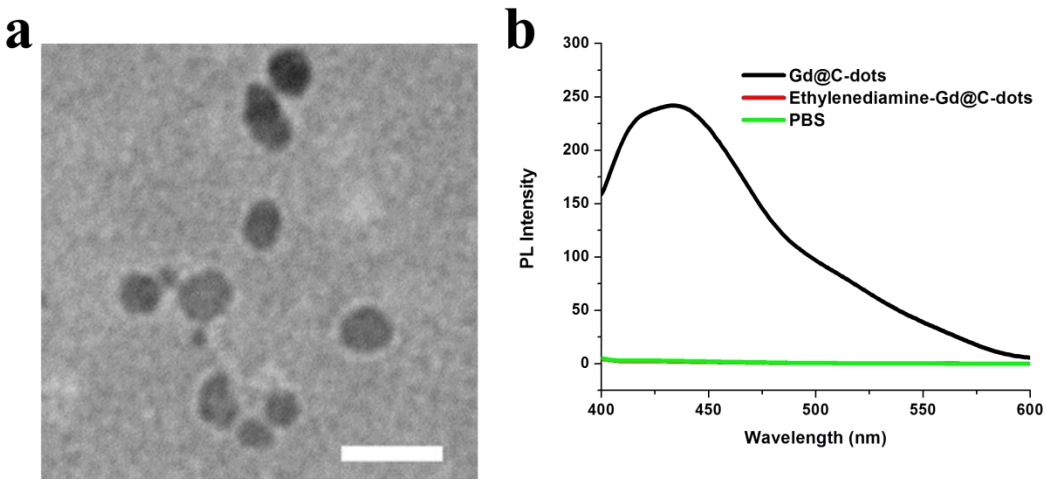

Figure S2.7. (a) TEM image of urine samples from mice injected with Gd@C-dots (scale bar: 20 nm). (b) Photoluminescence analysis on urine samples taken from mice 60 min after the injection of Gd@C-dots, ethylenediamine conjugated Gd@C-dots, or PBS.

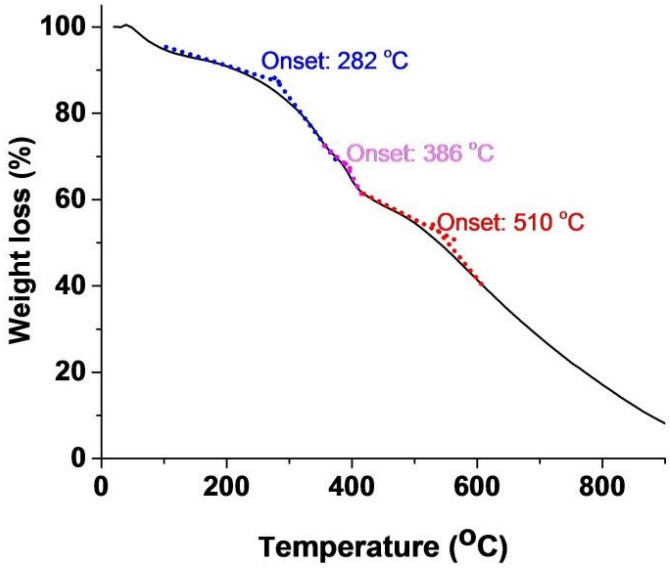

Figure S2.8: TGA analysis of Gd@C-dots. There was an initial moisture loss and then, at around 386 ˚C, a small weight drop attributable to the loss of surface-bound DTPA.[5]

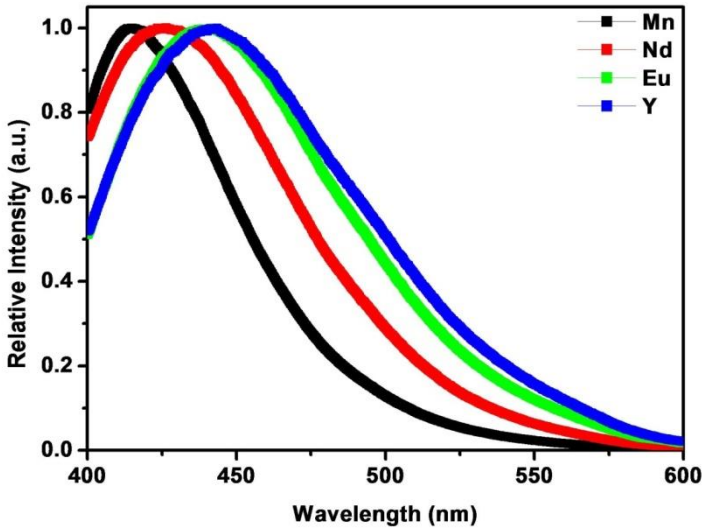

Figure S2.9. Fluorescence spectra of Mn, Nd, Eu and Y encapsulated C-dots, prepared by calcining corresponding metal-DTPA complexes at 300 ˚C in air.

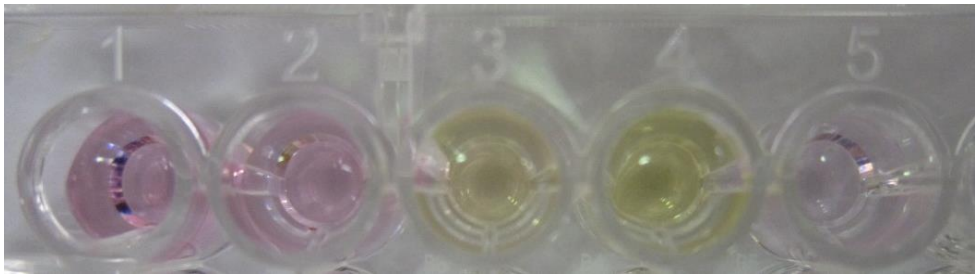

Figure S2.10. Gd leakage under different conditions, using xylenol organge (XO) as a Gd(III) indicator. (1) Gd-DTPA plus 2.5 mM Ca^{2+}, (2) $Gd(NO_3)_3$, (3) Gd@C-dots plus 1M HCl, (4) Gd@C-dots, and (5) XO only.

TOC

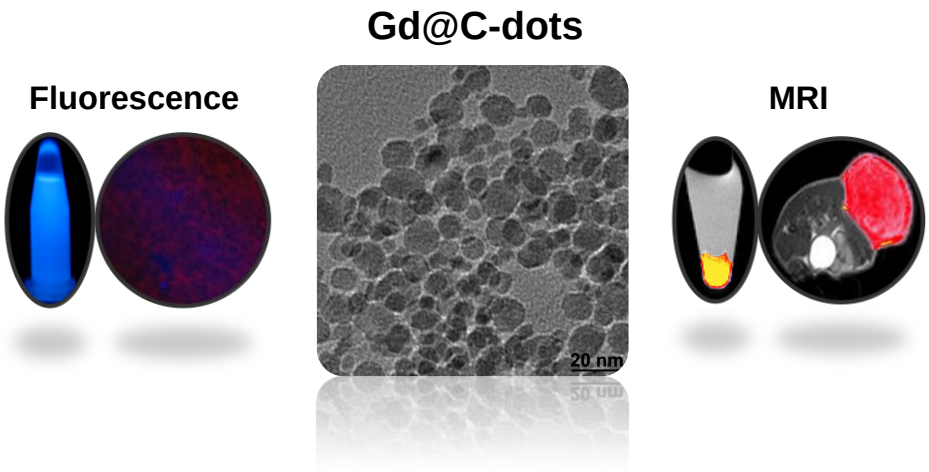

Nanoprobes for MRI and optical imaging. Gd@C-dots possess strong fluorescence and can effectively enhance signals on T1-weighted MR images. The nanoprobes are low-toxic and despite a relatively large size, can be efficiently excreted by renal clearance from the host after systemic injection.

CHAPTER 3

Gd AND Eu CO-DOPED NANOSCALE METAL-ORGANIC FRAMEWORK AS A T_1-T_2 DUAL-MODAL CONTRAST AGENT FOR MAGNETIC RESONANCE IMAGING[2]

[2] Geoffrey D. Wang, Hongmin Chen, Wei Tang, et al. 2016. Tomography. 2(3):179-187. Reprinted here with permission of the publisher.

Abstract

There have been a recent interest of developing T_1-T_2 dual-mode probes that can simultaneously enhance contrast on T_1- and T_2- weighted images. A common strategy is to integrate T_1 and T_2 components in a decoupled manner into a nanoscale particle. This approach, however, often requires multiple-step synthesis and delicate nano-engineering, which may potentially affect the production and wide applications of the probes. We herein report facile synthesis of a 50 nm nanoscale metal-organic framework (NMOF) comprised of Gd^{3+} and Eu^{3+} as metallic nodes. These nanoparticles can be prepared in large quantities and can be easily coated with a layer of silica. The yielded Eu,Gd-NMOF@SiO_2 nanoparticles are low toxic, highly fluorescent, and afford high longitudinal (38 $mM^{-1}s^{-1}$) and transversal (222 $mM^{-1}s^{-1}$) relaxivities on a 7T magnet. The nanoparticles were conjugated with c(RGDyK), a tumor targeting peptide sequence which has a high binding affinity toward integrin $\alpha_v\beta_3$. When intratumorally or intravenously injected, Eu,Gd-NMOF@SiO_2 nanoparticles induce simultaneous signal enhancement on T_1-weighted images and signal attenuation on T_2-weighted images. These results suggest great potential of the NMOFs as a novel T_1-T_2 dual-mode contrast agent.

Keywords: MRI, contrast agent, Gadolinium, MOF

Abbreviations: isophthalic acid (H2IPA), dimethyl formamide (DMF), polyvinylpyrrolidone (PVP), spin echo multiple slice (SEMS), fast spin echo multiple slice (FSEMS), hexamethylenetetramine (HMTA), tetraethylorthosilicate (TEOS), (3-aminopropyl) triethoxysilane (APTES), Magnetic resonance imaging (MRI), metal-organic framework (MOF), 3-(4,5-dimethylthiazol-2-yl)-2,5-diphenyltetrazolium bromide (MTT), arginylglycylaspartic acid (RGD)

Introduction

Magnetic resonance imaging (MRI) is one of the most widely used diagnostic tools in the clinic. MRI affords a number of advantages such as noninvasiveness, high spatial and temporal resolutions, and good soft tissue contrast [66, 67]. However, the intrinsic MRI signals are often suboptimal in delineating internal organs and diseased tissues. To improve imaging quality, contrast agents, often in the form of paramagnetic compounds or superparamagnetic nanoparticles, are administered prior to or during a MRI scan [68-70]. These magnetic agents alter local magnetic environments, inducing shortened longitudinal relaxation times (T_1) and transverse relaxation times (T_2). While most agents shorten both T_1 and T_2, the impact is often dominant on one side. So far in the clinics, the most commonly used T_1 agents are Gd complexes [71] and for T_2 imaging, iron oxide nanoparticles are often used [72].

Recently, there is a growing interest of developing T_1-T_2 dual-mode contrast agents that can simultaneously modulate T_1- and T_2-weighted contrasts. Such a technology is attractive because MRI has an intrinsic high background signal. Even with conventional T_1 and T_2 contrast agents, the diagnosis can often be affected by artifacts caused by truncation, motion, aliasing, and chemical shift [73]. T_1-T_2 dual-mode imaging may minimize the risks of ambiguity and improve image conspicuity and diagnostic sensitivity [74-76]. To this end, there have been some efforts of integrating T_1 and T_2 contrast components using nanoscale engineering. These include tethering Gd-complex onto the surface of iron oxide nanoparticles [77], doping Gd cations into the matrix of iron oxide nanoparticles [78, 79], and forming a core/shell nanostructure where the T_1 and T_2 components are magnetically decoupled [80, 81]. However, these approaches often involve multiple-step synthesis and/or delicate control over the interaction between the T_1 and T_2 components, which may potentially limit their production and applications.

Herein we report facile synthesis of a novel, nanoscale metal-organic framework (NMOF) based T_1-T_2 dual-modal contrast agent. Specifically, using isophthalic acid (H_2IPA) as building blocks, Eu^{3+} and Gd^{3+} as metallic nodes, and polyvinylpyrrolidone (PVP) as surfactant as reaction precursors, we prepared ~50 nm self-assembled Eu,Gd-NMOFs in large quantities. Unlike conventional NMOFs, which are rapidly degraded in an aqueous environment [82], our Eu,Gd-NMOFs are stable in water for up to 24 hours due to strong interaction between the lanthanides and H_2IPA as well as the PVP coating. To improve the particle stability against transmetallation, the Eu,Gd-NMOFs were further coated with a layer of silica. The resulting Eu,Gd-NMOFs@SiO_2 particles manifested both high r_1 and high r_2 relaxivities (38 $mM^{-1}s^{-1}$ and 222 $mM^{-1}s^{-1}$, respectively), suggesting their potential as a T_1-T_2 dual-modal contrast agent. Such a possibility was demonstrated first in vitro and then in vivo with either intratumorally or intravenously injected nanoparticles, resulting in simultaneous hyperintensities on T_1-weighted images and hypointensities on T_2-weighted images. Meanwhile, Eu,Gd-NMOF@SiO_2 nanoparticles also afford strong fluorescence which permits in vitro and potentially histological analysis of nanoparticle location within tissue specimens. Overall, the Eu,Gd-NMOFs can be synthesized in a straightforward and high-throughput fashion and afford excellent magnetic and optical properties, suggesting their great potential as a novel and versatile multimodal imaging probe.

Methodology

Material

$Gd(NO_3)_3{\cdot}6H_2O$, $Eu(NO_3)_3{\cdot}6H_2O$, isophthalic acid (H_2IPA), polyvinylpyrrolidone (PVP40), hexamethylenetetramine (HMTA), dimethylformamide (DMF), tetrahydrofuran (THF),

tetraethylorthosilicate (TEOS), (3-aminopropyl) triethoxysilane (APTES), ammonia, and ethanol were purchased from Aldrich and used without further purification.

Synthesis of Eu,Gd-NMOF.

In a typical synthesis, H_2IPA (1 mg), $Gd(NO_3)_3 \cdot 6H_2O$ (10 mg), $Eu(NO_3)_3 \cdot 6H_2O$ (0.5 mg), PVP (60 mg), and HMTA (16 mg) was first dissolved in a mixed solution containing 1.0 mL of DMF and 4.0 mL of water. Precursors of other ratios were also tested. The mixture was heated at 100°C for 4 min to induce Eu,Gd-NMOF growth. The resulting Eu,Gd-NMOFs were collected by centrifuge, washed with ethanol, and re-suspended in ethanol for further characterization. For comparison, the synthesis was also carried out without HMTA or H_2IPA.

Synthesis of silica-coated Eu,Gd-NMOF (Eu,Gd-NMOF@SiO_2).

Eu,Gd-NMOF@SiO_2 was prepared by mixing 10 mg of the as-synthesized Eu,Gd-NMOF with 100 µl of TEOS, 10 µl of APTES, and 0.5 mL of ammonia (28%) in 15 mL of ethanol at room temperature overnight. The Eu,Gd-NMOF@SiO_2 was isolated by centrifugation at 10,000 rpm for 10 minutes.

Bio-conjugation (preparation of RGD-NMOF@SiO_2)

50 mg of Eu,Gd-NMOF@SiO_2 nanoparticles were dispersed in a borate buffer (50 mM, pH 8.3) with magnetic stirring. Into the solution, 0.5 mg of bis(sulfosuccinimidyl)suberate (BS^3) in 0.1 mL of DMSO was added. After 0.5 h, the conjugate intermediate was collected by centrifuge and redispersed in borate buffer (50 mM, pH 8.3). c(RGDyK) in DMSO was added to the solution and the mixture was incubated at room temperature for 2 h to form RGD- Eu,Gd-NMOF@SiO_2 nanoparticles.

Characterizations.

All transmission electron microscopy (TEM) images were obtained on a FEI Tecnai 20 transmission electron microscope operating at 200 kV. Optical measurements were performed at room temperature under ambient air conditions. UV-vis absorption spectra were recorded on a Shimdzu 2450 UV-Vis spectrometer. Fluorescence measurements were performed using a Hitachi F-7000 spectrofluorimeter. Fourier transform infrared (FT-IR) spectra were recorded on a Nicolet iS10 FT-IR Spectrometer (Thermo Scientific). Powder X-ray diffraction (XRD) intensity data was collected on a PANalytical X'Pert PRO MRD powder diffractometer using Cu Kα radiation.

Stability of Eu,Gd-NMOF and Eu,Gd-NMOF@SiO_2 in water and PBS

5 mg of Eu,Gd-NMOFs or Eu,Gd-NMOF@SiO_2 were dispersed in 1 mL aqueous solutions with pH ranging from 3 to 11. Gentle agitation was applied. After 24 hours, aliquots of the solution were taken to measure change in fluorescent intensity.

MRI phantom study

Eu,Gd-NMOF@SiO_2 with Gd concentrations ranging from 5×10^{-5} to 0.08 mM were suspended in 1% agarose gel in 300 μl PCR tubes. These tubes were then embedded in a home-made tank designed to fit the MRI coil. T1- and T_2-weighted MR images of the samples were acquired on a 7 T Varian small animal MRI system. For T_1-weighted, a T_1 inversion recovery fast spin echo (FSE) sequence was used, with the following parameters: TR = 5000 ms, TE = 12 ms, ETL = 8, inversion times (TI) = 5, 10, 30, 50, 80, 200, 500, 700, 900, 1200 and 3000 ms. For T_2-weighted, a FSE sequence was used, with the following parameters: TR = 3 s, TE from 10 to 100 ms, with the step size set at 10 ms. For both sets of imaging, the following slice settings

were applied: field-of-view (FOV) = 65 × 65 mm^2 ; matrix size = 256 × 256; 4 coronal slices with 1 mm slice thickness.

Cell culture

U87MG (human glioblastoma) cells (ATCC) were grown in DMEM medium supplemented with 10% FBS and 100 units/mL of penicillin/streptomycin (ATCC). The cells were maintained in a humidified incubator with 5% carbon dioxide (CO_2) atmosphere at 37 °C.

Toxicity of NMOF in vitro

U87MG cells were seeded into a 96-well culture plate at a density of 4,000 cells/well and cultured overnight. Media was removed and replaced with fresh media containing different Eu,Gd-NMOF@SiO_2 concentrations (0-50 μM Gd^{3+}). Plates were incubated for 24 h at 37°C and 5% CO_2. Viability was measured by MTT assays [83].

Cell uptake

U87MG cells were incubated with Eu,Gd-NMOF@SiO_2 or RGD-Eu,Gd-NMOF@SiO_2 (20 μg/mL) in a chamber slide for 1 h. U87MG cells only served as a negative control. After the incubation, the cells were washed three times with PBS to remove unbound nanoparticles. The slides were then imaged on an Olympus X71 fluorescence microscope.

In vitro MRI with cell pellets

U87MG cells were cultured until approximately 70% confluency was reached. Cells were then washed with PBS, and incubated with 2 mL of media containing 100 μg of RGD-Eu,Gd-NMOF@SiO_2 or Eu,Gd-NMOF@SiO_2. After 1 hour, the media were removed and cells were collected as pellets in 200 μL tubes. These tubes were then embedded in a home-made tank

designed to fit the MRI coil. T1-and T_2-weighted MR images were acquired on a 7 T Varian small animal MRI system using fast spin-echo sequence with the following parameters: TR/TE = 500/14 ms (T1), TR/TE = 3000/8 ms (T_2), slice thickness = 0.5 mm, FOV = 60 × 50 mm, echo train length (ETL) = 8, 256 × 256 matrices, and repetition times = 3.

In vivo MRI with subcutaneously injected nanoparticles

Animal studies were performed according to a protocol approved by the Institutional Animal Care and Use Committee (IACUC) of University of Georgia. Before in vivo experiments, the Eu,Gd-NMOF@SiO_2 nanospheres were filtered through sterilized membrane filters (pore size 0.22 μm) and stored in sterilized vials. U87MG cancer cells were subcutaneously (s.q.) inoculated into the right flanks of 6-week old nude mice. Imaging was performed ~ 3 weeks later on a 7T Varian small animal MRI system. T_1- and T_2-weighted MR images were acquired using spin-echo multi slices (SEMS) and fast spin-echo multi slices sequence (FSEMS), respectively, with the following parameters: TR/TE = 500/14 ms (T_1) and TR/TE = 3000/33 ms (T_2), slice thickness = 1.0 mm, FOV = 60×50 mm, 256×256 matrices, and repetition times = 3. 0.8 mg/kg of Eu,Gd-NMOF nanospheres were intratumorally injected. T_1- and T_2-weighted MR images before and 4 h after the injection were acquired.

In vivo liver MRI with systemically injected nanoparticles

6-week old female balb/c mice were imaged on a 7T Varian small animal MRI system. T_1- and T_2-weighted MR images were acquired using SEMS and FSEMS with the following parameters: TR/TE = 500/16 ms (T_1) and TR/TE = 2500/8.65 ms (T_2), slice thickness = 1.0 mm, FOV = 30×30 mm, 256×256 matrices. Eu,Gd-NMOFs were intravenously injected at 0.8 mg/kg. T_1- and T_2-weighted MR images of the liver before and 4 h after the injection were acquired.

Results and Discussion

Synthesis and characterization of Eu,Gd-NMOFs

Eu,Gd-NMOFs were synthesized by mixing H_2IPA, $Gd(NO_3)_3$, $Eu(NO_3)_3$, hexamethylenetetramine (HMTA) and polyvinyl-pyrrolidone (PVP) in a DMF and water mixed solution and heating the solution at 100 °C. In a previous study, Oh et al. reported NMOF

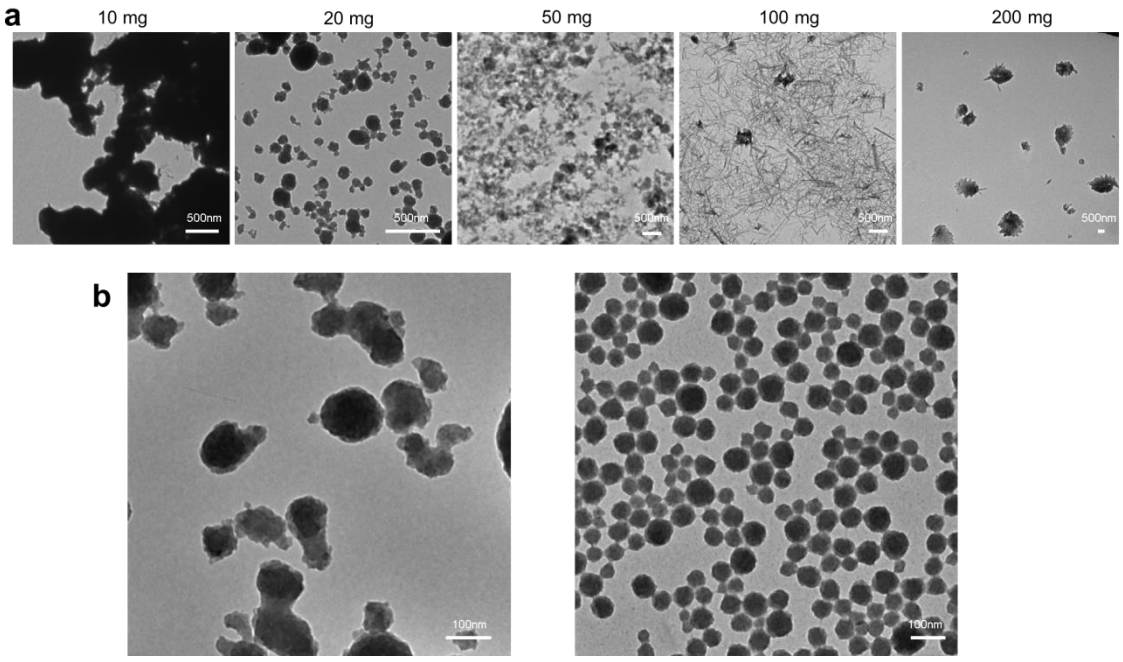

Figure 3.1. Synthesis of Eu,Gd-NMOFs. (a) Poor size control if HMTA and PVP are not used as reactants. Despite the ratio between the lanthanide cations and H_2IPA (the amount of which was increased from 10 mg to 200 mg), the nanoparticle products showed poor size distribution. Notably, the synthesis was conducted in a DMF/THF solvent as the resulting NMOFs were not stable in water. (b) The impact of HMTA and PVP on the nanoparticle formation. Left, when HMTA was added to the precursors, Eu,Gd-NMOFs were formed in a DMF/water solvent but the particle showed a wide size distribution. Right, when both HMTA and PVP were used, uniform Eu,Gd-NMOFs were obtained.

synthesis with Gd^{3+}, Eu^{3+}, and H_2IPA in a polar aprotic DMF and THF mixed solvent [84]. However, the method has poor size controls over the NMOF products. As manifested in **Figure 3.1a**, when using different amounts of H_2IPA, Eu,Gd-NMOFs of varied morphologies were obtained, but all the products showed a wide size distribution (**Figure 3.1a**). Moreover, Eu,Gd-NMOFs made by this method were very quickly degraded in water (data not shown), which is a potential problem for bioapplications. To address the issue, we added HMTA to the reaction solution. HMTA increased the pH of the initial reaction solution from ~5.0 to ~8.15, and as such promoted H_2IPA ionization and coordination with Gd^{3+} and Eu^{3+} [85]. Furthermore, we also included PVP as part of the precursors, which was bound to the growing nanoparticle surface to improve the particle stability and control their growth. By adding HMTA and PVP to the reactants, Eu,Gd-NMOFs of narrow size distribution were obtained in a DMF/water mixed solvent (**Figure 3.1b**). As a comparison, without the two agents, no NMOF was formed at the same condition (data not shown).

Transmission emission microscope (TEM) shows that the resulting Eu,Gd-NMOFs were spherical and had an average size of 50 ± 12 nm (**Figure 3.2a and 3.2b**). The Eu,Gd-NMOFs were very stable in aqueous solutions, which is rare among NMOFs [82]. However, the particles were still decomposed when the aqueous solution had a relatively high ionic strength, for instance PBS. This is presumably due to transmetallation and lanthanides binding with PO_4^{3-}. To further improve the particle stability, a silica coating was imparted to the surface of Eu,Gd-NMOFs. Specifically, we followed a Stöber method [86, 87] and used both TEOS and APTES as silane precursors in the coating. The resulting Eu,Gd-NMOF@SiO_2 particles have a coating thickness of ~ 30 nm and an overall diameter of 100 ± 20 nm (**Figure 3.2c**). X-ray diffraction (XRD) analysis found a broad peak at around 22.5° (2θ) (**Figure 3.2d**), which corresponds to the

diffraction by Eu,Gd-NMOFs (JCPDS No. 01-086-1561). Similar results were observed by others in previous studies [88]. FT-IR found absorbance at 1609 cm^{-1} and 1558 cm^{-1}, for Eu,Gd-NMOF and Eu,Gd-NMOF@SiO_2 respectively (**Figure 3.2e**). This absorbance corresponds to C=O stretch, confirming successful H_2IPA coordination in the system. For as-synthesized Eu,Gd-NMOFs, there was broad absorbance at around 3600 cm^{-1}, suggesting residual PVP coating on the nanoparticles (**Figure 3.2e**). Meanwhile, no characteristic HMTA absorbance at

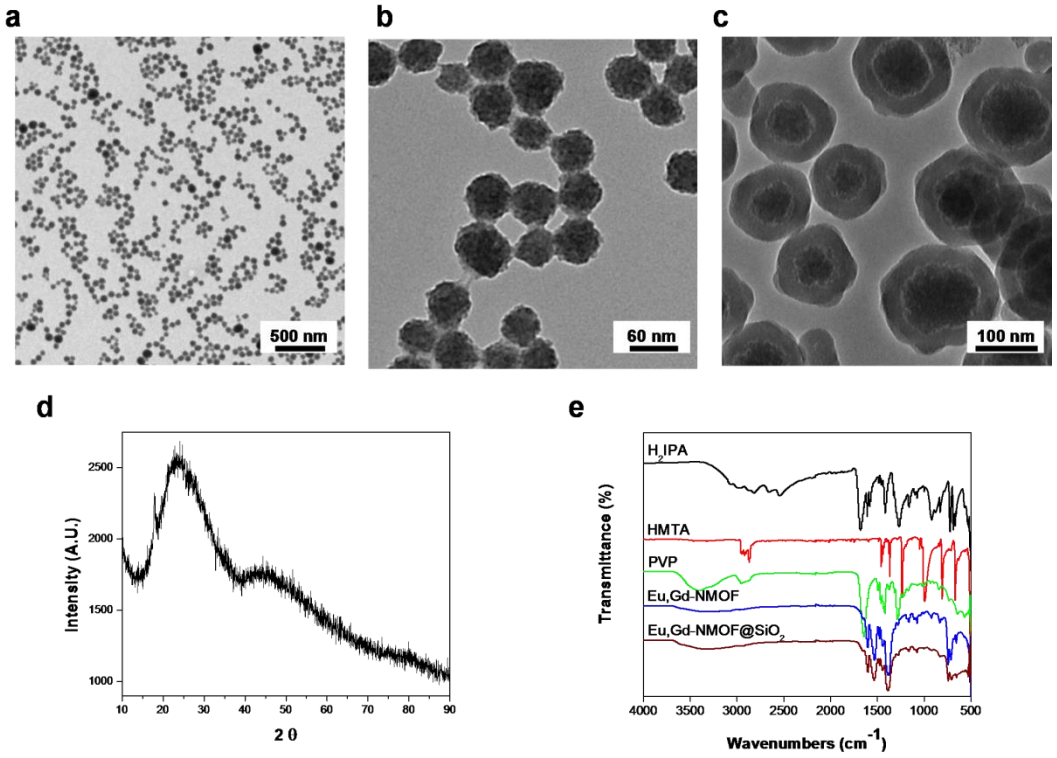

Figure 3.2. Characterization of Eu,Gd-NMOF@SiO_2. (a,b) TEM images of as-synthesized Eu,Gd-NMOF nanospheres in large scale. (c) TEM image of the core-shell structure of Eu,Gd-NMOF@SiO_2 (protection SiO_2 layer ~30 nm). (d) XRD pattern of Eu,Gd-NMOF@SiO_2 nanospheres. (e) FT-IR spectra of H_2IPA, HMTA, PVP, Eu,Gd-NMOFs, and Eu,Gd-NMOF@SiO_2 nanospheres.

1370 cm^{-1} (attributed to C-N stretch) was observed with Eu,Gd-NMOF, suggesting minimal adsorption of HMTA on particle surface (**Figure 3.2e**).

Optical and magnetic properties of Eu,Gd-NMOF@SiO_2

Eu,Gd-NMOF@SiO_2 nanoparticles absorb at around 280 nm (**Figure 3.3a**) and have strong emission at 594 nm and 620 nm (**Figure 3.3b**). These two emission peaks are attributed to $^5D_0 \rightarrow {}^7F_1$ and $^5D_0 \rightarrow {}^7F_2$ transition, respectively [89-91]. Such fluorescence can be utilized to track the nanoparticles in vitro and in histology studies.

The MRI contrast ability of the Eu,Gd-NMOF@SiO_2 nanoparticles was evaluated by phantom studies on a 7T magnet. Briefly, Eu,Gd-NMOF@SiO_2 nanoparticles of increased concentrations were dispersed in 1% agarose gel and the samples were scanned by MRI using SEMS and FSEMS sequences. For both T_1- and T_2-weighted imaging, the signals were clearly concentration dependent. Specifically, significant signal enhancement was observed in T_1 images at elevated concentrations; on the contrary, in T_2 images, signal reduction was observed at high particle concentrations. Based on the imaging results, it was deduced that r_1 was 38 $mM^{-1}s^{-1}$ and r_2 was 222 $mM^{-1}s^{-1}$ (**Figure 3.3c**). These relaxivity values are much higher than commonly used clinical contrast agents such as Gd-DTPA (r_1 of 3.10 $mM^{-1}s^{-1}$) and Feridex (r_2 of 117 $mM^{-1}s^{-1}$) [92]. The exact mechanisms behind the high r_1 and r_2 are unclear, but may be attributed to the rigid confinement of Gd^{3+} in the nanosystem and slow interexchange of Gd^{3+} with water molecules [93]. The r_2/r_1 ratio is 5.8, which is at the boundary between conventionally defined T_1 and T_2 agents [94].

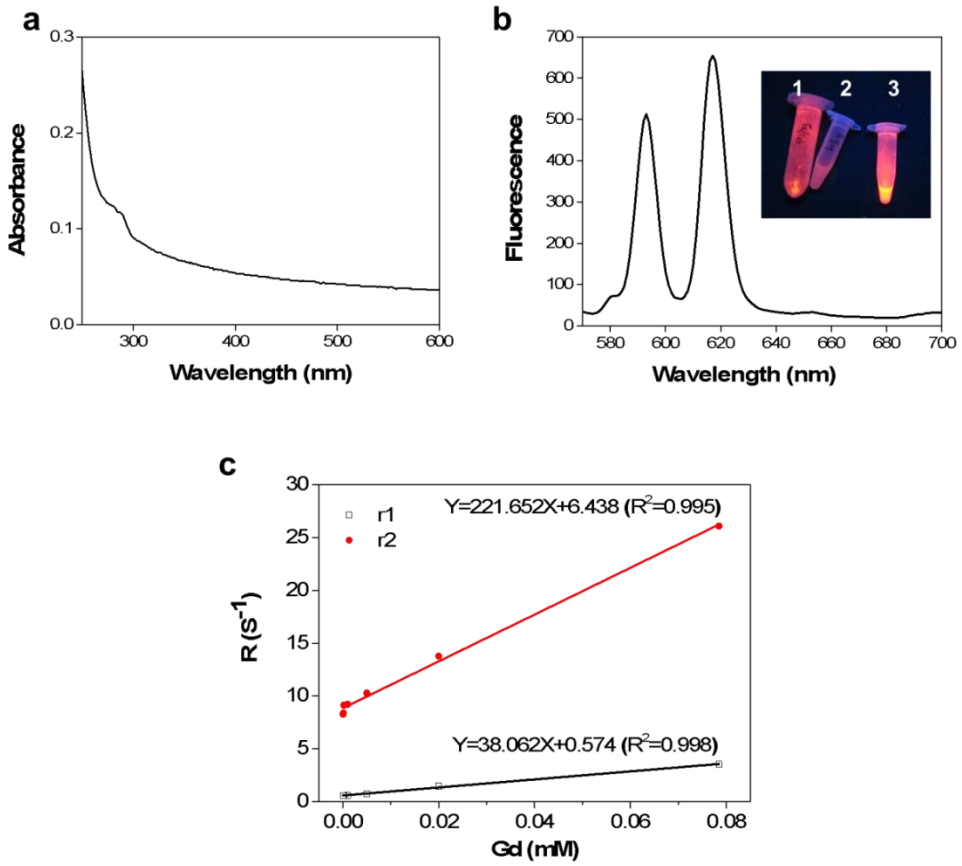

Figure 3.3. Optical and magnetic properties of Eu,Gd-NMOF@SiO_2 (a) UV-vis absorbance of Eu,Gd-NMOF@SiO_2 nanospheres. (b) Fluorescent spectrum of Eu,Gd-NMOF@SiO_2. The inset is a photograph of (1) Eu,Gd-NMOF@SiO_2 powder, (2) water, and (3) aqueous solution of Eu,Gd-NMOF@SiO_2. (c) Linear correlation between R_1 (T_1^{-1})/ R_2 (T_2^{-1}) and Gd concentration. r_1 and r_2 relaxivities were 38 $mM^{-1}s^{-1}$ and 222 $mM^{-1}s^{-1}$, respectively.

Nanoparticle stability and cytotoxicity

The stability of Eu,Gd-NMOF@SiO_2 nanoparticles was studied by monitoring fluorescence change in different solutions. These include aqueous solutions with pH ranging from 3 to 11 and PBS. It was observed that the Eu,Gd-NMOF nanoparticles were very stable

when the pH was maintained between 4-9, and only degraded when the pH was above 10 or below 4 (**Figure 3.4a**), suggesting great resistance of the particles against pH changes. On the

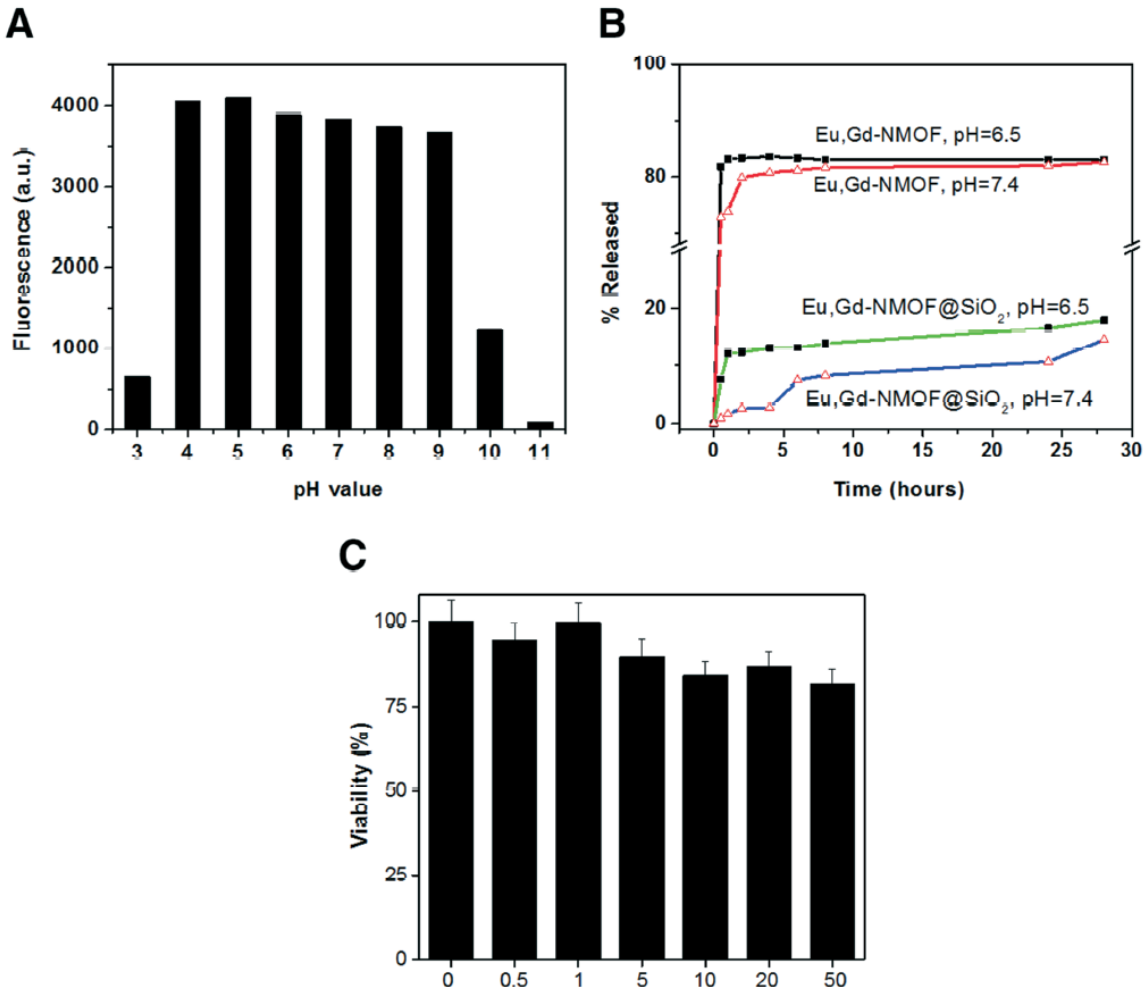

Figure 3.4. Stability and cytotoxicity. (a) Fluorescence intensity (ex/em: 360/595 nm) change when Eu,Gd-NMOF@SiO_2 nanospheres were incubated in aqueous solutions of different pH. (b) Gd^{3+} release profiles of Eu,Gd-NMOFs and Eu,Gd-NMOF@SiO_2 nanospheres in PBS (pH = 6.5 and 7.4). (c) Cell viability, assessed by MTT assays with U87MG cells. Eu,Gd-NMOF@SiO_2 nanospheres with a Gd concentration ranging from 0 to 50 μM were incubated with cells.

other hand, Eu,Gd-NMOFs were much more labile in PBS, and were largely dissolved within one hour (**Figure 3.4b**). With the silica coating, however, Eu,Gd-NMOF@SiO_2 showed

significantly enhanced stability, showing no fluorescence drop in PBS for at least 28 hours (**Figure 3.4b**).

Cytotoxicity and cell uptake studies

Cytotoxicity of the nanoparticles were evaluated by MTT assays with U87MG cells, which are a human glioblastoma cell line. We found no detectable cytotoxicity with Eu,Gd-NMOF@SiO_2 nanoparticles even at the highest concentration investigated (20 μM Gd^{3+}), indicating good biocompatibility.

Next, we investigated whether Eu,Gd-NMOF@SiO_2 can be visualized by MRI when internalized by cells. To investigate, we conjugated c(RGDyK), a cyclic peptide with high binding affinity against integrin $\alpha_v\beta_3$ [95], to the surface of Eu,Gd-NMOF@SiO_2. This was achieved by covalently linking the primary amine of c(RGDyK) and the amine groups on Eu,Gd-NMOF@SiO_2 surface using BS^3 as a homo-dimer crosslinker. U87MG cells were then incubated with RGD-Eu,Gd-NMOF@SiO_2 and Eu,Gd-NMOF@SiO_2 nanoparticles for 1 hour. Notably, U87MG cells are high in integrin $\alpha_v\beta_3$ expression [96]. Under a fluorescence microscope, we observed a significant increase of intracellular red fluorescence, suggesting efficient internalization of RGD-Eu,Gd-NMOF@SiO_2 (**Figure 3.5a**). As a comparison, Eu,Gd-NMOF@SiO_2 nanoparticles showed low cell uptake, indicating that the uptake was mainly mediated by RGD-integrin interaction.

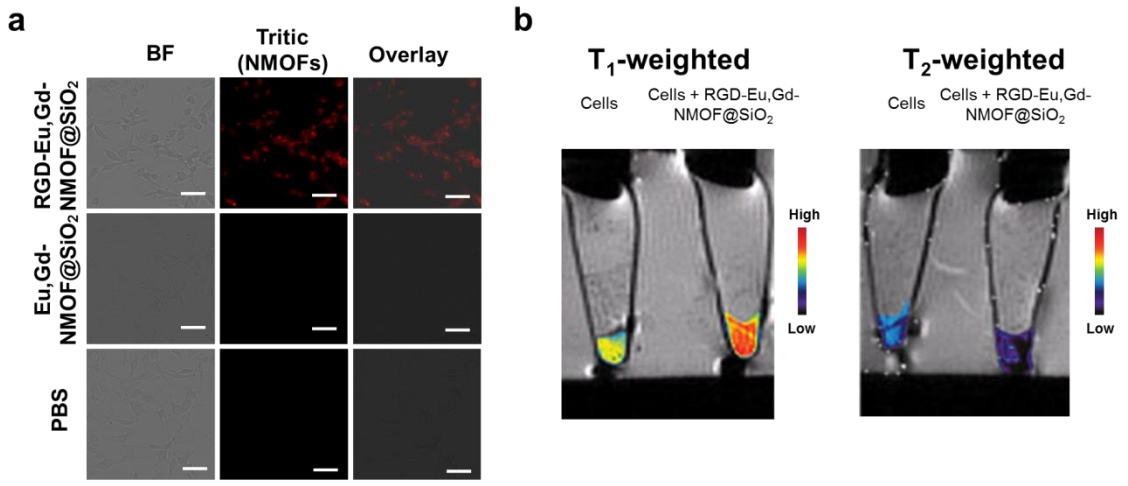

Figure 3.5. Cell fluorescence images and MRI. (a) Fluorescent images of U87MG cells that had been incubated for 1h with Eu,Gd-NMOF@SiO_2 or RGD-Eu,Gd-NMOF@SiO_2. Scale bars: 50 µm. (b) T_1- and T_2-weighted MRI of cells that had, or had not, been incubated with RGD-Eu,Gd-NMOF@SiO_2.

Such RGD-Eu,Gd-NMOF@SiO_2 treated cells were also collected as cell pellets and scanned by MRI. On T_1-weighted images, significant signal enhancement was observed with cells that had been incubated with nanoparticles relative to those that had been not (**Figure 3.5b**). This is attributed to hyperintensities induced by RGD-Eu,Gd-NMOF@SiO_2 nanoparticles. Meanwhile, significant signal reduction was observed on T_2-weighted images (**Figure 3.5b**), which was attributed to hypointensities induced by the NMOFs. These results confirm that Eu,Gd-NMOF@SiO_2 labeled cells can be visualized by both T_1 and T_2 weighted MRI as well as by fluorescence microscopy.

In Vivo MRI

For proof-of-concept, we investigated dual-mode contrast capacity of Eu,Gd-NMOF@SiO_2 in two in vivo studies. In the first study, we intratumorally injected Eu,Gd-

NMOF@SiO_2 (0.8 mg/kg in 100 µl PBS, n=3) to U87MG models and scanned the animals on a 7T magnet. Similar to the in vitro studies, relative to the pre-scans, there was significant signal enhancement on T_1-weighted images and signal reduction on T_2-weighted images (**Figure 3.6a**

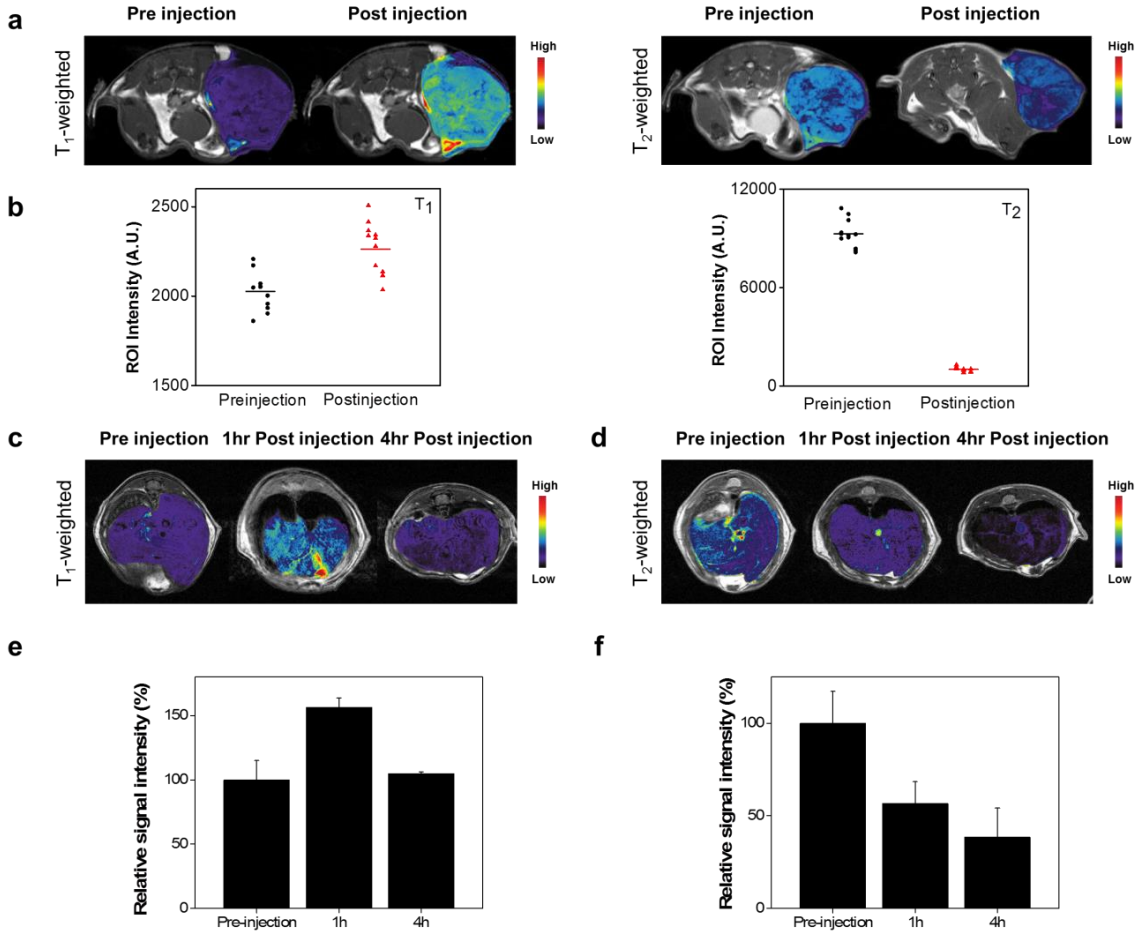

Figure 3.6. In vivo MRI studies. (a) Axial T_1- and T_2-weighted images, taken before and after intratumoral injection of Eu,Gd-NMOF@SiO_2 nanospheres. (b) Signal change before and after Eu,Gd-NMOF@SiO_2 nanosphere injection, based on ROI analysis on multiple slides from (a). (c) Axial T_1-weighted images of the liver, acquired before and after intravenous injection of Eu,Gd-NMOF@SiO_2 nanospheres. (d) Axial T_2-weighted images of the liver, acquired before and after intravenous injection of Eu,Gd-NMOF@SiO_2 nanospheres. (e, f) Change of signals in the liver, based ROI analysis on imaging results from (c) and (d), respectively.

and 3.6b). Specifically, the average signals in tumors were increased by 12 ± 6% on T_1-weighted images after injection and decreased by 89 ± 2% on T_2-weighted images. In the second study, Eu,Gd-NMOF@SiO_2 nanoparticles were intravenously injected (0.8 mg/kg) into balb/c mice and T_1- and T_2-weighted images of the liver area were acquired both before as well as 1 and 4 h after the injections (**Figure 3.6c and 3.6d**). It is well known that nanoparticles after systemic injection are efficiently accumulated in the liver, such as through uptake by Kupffer cells [97]. Region of interest (ROI) analysis showed that relative to the prescans, signals in the liver were increased to 157 ± 9% on T_1-weighted images at 1 h. Interestingly, the signal fell back at 4 h (105 ± 2% relative to the prescans, **Figure 3.6e**). This is probably attributed to too high a concentration of Eu,Gd-NMOF@SiO_2 in the liver at the time point, which leads to signal saturation. A similar phenomenon was observed by others [98, 99]. Meanwhile, on T_2-weighted images, signals in the liver were decreased to 57 ± 12% on T_2 images at 1 h and to 38 ± 16% at 4 h (**Figure 3.6f**). Overall, these results confirm the feasibility of using Eu,Gd-NMOF@SiO_2 nanoparticles as a T_1-T_2 dual-mode imaging probe.

Conclusions

We have developed a novel and facile procedure to synthesize a highly hydrostable metal-organic framwork, Eu,Gd-NMOFs. Silica coated Eu,Gd-NMOFs exhibit high longitudinal (38 $mM^{-1}s^{-1}$) and transversal (222 $mM^{-1}s^{-1}$) relaxivities, and strong fluorescence. In vitro and in vivo MRI studies confirmed that Eu,Gd-NMOFs can induce both hyperintensities on T_1-weighted images and hypointensities on T_2-weighted images, suggesting great potential of the probe as a novel T_1-T_2 dual-mode imaging probe. The nanoparticle surface can be easily coupled with a variety of targeting moieties for different imaging purposes. It is also possible to impart onto the solid silica layer a mesoporous silica layer into which drug molecules can be loaded.

These make the nanoparticles a modifiable platform technology that can find wide applications in modern imaging and theranostics.

CHAPTER 4

NANOSCINTILLATOR-MEDIATED X-RAY INDUCIBLE PHOTODYNAMIC THERAPY FOR *IN VIVO* CANCER TREATMENT[3]

[3]*Hongmin Chen, Geoffrey D. Wang, Yen-Jun Chuang, et al. 2015*. Nano Letters. *15(4):2249-2256. Reprinted here with permission of the publisher.*

Abstract

Photodynamic therapy is a promising treatment method, but its applications are limited by the shallow penetration of visible light. Here we introduce a novel X-ray inducible photodynamic therapy (X-PDT) approach that allows PDT to be regulated by X-rays. This is achieved with an integrated nanosystem comprised of a core of a nanoscintillator and a mesoporous silica coating loaded with photosensitizers. Upon X-ray irradiation, the nanoscintillator converts X-ray photons to visible photons to activate the photosensitizers.

Keywords: nanomedicine, X-PDT, nanoscintillator, radioluminescence nanophosphors, singlet oxygen, cancer treatment

Introduction

Photodynamic therapy (PDT) is a relatively new modality for cancer treatment [100]. PDT consists of three essential components; light, oxygen, and a photosensitizer [22, 100]. Photosensitizers, often pharmacologically inactive without illumination, can be activated by light of a specific wavelength. This activation is followed by transfer of energy to nearby oxygen molecules to generate cytotoxic reactive oxygen species (ROS), most importantly singlet oxygen($^1O_2$) [22]. Compared to other common treatment modalities (*e.g.* radiotherapy and chemotherapy), PDT is minimally invasive, induces low systematic toxicity, and causes little intrinsic or acquired resistance [21-23]. One primary downside of PDT, however, is its inability to treat tumors located deep under the skin due to the short penetration depth of light in tissues[101]. This problem can be partially alleviated by advanced light-delivering technologies that allow for illumination of certain internal cavities, such as the bladder, prostate, lung, and esophagus [102, 103]. Nonetheless, it is considered challenging or impossible for conventional

PDT to treat tumors of large volumes[104] or multiple loci[105]. Recently, there have been exciting developments of novel PDT derivatives, such as two-photon PDT or upconversion

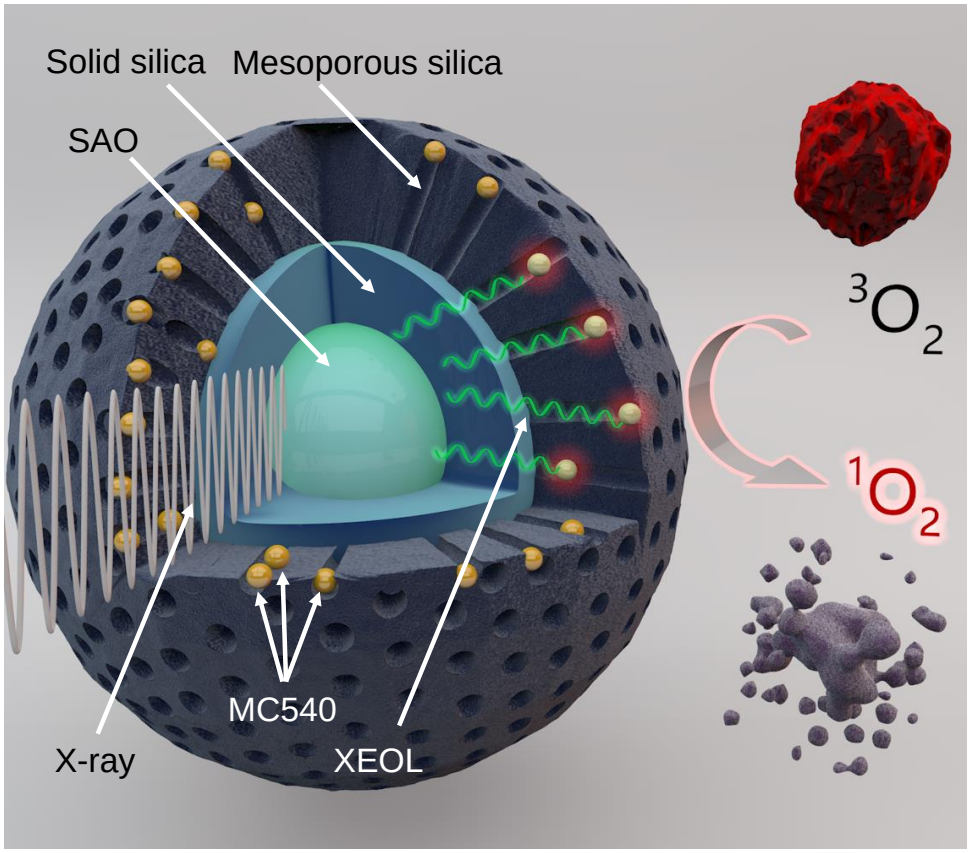

Scheme 4.1. Schematic illustration of the working mechanism of X-PDT. A nanoscintillator core made of SAO is coated with two layers of silica--an inner solid layer and an outer mesoporous layer. Into the mesoporous silica layer, a photosensitizer, MC540, is loaded. Under X-ray irradiation, SAO converts X-rays to visible light photons (XEOL). The visible light photons, in turn, activate near-by MC540 molecules to produce cytotoxic $^1O_2$ that destroys nearby cancer cells. $^3O_2$, ground-state oxygen.

nanoparticle-mediated PDT, which aim to minimize tissue interference and improve penetration depth [21, 67, 101, 106, 107]. However, given that the methods are powered by light, the treatment efficiency may still be surface-weighted.

Experiments and Results

We herein introduce a novel X-ray induced PDT (X-PDT) methodology, which, as the name suggests, regulates photosensitizer activation by X-rays. The rationale is that unlike visible or NIR light, X-ray photons have practically unlimited penetration power in body tissues. Should PDT be X-ray-activatable, the treatment could be initiated from virtually any part of a body with equal efficiency [21]. The key element of our design is an integrated nanosystem, comprised of a core made of $SrAl_2O_4$:1%Eu^{2+} (hereafter referred to as SAO), and a silica coating, onto which merocyanine 540 (MC540), a photosensitizer, is loaded (**Scheme 4.1**). SAO is a scintillator material, which can convert X-ray photons to visible photons, a phenomenon known as X-ray excited optical luminescence (XEOL)[108, 109]. It is postulated that under X-ray irradiation, the SAO nanoparticle can relay energy in the form of green light to the near-by MC540 molecules. MC540, with an excitation wavelength overlapping the XEOL of SAO, is activated by the emission generated *in situ* to produce cytotoxic $^1O_2$. The hypothesis has been confirmed both *in vitro* and *in vivo*. While little toxicity is observed when low-intensity X-ray (0.5 Gy), MC540, or SAO nanoparticles are applied individually, the combination of the three efficiently kills surrounding tumor cells. In particular, we observed in murine xenograft models that X-PDT can induce prominent tumor growth arrest and shrinkage, while leaving the normal tissues unaffected. It is also noted that SAO nanoparticles, unlike many other materials under investigation, are highly hydrolytic. Even with the silica coating, they are reduced to non-toxic ions and excreted from the body after the treatment, causing no long-term side effects to the host. Overall, X-PDT inherits the benefits of PDT and meanwhile, boasts unlimited penetration capacity owing to using X-ray as the energy source. These properties suggest X-PDT as a novel and powerful treatment modality with great perspectives in the clinic, especially in oncology.

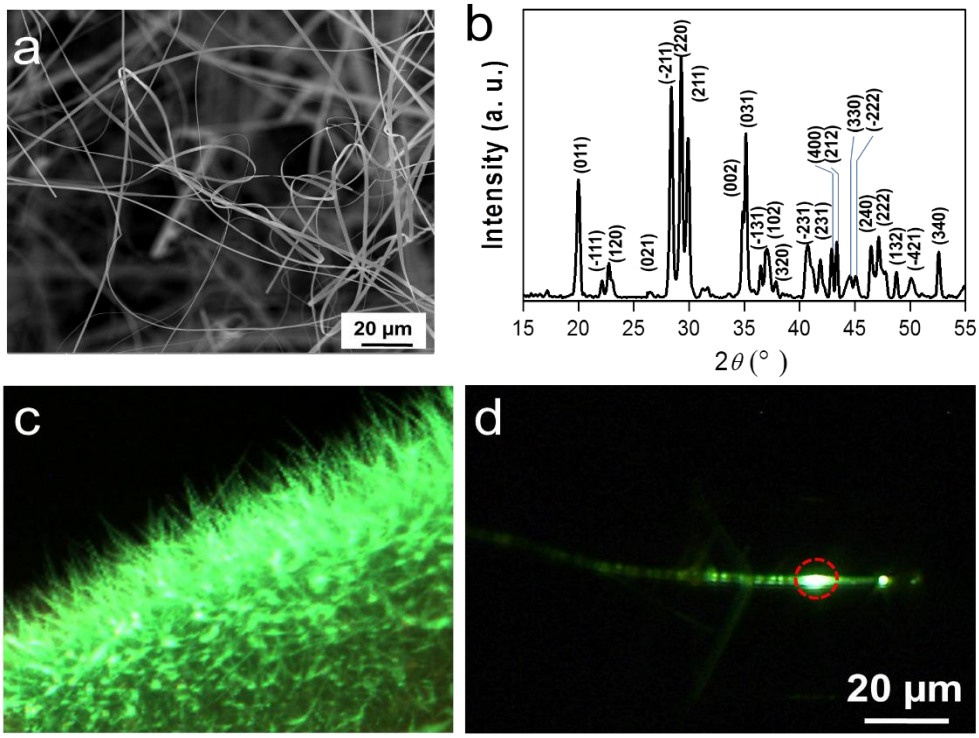

Figure 4.1. Structure, composition, and optical properties of raw SAO. a, Scanning electron microscopy (SEM) image of as-synthesized SAO. b, X-ray diffraction (XRD) analysis result. The main product is monoclinic $SrAl_2O_4$ (JCPDS #74-0794). c, The raw SAO product under 365-nm UV irradiation. Strong green fluorescence was emitted from the material. Image was taken by a digital microscope. d, Image of a single SAO wire struck by a narrow X-ray beam (the hit point was circled by red dashed lines). The resulting green emission was disseminated to the surroundings or along the wire.

Synthesis, surface modification, and MC540 loading of SAO nanoparticles

Raw SAO was synthesized by carbothermal reaction using a vapor-phase deposition method [110, 111]. Briefly, $SrCO_3$, Al_2O_3, Eu_2O_3 and graphite powders were mixed and heated in a tube furnace system at 1450 °C for 2 h under an argon flow with pressure maintained at 5 Torr. The as-synthesized SAO was wire-like (**Figure 4.1a**) and the main structure was identified

to be monoclinic $SrAl_2O_4$ (JCPDS #74-0794) (**Figure 4.1b**) [110, 111]. The material emits green

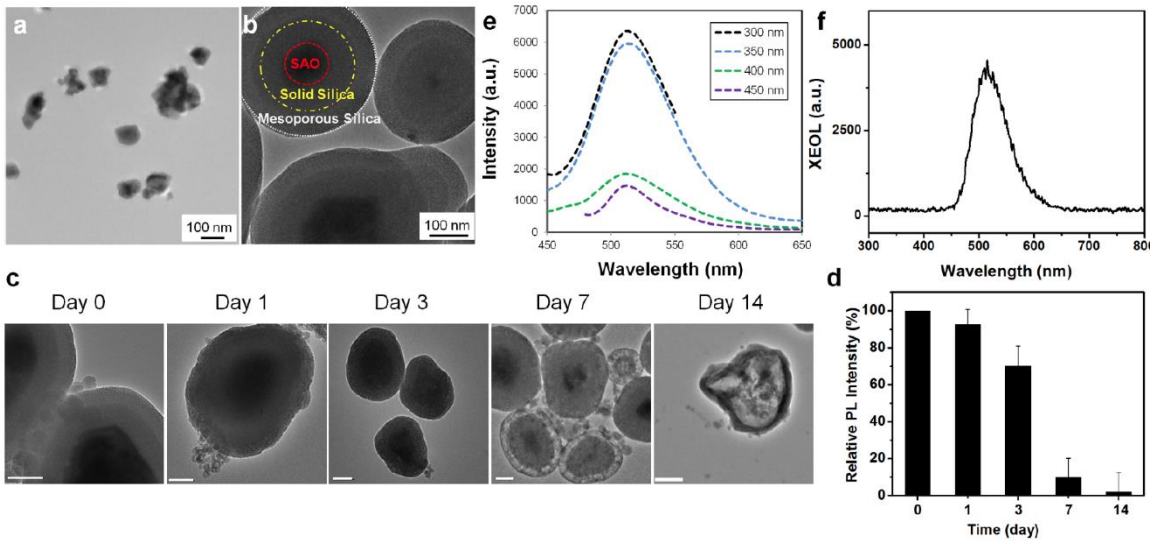

Figure 4.2. Morphology and optical properties of $SAO@SiO_2$ nanoparticles. a, Transmission electron microscopy (TEM) image of bare SAO particles. b, TEM image of $SAO@SiO_2$ nanoparticles. The silica coating consists of an inner solid layer and an outer mesoporous layer. c, Stability of $SAO@SiO_2$ nanoparticles. $SAO@SiO_2$ nanoparticles were incubated in a simulated body fluid [22, 23] prepared by following a published protocol[22,23]. The SAO cores were stable at the beginning but were then degraded gradually. After 14 days, only empty silica shells were observed under TEM. Scale bars, 100 nm. d, Change of photoluminescence (PL) intensity (ex/em: 360nm/520 nm), relative to the PL at the beginning of the incubation. Coincided with the TEM observations in c, there was a gradual drop of the PL intensity over time. The error bars represent ± s.e.m. of three independent experiments. e, Photoluminescence spectra of $SAO@SiO_2$ nanoparticles, taken under excitation by different wavelengths of light (300-450 nm). Maximum emission was observed at ~520 nm. f, XEOL spectrum of $SAO@SiO_2$ nanoparticles. Emission also peaked at ~520 nm.

photoluminescence and XEOL under UV and X-ray irradiation, respectively (**Figure 4.1c, d**). Both types of luminescence are attributable to the $4f^6 5d^1 \rightarrow 4f^7$ transition of Eu^{2+} ions in the lattice [112, 113].

The bulkiness of the as-synthesized SAO makes it unsuitable for bio-applications. To reduce its dimensions, the SAO was mechanically ground, followed by sedimentation, filtration and centrifugation, to yield ~150 nm nanoparticles (**Figure 4.2a**). These SAO nanoparticles were then coated with a solid layer of silica, followed by further coating with an outer mesoporous layer (**Figure 4.2b, Supplementary Figure S4.1a, b, d, e**). Each of the two silica layers plays a distinctive role in the nanosystem. The inner, solid silica coating functions as a protection shell that prevents contact between the SAO core and the surrounding aqueous environment (**Supplementary Figure S4.1a, b)**. This is essential because SAO is highly hydrolytic: Bare SAO nanoparticles are completely degraded in 5 min when directly exposed to aqueous solutions (**Supplementary Figure S4.1g)**. With the solid silica coating, the lifetime of SAO nanoparticles in aqueous solutions can be extended to more than 3 days (**Figure 4.2c, d**), which is sufficiently long for therapy purposes. The outer, mesoporous silica coating affords a docking place for small molecules, a strategy commonly used in surface modification of nanoparticles [76, 107]. Notably, for the mesoporous coating, we used both aminopropyltriethoxysilane (APTES) and tetraethyl orthosilicate (TEOS) as silane precursors. The resulting silica coated SAO nanoparticles (SAO@SiO_2 nanoparticles) have multiple amine groups on the surface and are thus slightly positively charged.

SAO@SiO_2 nanoparticles maintain the strong photoluminescence and XEOL of SAO. **Figure 4.2e,f** display emission spectra of SAO@SiO_2 nanoparticles under irradiation by UV/Vis and X-ray light, respectively. Similar to the bulk material, both types of emission were found in

the green spectral region, peaking around 520 nm (**Figure 4.2e, f, Supplementary Figure S4.2**). The emission can be readily visualized on a Maestro small animal imaging system (Supplementary **Figure S4.3a-c**), and even by the naked eye (Supplementary **Figure S4.3d, e**).

Cellular uptake and cytotoxicity studies

Cellular uptake was investigated with U87MG (human glioblastoma) cells. After incubation with SAO@SiO_2 nanoparticles (50 μg/mL) for 1 h, the cells were washed with PBS and imaged under a fluorescence microscope (Supplementary **Figure S4.4a**). Green photoluminescence was observed in all the cells in the scope and was distributed across the cytoplasm but not in the nuclei [44]. This fits the pattern that SAO@SiO_2 nanoparticles were internalized by cells through endocytosis [114, 115], a process that may have been facilitated by electrostatic interactions between the particles and the cell membranes (Supplementary **Figure S4.4a**).

Using MTT (3-(4,5-dimethylthiazol-2-yl)-2,5-diphenyltetrazolium bromide) assays, we then investigated the cytotoxicity of SAO@SiO_2 nanoparticles. We observed no significant viability drop even at high particle concentrations (up to 100 μg/mL, Supplementary **Figure S4.4b**), suggesting good biocompatibility of our SAO@SiO_2 nanoparticles. However, MTT assays are only viable to assess short-term cytotoxicity (*e.g.* within 24 or 72 h) when most of the nanoparticles are still intact. As mentioned above, SAO is highly hydrolytic, and despite the presence of the SiO_2 coating, the nanoparticle core can be degraded in a physiological environment after one week [1, 2] (**Figure 4.2c,d**). The released constituent ions, including Sr^{2+}, $Al(OH)_4^-$ (the primary form at neutral pH)[116], and Eu^{2+}, may affect cell viability differently. To investigate, in a separate study, we incubated bare SAO nanoparticles in water for 1 week to decompose SAO, and then used the hydrolytes for toxicity assessments. There was again no

significant drop of viability, confirming minimal toxicity of the nanoparticles even in the long run (Supplementary **Figure S4.5**). This is not surprising since all the constituent ions have relatively low toxicity profiles. Sr^{2+} and Al^{3+} have been used in clinical medicines for applications such as postmenopausal osteoporosis, antiacid, and bone implants [117-119]. Eu^{2+} is also relatively non-toxic compared to other heavy metals [120].

$^1O_2$ generation by X-PDT

The mesoporous coating allows easy loading of small molecules. Through overnight incubation, MC540 was loaded onto SAO@SiO_2 nanoparticles at a rate of 15 wt%. Despite the heavy loading, the resulting MC540-loaded SAO@SiO_2 nanoparticles, or M-SAO@SiO_2 nanoparticles, remain highly stable in aqueous solutions (Supplementary **Figure S4.6**).

There is a significant overlap between the XEOL of SAO and the excitation wavelength of MC540 (**Figure 4.3a**). It is thus hypothesized that when M-SAO@SiO_2 nanoparticles are irradiated by X-ray, SAO can relay energy in the form of visible photons to MC540 and as a result, produce $^1O_2$. To study the effect, we used a common $^1O_2$ indicator, singlet oxygen sensor green (SOSG) [121, 122]. SOSG is a fluorescent compound which undergoes a structural change in the presence of $^1O_2$. The process is accompanied with an increase of fluorescence (ex/em: 504/525 nm). Hence by measuring the fluorescence change, one can monitor $^1O_2$ generation in solutions or cells[121-123]. Using SOSG, we first studied $^1O_2$ generation with a M-SAO@SiO_2 nanoparticle solution (50 μg/mL) under X-ray irradiation (1 Gy/h, **Figure 4.3b**). Compared to the background, the intensity of 525 nm fluorescence was increased by 8, 25, 35 and 45% after 5, 10, 15, and 20 min X-ray irradiation, respectively (**Figure 4.3b**). Meanwhile, no significant signal increase was observed during the intermissions of X-ray irradiations (**Figure 4.3b**). Similar studies were performed with solutions of MC-540, SAO nanoparticles, and PBS,

all of which showed minimal increase of fluorescence, either with or without X-rays (**Figure 4.3b**). These data suggest that $^1O_2$ can, and only can be produced when all the three components--MC-540, SAO, and X-ray are present, corroborating our hypothesis that $^1O_2$ production is a result of SAO-mediated energy transfer.

The $^1O_2$ production was next examined with U87MG cells, again using SOSG as an indicator. For cells incubated with M-SAO@SiO_2 nanoparticles and irradiated by X-ray, there was a significant enhancement of 525-nm fluorescence. As a comparison, cells treated with nanoparticles only showed minimal fluorescence change (**Figure 4.3c**, Supplementary **Figure S4.7**). By quantifying fluorescence readings from 10 images from each group (Image J, National Institutes of Health), it was determined that the fluorescence was enhanced by 410 ± 29% in cells treated by X-PDT (i.e. nanoparticle + X-ray). As with the observations made in the solutions, cells treated with M-SAO@SiO_2 only (without X-ray) or SAO@SiO_2 nanoparticles (with or without X-ray) showed only a marginal increase of fluorescence, again confirming that it takes the combination of X-ray, MC540, and SAO to generate $^1O_2$ (**Figure 4.3c**).

The produced $^1O_2$ translates to toxicity to cells. **Figure 4.3d** shows a cytotoxicity assay where ethidium homodimer-1 was used to mark dead cells (ex/em: 517/617 nm). Low red fluorescence intensity was observed with U87MG cells treated with X-rays alone (0.5 Gy) or with M-SAO@SiO_2 nanoparticles in the absence of X-ray irradiation (**Figure 4.3d**). In accordance with the $^1O_2$ generation results, the combination of M-SAO@SiO_2 nanoparticles and X-rays resulted in significant increase of red fluorescence within cells (**Figure 4.3d**), accompanied by cell morphology changes (Supplementary Figure **S4.8&S4.9**). The result was further confirmed by MTT assays, which found a viability drop of 62% with X-PDT-treated cells but little toxicity in all the controls (**Figure 4.3e**).

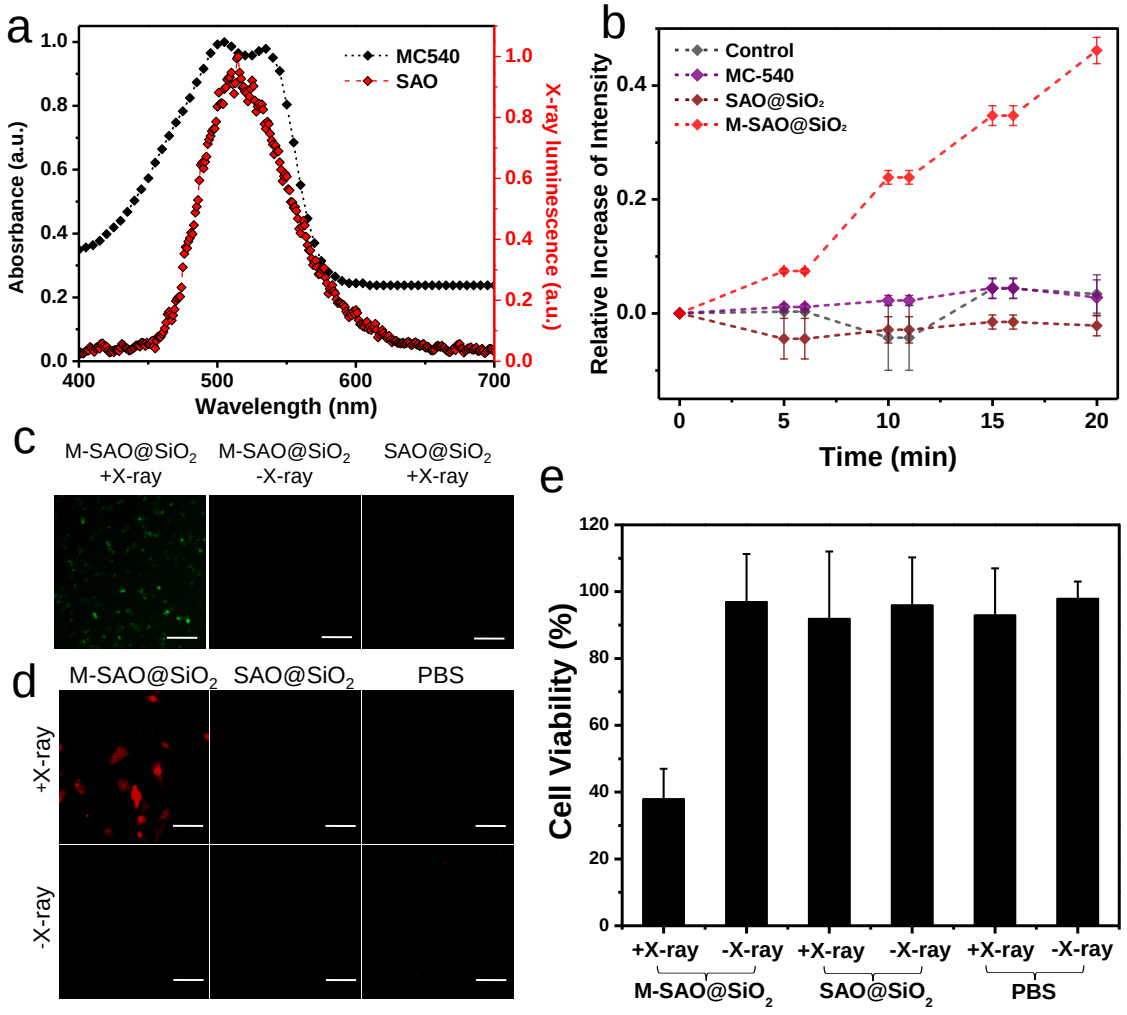

Figure 4.3. X-PDT induced $^1O_2$ production and cytotoxicity. a, Good overlap exists between the XEOL of SAO (red) and the absorbance of MC540 (black). b, Comparison of $^1O_2$ production, using SOSG as an indicator (ex/em: 504/525 nm). Increased levels of $^1O_2$ were only observed with M-SAO@SiO_2 nanoparticles under X-ray irradiation. Notably, there was a 1-minute intermission after each 5-minute X-ray irradiation cycle. The error bars represent ± s.e.m. of three independent experiments. c, X-PDT induced $^1O_2$ generation in cells. Similar to

observations in b, enhanced fluorescence at 525-nm--which signals $^1O_2$ generation--was only observed when cells were treated with M-SAO@SiO_2 nanoparticles and in the presence of X-ray irradiation. Scale bars: 100 μm. d, Cytotoxicity studies, using ethidium homodimer-1 as a dead cell marker (a.k.a. dead assay). Correlated to the observations in c, cytotoxicity was observed when M-SAO@SiO_2 nanoparticles and X-ray were used in combination. Ex/em: 530 nm/635 nm. Scale bars, 50 μm. e, MTT assay results. Cell viability was significantly reduced when cells were treated with X-PDT (M-SAO@SiO_2 nanoparticles plus X-ray), and was minimally affected in other conditions. The error bars represent ± s.e.m. (n = 4 per group).

In vivo therapy studies

An *in vivo* therapy study was conducted in murine subcutaneous tumor models. Briefly, 30 U87MG tumor bearing mice were randomized to receive the following treatments (n = 5): 1) M-SAO@SiO_2 nanoparticles + X-ray, 2) M-SAO@SiO_2 nanoparticles only, 3) SAO@SiO_2 nanoparticles + X-ray, 4) M-SAO@SiO_2 nanoparticles only, 5) PBS + X-ray, and 6) PBS only. For Group 1-4, SAO@SiO_2 or M-SAO@SiO_2 nanoparticles were intratumorally injected into the animals (4.25 mg SAO/kg, in 50 μL of PBS solution, 1.7 mg SAO/ml, single dose). For groups 5 and 6, 50 μL of PBS was intratumorally injected. For animals receiving X-rays (Group 1, 3, and 5), the irradiation was applied to the tumor area (1 Gy/h for 30 min, beam diameter 6 mm) 5 minutes after particle injection. Notably, this irradiation dose is far below those used in clinical radiotherapy (60-80 Gy for solid epithelial tumors, 5 Gy per fraction)[124-126].

Relative changes of tumor volume (V/V_0) are graphed in **Figure 4.4a**. For the treatment group (Group 1), tumor growth was immediately arrested after the treatment, followed by significant tumor shrinkage starting from day 6. On day 12, the average tumor volume was reduced to 60.2 ± 6.9% (**Figure 4.4a**). On day 16, three of the five animals showed almost

impalpable tumors, leaving only thin scabs at the original tumor sites (**Figure 4.4b,**

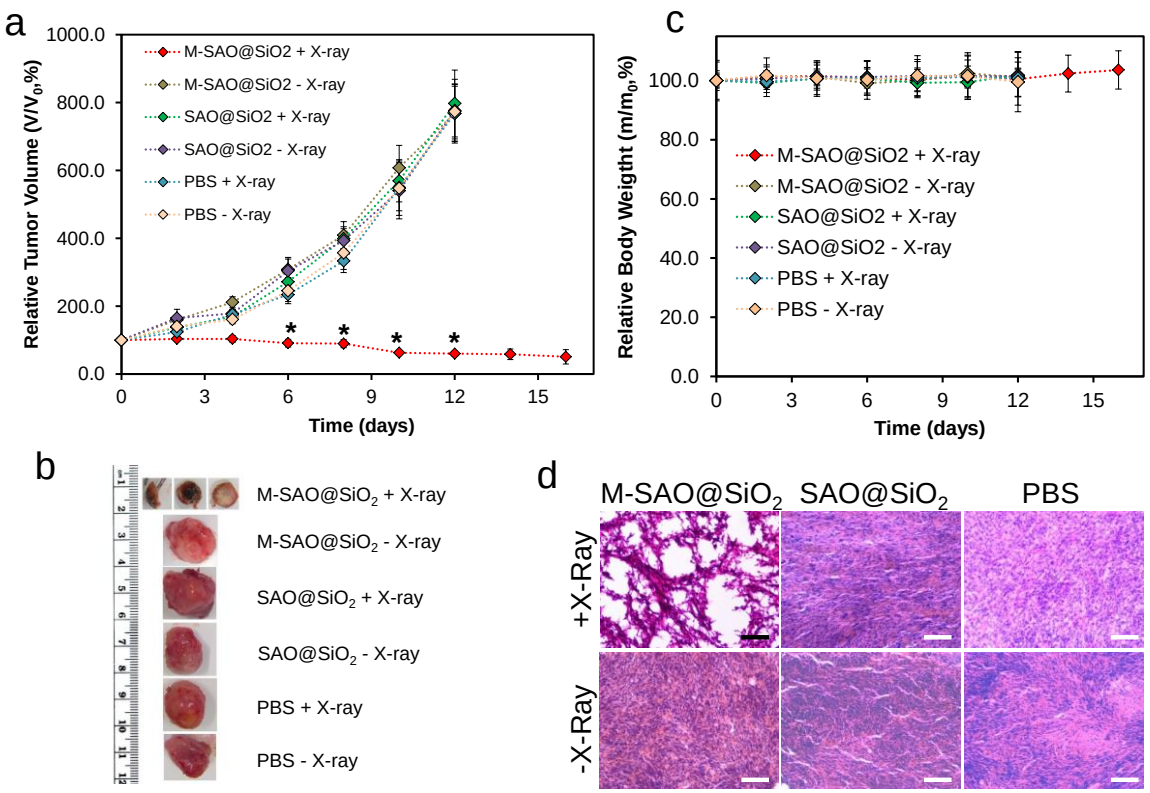

Figure 4.4. X-PDT for *in vivo* tumor therapy. a, Tumor growth curves (V/V_0%, n = 5). Significant tumor suppression and shrinkage was observed with animals injected with M-SAO@SiO_2 nanoparticles and irradiated by X-ray. In all the control groups, tumors grew rapidly and in a comparable pace. By day 14, all the animals in the control groups had either died or been euthanized for meeting at least one humane end point. The error bars represent ± s.e.m. *P < 0.05. b, Photographs of representative tumors taken from Groups 1-6. c, Body weight curves. No significant decrease of body weight was observed with X-PDT-treated animals. The error bars represent ± s.e.m. d, H&E staining on tumor tissues taken from Groups 1-6. Compared to all the controls, where densely packed neoplastic cells were observed throughout the mass, tumors treated by X-PDT manifested drastically impacted tumor architectures and significantly reduced cell density. Scale bars, 100 µm.

Supplementary Figure S4.10). All the animals in Group 1 were healthy throughout the whole study (**Figure 4.4c)**. On the contrary, all the animals in the control groups showed rapid and comparable tumor growth (Figure 4a, Supplementary Figure S10). On day 12, tumor volumes were increased by 768.0 ± 87.0%, 797.4 ± 98.6%, 776.9 ± 91.9%, 767.4 ± 80.8%, and 773.1 ± 80.4% for Groups 2-6, respectively (**Figure 4.4a,b**). By day 14, all the animals in the control groups had either died or been euthanized due to meeting at least one humane end point (Supplementary **Figure S4.11**).

Post-mortem H&E staining found densely packed neoplastic cells in tumors from the control groups (**Figure 4.4d**, Supplementary **Figure S4.12a**). As a comparison, the treatment group showed drastically impacted tumor architectures and significantly reduced cell density (**Figure 4.4d**, Supplementary **Figure S4.12a**), with many regions void of viable cells. Meanwhile, there was no detectable impact to the normal tissues, such as the heart, liver, spleen, kidneys, and skin (Supplementary **Figure S4.12b**). This is attributed to the high selectivity of the X-PDT treatment (narrow and controllable beam irradiation), and also, the low toxicity and high biodegradability of SAO nanoparticles.

To further assess the excretion of SAO particles, in a separate study, we intravenously injected M-SAO@SiO_2 nanoparticles to normal balb/c mice. On day 16, we sacrificed the animals and evaluated the remaining Sr contents in different organs by inductively coupled plasma mass spectrometry (ICP-MS) analysis. For all the organs analyzed, we found that Sr contents were comparable to the background, confirming the efficient clearance of the particles (**Figure 4.5a**). All of the injected animals were healthy throughout the whole study, with no weight loss (**Figure 4.5b**), skin toxicity, or any signs of morbidity.

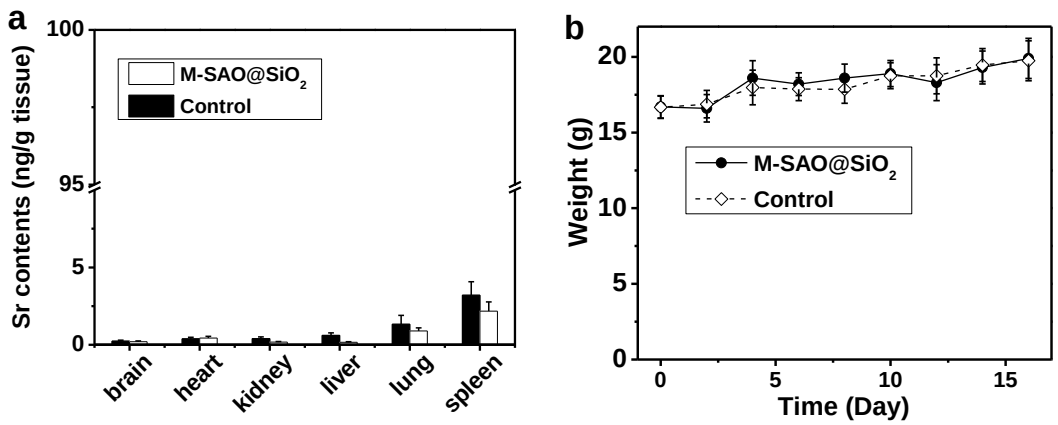

Figure 4.5. Biodistribution and change of body weight after intravenous injection of M-SAO@SiO_2 nanoparticles. a, Strontium (Sr) contents in different organs on day 16. The results were based on ICP analysis results on tissue samples. No difference in Sr contents was observed relative to control animals that had not been injected with M-SAO@SiO_2 nanoparticles. This observation suggests that the SAO had been mostly degraded and excreted by day 16. The error bars represent ± s.e.m. of three independent experiments. b, Body weight changes. No significant difference in body weight was observed between normal animals and those injected with M-SAO@SiO_2 nanoparticles. The error bars represent ± s.e.m. (n=5 mice per group).

Discussions and Conclusion

In the present study, the *in vivo* investigations were performed in subcutaneous tumor models. Owing to the excellent tissue penetration ability of X-rays, however, X-PDT has all the potential to treat tumors located deep under the skin. This was supported by a cytotoxicity study where U87MG cells were treated with M-SAO@SiO_2-mediated X-PDT, but with 4.5-cm thick pork positioned between the X-ray source and cells (Supplementary **Figure S4.13**). No significant difference in viability drop was observed relative to the cells receiving X-PDT but under direct X-ray exposure (35 ± 9% vs. 38 ± 9% for cells treated with and without pork,

respectively, $P < 0.05$, Supplementary **Figure S4.14**). This observation confirms the independence of X-PDT to tissue depth, a quality that is missing in conventional PDT [127].

A SAO-based nanoscintillator was used for X-ray-to-visible conversion, a step that is key to the X-PDT system. SAO is a well-known inorganic luminescent material, and has been extensively used in areas such as safety indication, emergency lighting, road signs, billboards, graphic arts, interior decoration, lamp industry, radiation dosimetry, and color display [128]. In addition to its excellent optical properties, there are at least two more advantages of SAO for the current application. First, SAO forms an excellent energy pair with MC540, ensuring efficient intra-particle energy transfer that eventually leads to $^1O_2$ production. Second, SAO is highly hydrolytic and its hydrolytes are minimally toxic[129]. With silica as a semi-stable protection shell, the SAO core remains intact for a time span sufficient for the therapy, and is then reduced to constituent ions that are readily excreted. This property minimizes long-term toxicity to the host, which is a common issue in nanoparticle-based imaging and therapy[67].

X-ray as an energy source is widely used in the clinic for both diagnosis and therapy purposes[108, 130]. This suggests a minor hurdle from an instrument perspective as to the clinical translation of the technology. X-rays can be given to cover either a relatively small area (*e.g.* in external radiotherapy and dental radiography) or a large area (chest X-ray and CT). Both types of X-rays may be employed to power X-PDT. While narrow-beam X-rays may induce more focal and selective damage, X-rays covering a large area may enable X-PDT to treat tumors of multiple loci or tumor metastasis. As shown in the present study, M-SAO@SiO_2 nanoparticles can be delivered directly to the cancerous sites, and the modality in this form resembles brachytherapy (except the need of external X-ray irradiation as a trigger). This approach is expected to find wide applications in the clinic, especially for tumors that are

resistant to radiation therapy. Meanwhile, it is possible to deliver nanoparticles systematically to tumors. For that purpose, a reduced nanoparticle dimension and optimized surface features are needed so as to minimize particle uptake by the reticuloendothelial system (RES) and maximize their accumulation in tumors[131, 132].

Future studies from different perspectives are needed to further improve the efficiency of X-PDT. First, optimize the particle core size, the coating thickness of each silica layer, and the photosensitizer loading efficiency to achieve the most efficient $^1O_2$ production. Second, evaluate other candidate nanoscintillators, many of which have stronger XEOL[108], as transducers. However, a different photosensitizer with a matching excitation wavelength is needed, and the toxicity and biodegradability has to be reassessed. Third, investigate the impact of X-ray intensity and irradiation time on the treatment efficacy of X-PDT. This is important because the efficiency of PDT is often highly dependent on illumination fluence and fluence rate[1].

Overall, we have developed a novel X-PDT methodology which, by employing a SAO nanoscintillator as a transducer, allows photosensitizer activation to be regulated by X-rays. It has come to our attention that the concept of X-ray powered PDT was mentioned previously[21],[133]. To the best of our knowledge, however, the current study is the first to confirm the feasibility of X-PDT or its like's for real *in vivo* applications. An advanced PDT derivative, X-PDT inherits all the benefits of conventional PDT while breaks the shallow penetration depth restraint, thereby opening many new possibilities. X-PDT as a novel and less invasive modality is expected to find wide applications in the battle against cancer as well as other diseases.

Methods

In vitro X-PDT.

U87MG (human glioblastoma) cells (ATCC) were grown in DMEM medium supplemented with 10% FBS and 100 units/mL of penicillin (ATCC). The cells were maintained in a humidified, 5 % carbon dioxide (CO_2) atmosphere at 37 °C. For viability studies, 10^4 U87MG cells were seeded in 96-well plates (Corning) and cultured for 24 h. The cells were then incubated with 50 μg/ml M-SAO@SiO_2 nanoparticles for 1 h. Subsequently, they were washed with PBS for two times, and then exposed to X-ray irradiation for 30 min (1 Gy/h). Cell viability was evaluated by either dead assays (using ethidium homodimer-1 as a dead cell marker, Invitrogen) or MTT assays (Sigma Aldrich) by following the vendor's protocols. For controls, cells were incubated with M-SAO@SiO_2 nanoparticles but were not X-ray-irradiated.

Animal models

All the animal studies conform to the Guide for the Care and Use of Laboratory Animals published by the National Institutes of Health, USA, and a protocol approved by the Institutional Animal Care and Use Committee (IACUC), University of Georgia. Animal models were established by subcutaneous injection of 10^6 U87MG onto the hind legs of 5–6 week athymic nude mice (Harlan).

In vivo X-PDT

Therapy study began 3 weeks after tumor cell inoculation. Animals were randomized to receive the following treatments: 1) M-SAO@SiO_2 nanoparticles + X-ray, 2) M-SAO@SiO_2 nanoparticles only, 3) SAO@SiO_2 nanoparticles + X-ray, 4) M-SAO@SiO_2 nanoparticles, 5) PBS + X-ray, and 6) PBS only (n = 5). Nanoparticles were injected in 50 μL PBS solutions to the tumors (4.25 mg SAO/kg for both M-SAO@SiO_2 and SAO@SiO_2nanoparticles). For groups

receiving X-ray irradiation, animals were irradiated by X-rays 5 minutes after the particle injection, at an irradiation dose of 0.5 Gy (over 30 min). Only one therapy dose was applied to each animal. The tumor size and body weight of each animal were measured every other day. The tumor volume was calculated using the formula, tumor volume = length × $(\text{width})^2/2$. Tumors and major organs from the euthanized animals were harvested, weighed, and cryosectioned. The tissue sections were then subjected to standard H&E staining to assess treatment outcomes and side effects (BBC Biochemical).

Biodistribution study.

Normal balb/c mice (Harlan) were injected with M-SAO@SiO_2 nanoparticles (4.25 mg SAO/kg, n = 5). The animals were euthanized 16 days after the injection, and the major organs, such as the liver, kidneys, heart, and spleen, were collected and weighted. The tissues were incubated in hot 70% nitric acid (Sigma Aldrich) until they were decomposed and the solution became clear. The samples were centrifuged to remove remaining debris and the supernatants were analyzed by ICP-MS for strontium concentrations. The strontium contents in the organs were computed and expressed as ng/g tissue.

Statistical analyses

In therapy study, 30 tumor bearing mice were randomly divided into 6 groups. Two investigators were blinded when measuring tumor sizes and assessing treatment outcomes. Quantitative data were expressed as mean ± s.e.m. A two-tailed Student's t-test was used for statistically comparing the treatment group and the control group. $P < 0.05$ was considered statistically significant.

Supplemental Methods

SAO nanoparticle synthesis, surface modification, and photosensitizer loading

SAO was synthesized by a carbo-thermal reduction and vapor-phase deposition method, which was published by us previously.[110, 111] To render SAO amenable to bio-related applications, bulk SAO was ground into particles with diameters of ~ 150 nm. These bare SAO nanoparticles were coated with a layer of solid silica by following a previously published protocol [134]. The resulting nanoparticles were subsequently coated with a layer of mesoporous silica using an established method[75], except that 3-aminopropyltriethoxysilane (5%) (Sigma Aldrich) was mixed with tetraethyl orthosilicate (TEOS) (Sigma Aldrich) as silane precursors.

Characterizations of SAO nanoparticles

UV-Vis absorption spectra were recorded on a Shimdzu 2450 UV-Vis spectrometer. Photoluminescence measurements were performed on a Hitachi F-7000 fluorometer. X-ray excited optical luminescence (XEOL) was measured on Horiba JobinYvon FL3-2iHR fluorescence spectrometer using an emission filter of 285 nm and an emission slit of 3 nm. The recorded spectrum was smoothed by a Savitzky-Golay method of 5 points. A mini-X X-ray tube (Amptek Inc.) was used as the X-ray source, and was set at 50 kV and 70 μA for all the experiments in this study. TEM and HR-TEM samples were prepared by dripping sample solutions onto carbon-coated copper grids and evaporating the solvent. TEM/HR-TEM images were taken on an FEI Tecnai 20 transmission electron microscope operating at 200 kV. SEM images were taken on an FEI Inspect F field emission gun scanning electron microscope at 20 kV. Dynamic light scattering (DLS) analysis was performed using a Zetasizer Nano S90 size analyzer (Malvern Corp, U.K.).

Loading MC540 onto SAO@SiO_2 nanoparticles

For MC540 loading, MC540 (Invitrogen) in ethanol was added to an aqueous solution of SAO@SiO_2 nanoparticles, and the incubation went on overnight at room temperature[107]. The mixture was then centrifuged and the supernatant removed. The collected nanoparticles were resuspended in PBS (Thermo Scientific). The MC540 content in the supernatant was quantified by UV-Vis analysis and compared to a pre-determined standard curve. The yielded MC540 quantity was deducted from the mass of MC540 added at the beginning to arrive at the amount of MC540 that was loaded onto SAO@SiO_2 nanoparticles. The loading efficiency in wt% was computed using Equation 1:

(1)

$$\text{Photosensitizer loading (\%)} = \frac{\text{Mass of photosensitizers incorporated into particles}}{\text{Mass of particles}} \times 100$$

$^1O_2$ production in solutions

1 mL of 0.05 mg M-SAO@SiO_2/mL solution was added into a quartz cuvette (equilibrated with air at room temperature) containing 1 μM of SOSG (Life Technologies). For controls, SAO and MC540 solutions, and water were analyzed. The solutions were irradiated by X-ray at rate of 1 Gy/h for 20 min, with a 1-min intermission after each 5-min irradiation cycle. Fluorescence intensities (ex/em: 504/525 nm) were measured on a Hitachi F-7000 fluorescence spectrophotometer.

Cell imaging

U87-MG cells were incubated with 30 μg/mL of SAO@SiO_2 nanoparticles for 1 h. The cells were washed three times with PBS to remove unbound nanoparticles. The nuclei were

counterstained with DAPI (Vector) and the slide was mounted by a glass cover slip. Images were taken on an Olympus X71 fluorescence microscope (ex/em: 360/460 nm).

To monitor $^1O_2$ generation in live cells, SOSG was added to the incubation medium. Briefly, U87MG cells were seeded in a petri dish and grown for 24 h. The medium was then replenished with fresh medium containing 1 μM SOSG. The incubation went on for 30 min and the cells were washed by PBS to remove excess SOSG. Subsequently, the cells were incubated with M-SAO@SiO_2 nanoparticles (50 μg/mL) for 4 h and then washed with PBS for three times. X-ray irradiation was applied to cells at a dose rate of 1 Gy/h for 30 min. Fluorescence images were acquired on an Olympus X71 fluorescence microscope (ex/em: 504/525 nm).

In vitro X-PDT using pork as model tissue

M-SAO@SiO_2nanoparticles (50μg/mL) were incubated with U87MG cells in petri dishes for 1 h at 37 °C, and the cells were washed with PBS. A stack of pork slices (a total thickness of 4.5 cm) was placed between the X-ray source and the U87MG cells. Cells were exposed to X-ray for 30 min (dose rate of 1 Gy/h), and then cultured for another 24 h. Cell viability was determined by MTT assay. As a comparison, cells treated with X-PDT but without the pork stack were also studied.

Supplemental Figures

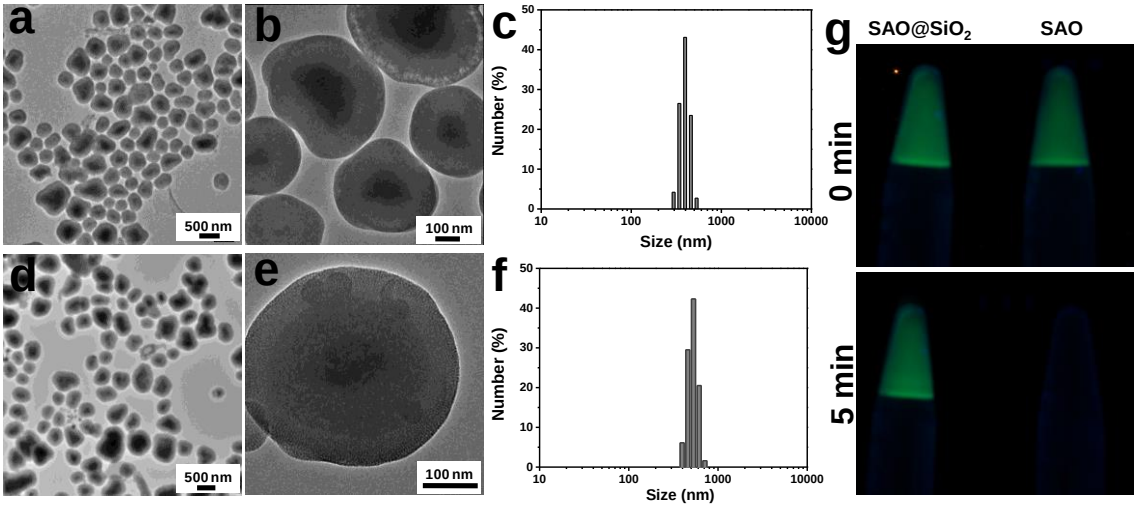

Figure S4.1. Size distribution and stability of silica coated SAO nanoparticles. (a,b) TEM images at relatively low (a) and high (b) magnifications for SAO nanoparticles coated with one layer of solid silica. c, Size distribution of the particles in (a) and (b), analyzed by DLS. (d,e) TEM images at relatively low (d) and high (e) magnifications for SAO nanoparticles coated with two layers of silica (i.e. SAO@SiO_2 nanoparticles). (f) Size distribution of SAO@SiO_2 nanoparticles, analyzed by DLS. (g) Without silica coating, photoluminescence of SAO nanoparticles vanished within 5 min in water.

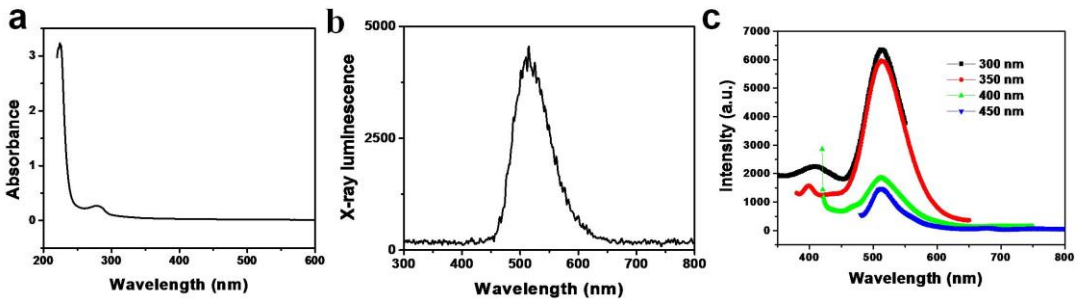

Figure S4.2. Optical properties of as-synthesized SAO. (a) Absorbance spectrum. (b) X-ray excited luminescent spectrum under X-ray excitation. The spectrometer was coupled with a 285-nm emission filter and the emission slit was set at 3 nm. X-ray tube was operated with a tube voltage of 50 KV and a tube current of 70 μA. (c) Photoluminescence spectra of SAO under excitation by light of different wavelengths.

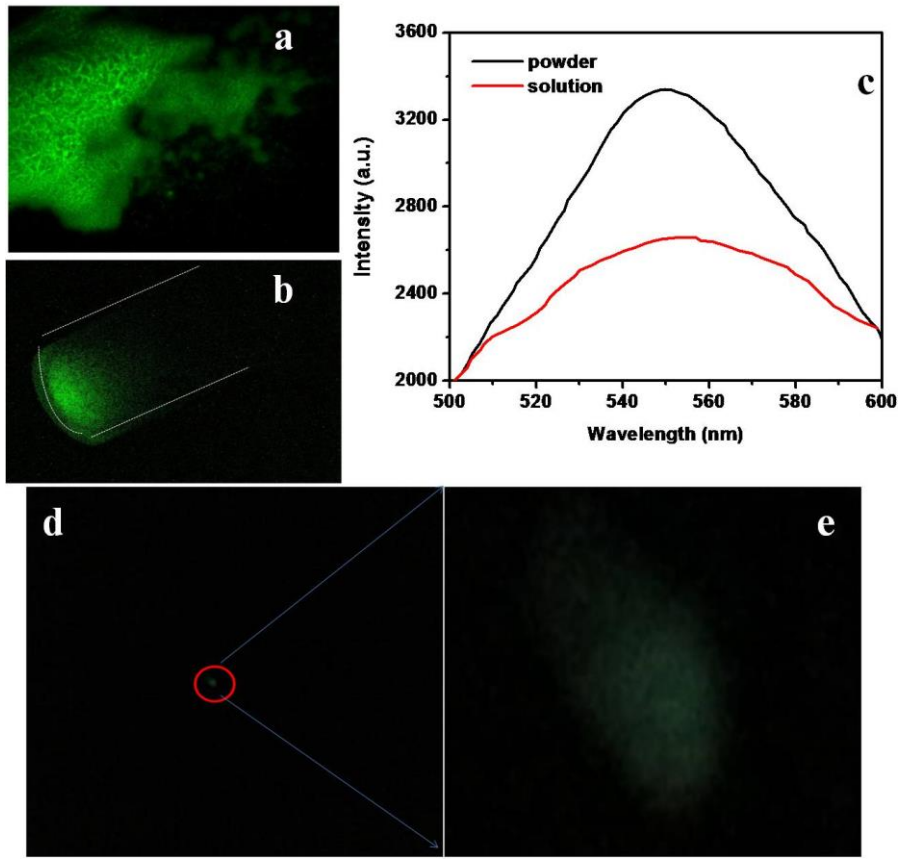

Figure S4.3. X-ray excited optical luminescence of SAO@SiO_2 nanoparticles. (a,b) Photographs of SAO in powder (a) and aqueous solutions (b, 1 mg/mL) under X-ray irradiation in the dark. Images were taken on a Mastro small animal imager. A mini-X X-ray tube was set up in the chamber of the imager as the excitation source. **c,** X-ray excited optical luminescence spectra of (a) and (b), taken by the imager. (d,e) Photographs of M-SAO@SiO_2 nanoparticle powder under X-ray irradiation, taken by an iPhone 4s. X-ray tube was operated with a tube voltage of 50 KV and a tube current of 70 μA.

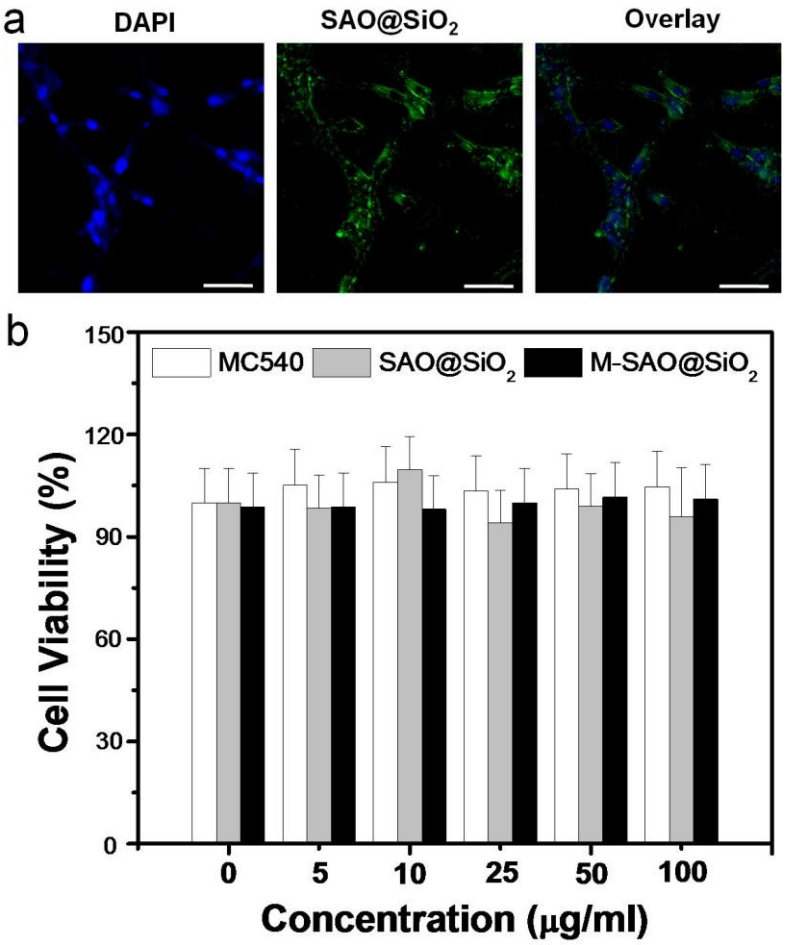

Figure S4.4. (a) Uptake of $SAO@SiO_2$ nanoparticles by U87MG cells (scale bars: 50 μm). Blue, DAPI (ex/em: 360/460 nm). Green, $SAO@SiO_2$ nanoparticles (ex/em: 360/520nm). (b) MTT assay results with MC540, $SAO@SiO_2$, and M-$SAO@SiO_2$ nanoparticles after 24 h incubation. The error bars represent ± s.e.m. (n = 5 per group).

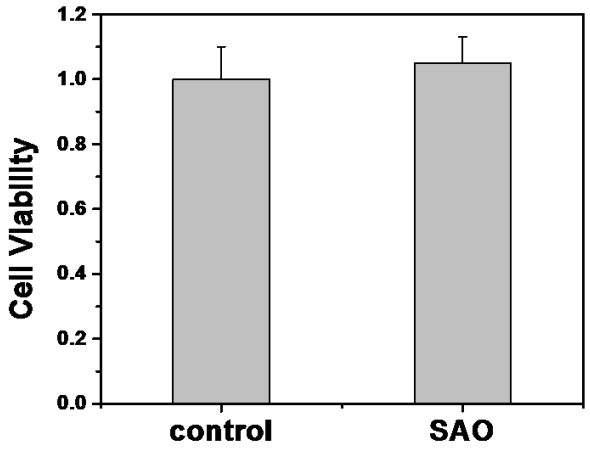

Figure S4.5. MTT assay results, studied using hydrolytes of bare SAO nanoparticles (0.05 mg/mL). No sign of cytotoxicity was observed. The error bars represent ± s.e.m. (n=5 per group).

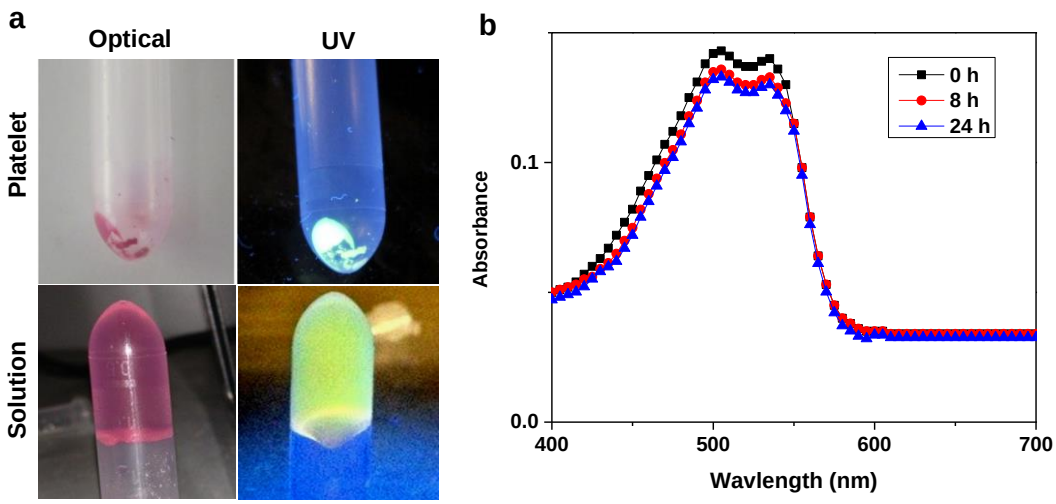

Figure S4.6. (a) Photographs of M-SAO@SiO_2 in powder (upper panel) and solution (lower panel) when irradiated in the dark by 365-nm UV light. (b) Release of MC540 from M-SAO@SiO_2, investigated by analyzing the change of absorbance over time. Compared to the initial time point (0 h), the release of MC540 at 8 h and 24 h is minimal.

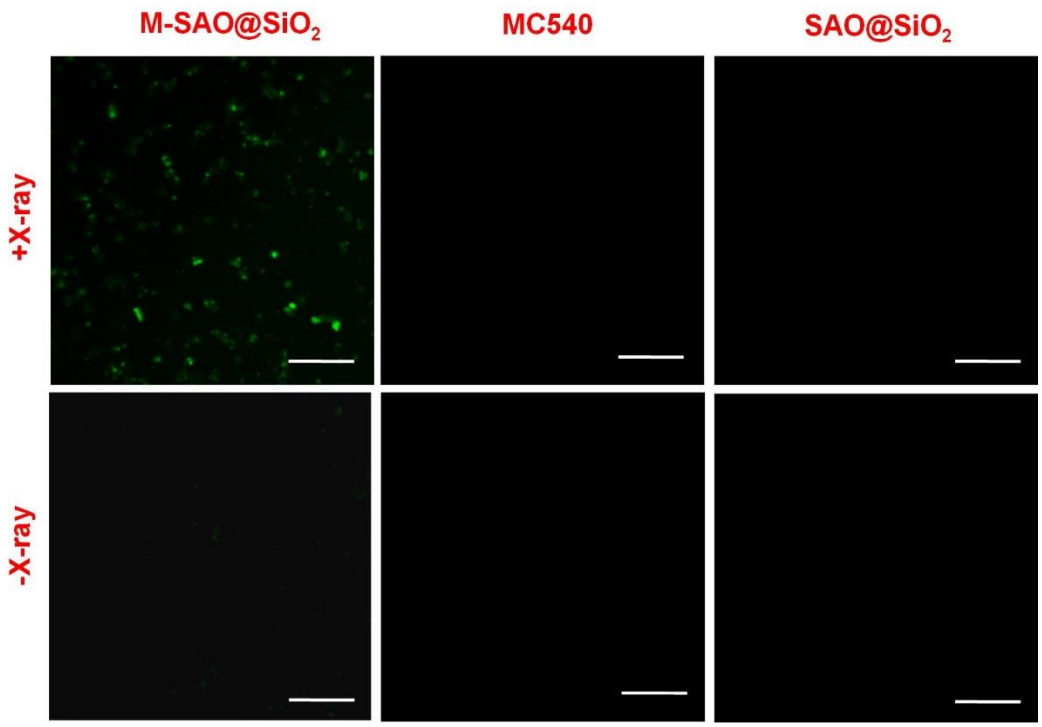

Figure S4.7. $^1O_2$ production in cells. U87MG cells were incubated with M-SAO@SiO_2 nanoparticles, SAO@SiO_2 nanoparticles, or MC540, with and without subsequent X-ray irradiation. X-ray tube was operated with a tube voltage of 50 KV and a tube current of 70 µA. SOSG was used as a $^1O_2$ indicator. Enhanced fluorescence (ex/em:504/525 nm) was only observed with cells treated with a combination of M-SAO@SiO_2 nanoparticles and X-rays. Scale bars, 100 µm.

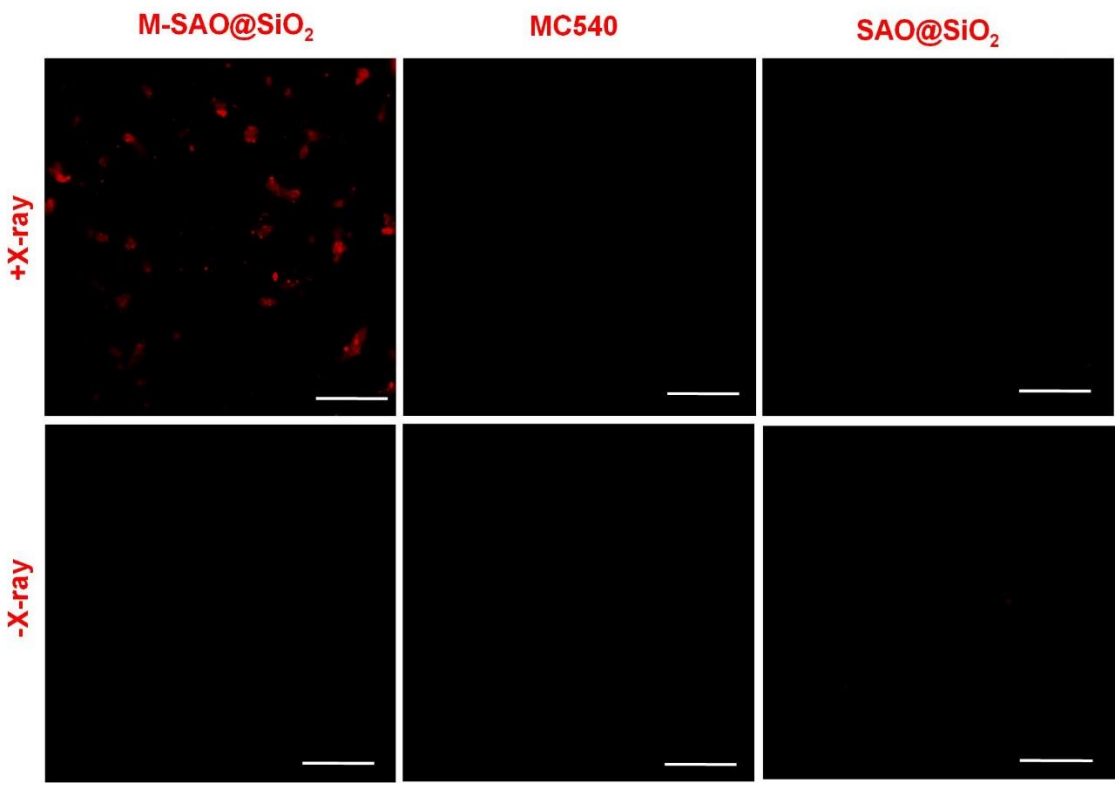

Figure S4.8. Cytotoxicity induced by X-PDT, studied by ethidium homodimer-1 assay. M-SAO@SiO_2 nanoparticles (0.05 mg/mL) were incubated with U87MG cells for 1 h before X-ray irradiation. X-ray tube was operated with a tube voltage of 50 KV and a tube current of 70 µA. Consistent with the observations made in **Figure S7**, toxicity was only found with cells treated with the M-SAO@SiO_2 nanoparticle and X-ray combination. Ex/em: 517/617 nm. Scale bars, 100 µm.

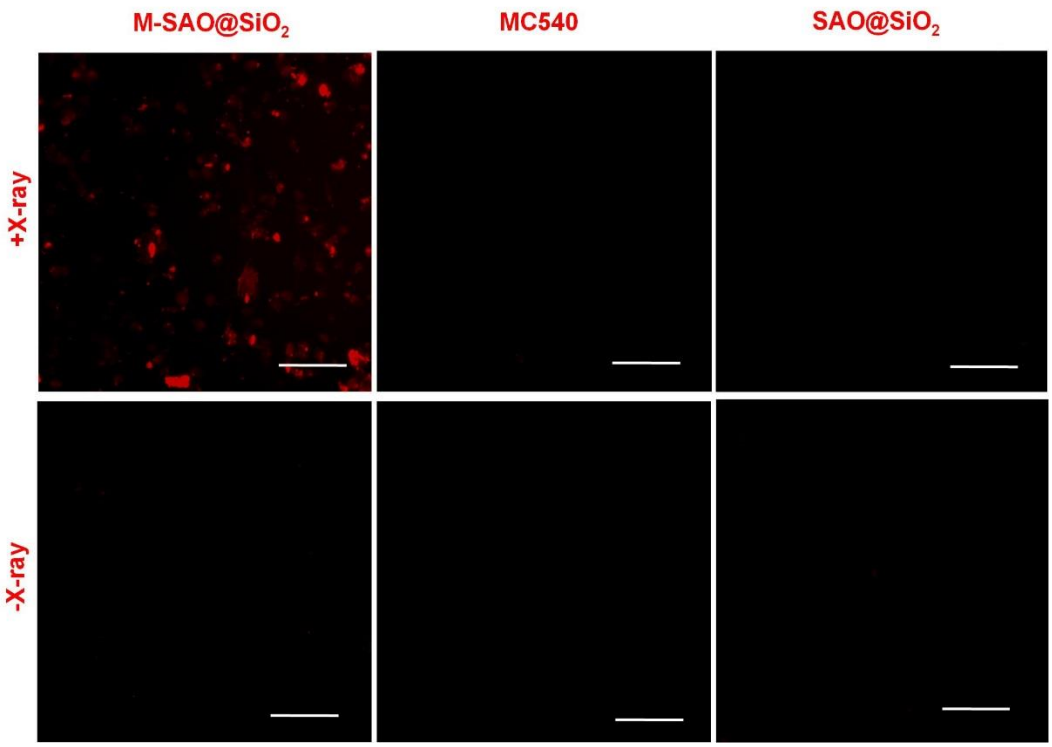

Figure S4.9. Cytotoxicity induced by X-PDT, studied by ethidium homodimer-1 assay. X-ray tube was operated with a tube voltage of 50 KV and a tube current of 70 μA. M-SAO@SiO_2 nanoparticles (0.05 mg/mL) were incubated with U87MG cells for 24 h before X-ray irradiation. Ex/em: 517/617 nm. Scale bars, 100 μm.

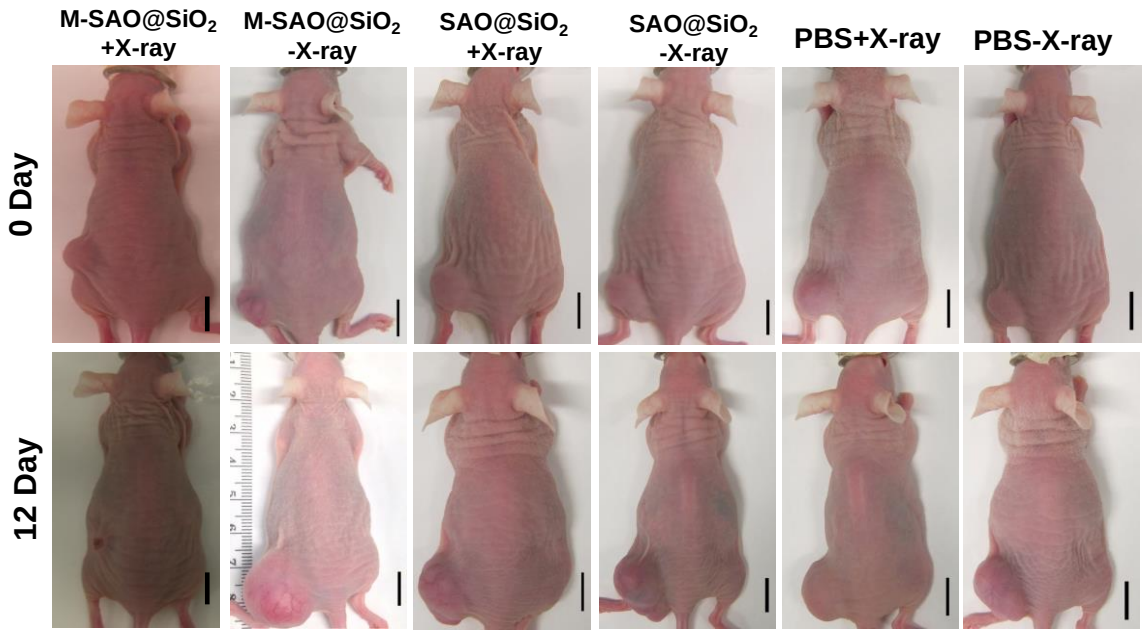

Figure S4.10. Representative photographs of mice from Groups 1-6 on day 12 (scale bar: 1 cm).

Figure S4.11. Photographs of tumors taken from Groups 1 (i.e. therapy group).

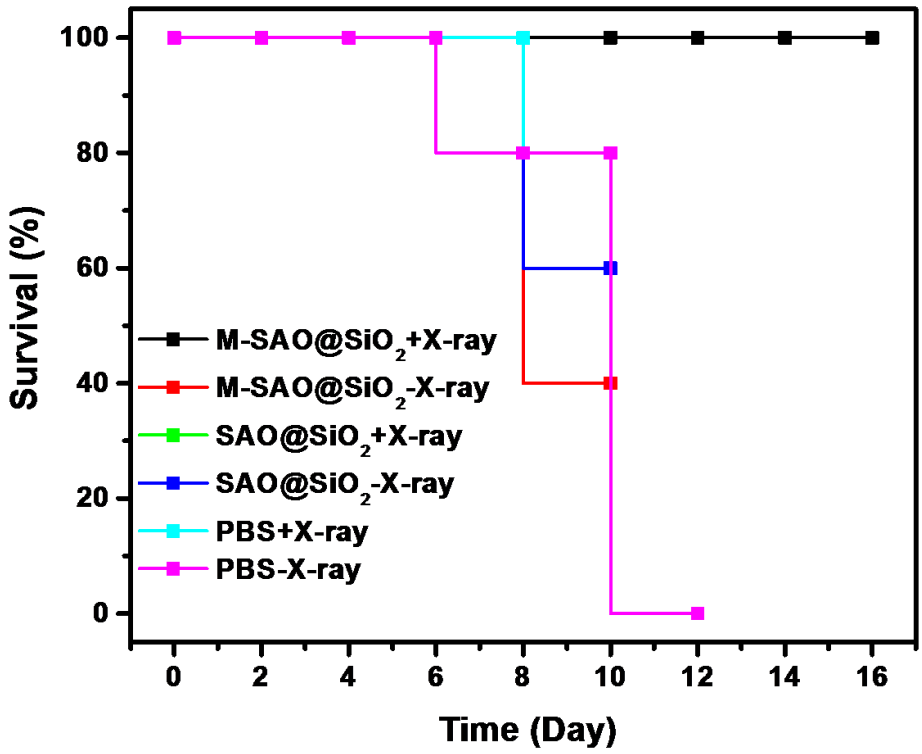

Figure S4.12. Survival curves for animals from Groups 1-6.

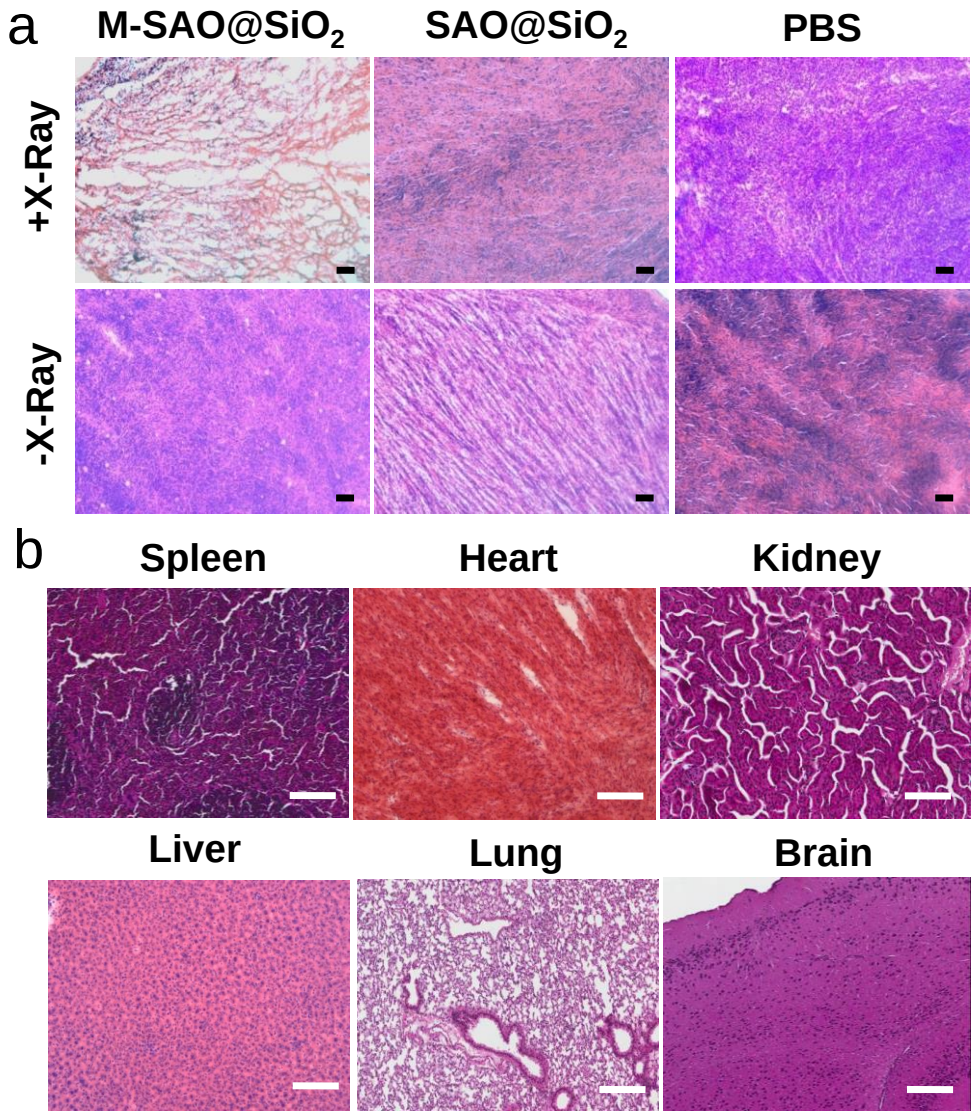

Figure S4.13. H&E staining results. (a) H&E staining with tumor tissues from different treatment groups. Scale bars, 100 μm. (b) H&E staining with normal tissues taken from Group 1. Scale bars, 100 μm.

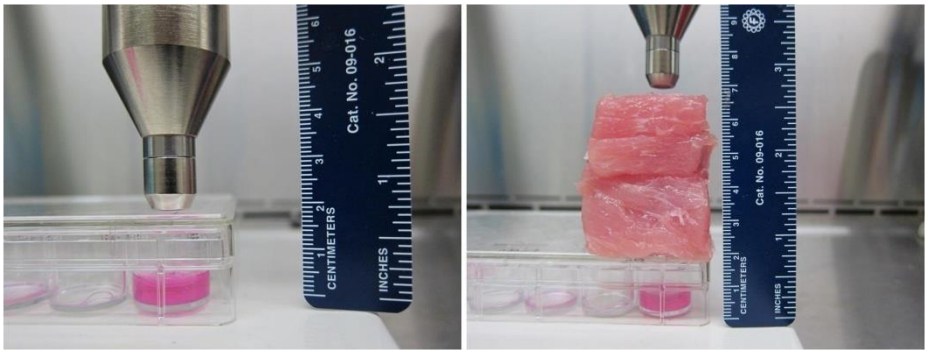

Figure S4.14. Photographs showing the experimental setup for assessing *in vitro* toxicity induced by X-PDT without (left) and with (right) pork as an X-ray blocker. X-ray tube was operated with a tube voltage of 50 KV and a tube current of 70 μA.

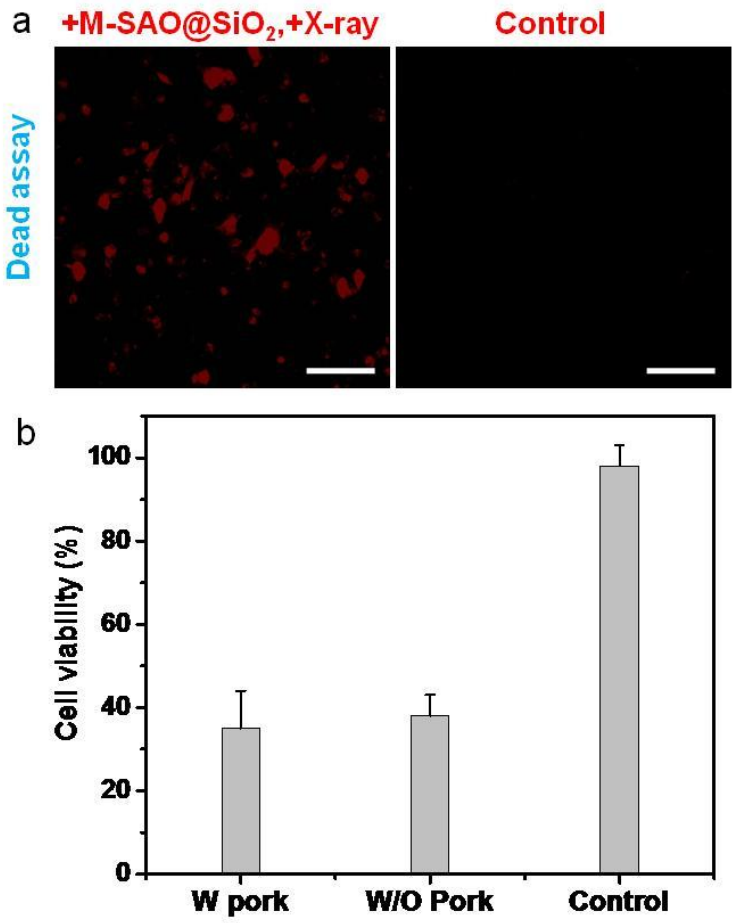

Figure S4.15. *In vitro* cytotoxicity study with X-PDT, with 4.5-cm pork blocked between the X-ray source and the cells. (a) Ethidium homodimer-1 assay results. Despite of the thick pork as a blocker, X-rays can effectively activate X-PDT to cause cell death, manifested by enhanced red fluorescence (ex/em: 517/617 nm). Scale bar: 100 μm. (b) Comparison of cytotoxicity, with and without the use of pork as an X-ray blocker. X-ray tube was operated with a tube voltage of 50 KV and a tube current of 70 μA. The error bars represent ± s.e.m. (n = 4 per group).

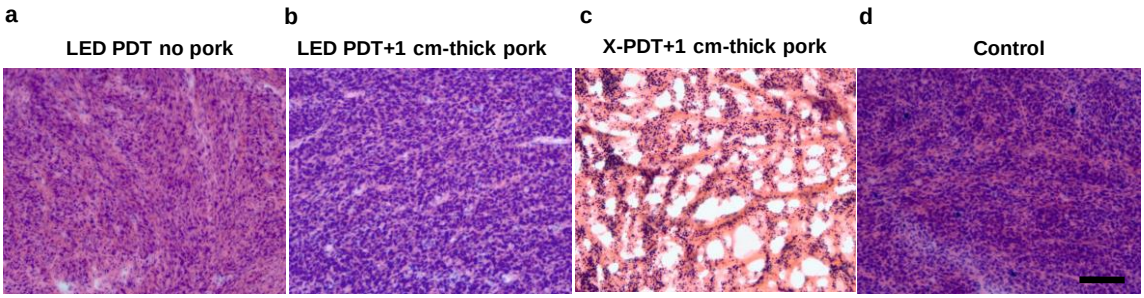

Figure S4.16. H&E staining results. (a) UG87 tumor xenografts were intratumorally injected with M-SAO@SiO_2 nanoparticles (6.25 mg/kg) and irradiated by 520 nm LED light (0.1 W/cm^2) for 30 min. The tumors were excised 14 days after the treatment. (b) A 1-cm-thick pork slice was laid on top of the tumors during the irradiation; otherwise the conditions were the same as those in **a**. No detectable damage was observed for animals from (a) and (b). (c) Animals were injected with M-SAO@SiO_2 nanoparticles but were irradiated by X-ray (1 Gy/h for 30 min); similar to b, a 1-cm-thick pork was laid between the X-ray tube and the tumors. There was a significant decrease in cancer cell density. (d) Animals were injected with PBS and received no irradiation. Scale bar: 100 μm.

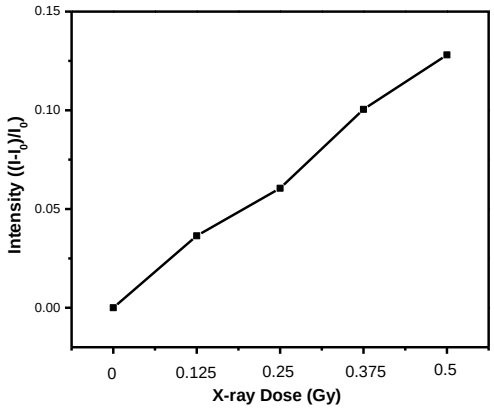

Figure S4.17. An elevated X-ray dose corresponds with an increased $^1O_2$ production, performed with a 6.25 mg/mL M-SAO@SiO_2 solution. X-ray was operated at 1 Gy/h, 50 kV.

CHAPTER 5

X-RAY INDUCED PHOTODYNAMIC THERAPY: A COMBINATION OF RADIOTHERAPY AND PHOTODYNAMIC THERAPY [4]

[4] Geoffrey D. Wang, Ha T. Nguyen, Hongmin Chen, et al. 2016. Theranostics. 6(13):2295-2305. Reprinted here with permission of the publisher.

Abstract

Conventional photodynamic therapy (PDT)'s clinical application is limited by depth of penetration by light. To address the issue, we have recently developed X-ray induced photodynamic therapy (X-PDT) which utilizes X-ray as an energy source to activate a PDT process. In addition to breaking the shallow tissue penetration dogma, our studies found more efficient tumor cell killing with X-PDT than with radiotherapy (RT) alone. The mechanisms behind the cytotoxicity, however, have not been elucidated. In the present study, we investigate the mechanisms of action of X-PDT on cancer cells. Our results demonstrate that X-PDT is more than just a PDT derivative but is essentially a PDT and RT combination. The two modalities target different cellular components (cell membrane and DNA, respectively), leading to enhanced therapy effects. As a result, X-PDT not only reduces short-term viability of cancer cells but also their clonogenecity in the long-run. From this perspective, X-PDT can also be viewed as a unique radiosensitizing method, and as such it affords clear advantages over RT in tumor therapy, especially for radioresistant cells. This is demonstrated not only in vitro but also in vivo with H1299 tumors that were either subcutaneously inoculated or implanted into the lung of mice. These findings and advances are of great importance to the developments of X-PDT as a novel treatment modality against cancer.

Keywords: photodynamic therapy, radiotherapy, lung cancer, clonogenecity, nanoparticles

Introduction

PDT is a relatively new and minimally invasive cancer therapy approach [135-137]. PDT utilizes photosensitizers that are activated by light in the presence of oxygen, producing reactive oxygen species (ROS) that are cytotoxic [137]. PDT can kill cancer cells directly and or damage tumor microvessels, leading to tissue ischemia [136, 138, 139]. It has been utilized in the clinic

for treatments of different cancer types, including esophageal cancer, non-small cell lung cancer, bladder cancer, and head and neck cancer [140-144]. Despite of the promises, however, PDT suffers from the shallow tissue penetration of light, especially in the visible spectrum window [145]. There has been progress of developing near-infrared (NIR) photosensitizers, for instance Lumin, Motexafin lutetium, and TOOKAD (absorption peaks at 770 nm, 732 nm and 753 nm) [146, 147]. However, even in the NIR region, light can travel less than 1 cm in tissues. This restriction has largely limited the applications of PDT in the clinic.

Recently, we and others have developed a new PDT derivative called X-ray induced PDT, or X-PDT [87, 148-150]. The goal is to break the shallow penetration restriction by using X-ray as an energy source [151]. The idea of utilizing X-ray to overcome the shallow penetration of PDT was first raised by Chen et al. in 2006 [152], but it was not until very recently that we and the Chen group demonstrated its feasibility in vivo [87, 148-150]. In particular, we showed in a recent study that $SrAl_2O_4:Eu^{2+}$ nanoparticle (SAO:Eu, a scintillator which convert X-ray photons to visible photons) and MC540 (a photosensitizer with matching excitation wavelength) co-loaded mesoporous silica nanoparticles (MC540-SAO:Eu@$mSiO_2$) can produce singlet oxygen ($^1O_2$) under X-ray radiation, leading to efficient cancer cell death, even when the cells are beneath thick tissues [87].

It is clear that during X-PDT, not all X-ray energy, but a portion of it, is converted to visible photons to activate PDT. Despite of the studies by us and others observed enhanced treatment efficacy with X-PDT relative to radiation therapy (RT) alone at the same radiation doses [87, 148-150], this phenomenon is intriguing, indicating that there is more to X-PDT than a mere PDT process. In the current study, we tap into the mechanisms behind X-PDT-induced cell death. Specifically, we conducted comprehensive studies to examine the impacts of X-PDT

on cell viability, clonogenicity, apoptosis, necrosis, DNA damage, and membrane lipid damage. Our studies showed that X-PDT contains a RT component, and hence it is essentially a RT and PDT combination. The two modalities interplay to attack both cell membrane and DNA, leading to lethal damage that is beyond the repairs of cells. The synergy explains the better cell killing efficacy of X-PDT than RT, even for cells that are refractory to radiotherapy. In particular, we found that X-PDT can efficiently kill H1299 cells, which are radioresistant non-small cell lung cancer (NSCLC) cells. The enhanced efficacy was observed not only in vitro but also in vivo with a subcutaneous tumor model or when H1299 cells were percutaneously implanted into the lung. These findings are of great value to our understanding of X-PDT as a novel treatment modality and its further transformation for eventual clinical translation.

Experiments and Results

Preparation of MC540-SAO:Eu@mSiO_2 nanoparticles

The MC540-SAO:Eu@mSiO_2 nanoparticles were prepared by following our published protocol [87]. Briefly, $SrCO_3$, Al_2O_3, Eu_2O_3 and graphite powders were mixed and heated in a tube furnace at 1450 °C for 2 h under an argon flow. The pressure was maintained at 5 Torr. The as-synthesized bulk SAO:Eu was subject to mechanical grinding, followed by sedimentation, filtration and centrifugation, to yield nanoscale nanoparticles (73.5 ± 26.9 nm, **Figure 5.1a,b**). X-ray diffraction (XRD) analysis found that the composition of the material was monoclinic $SrAl_2O_4$ (JCPDS #74-0794, **Figure S5.1**). Inductively coupled plasma (ICP) confirmed the chemical composition and found that Eu accounts for ~1% of the total mass. As described in the previous study, $SrAl_2O_4$:Eu can be stimulated by both Uv-vis and X-ray to emit green photoluminescence (centered at ~520 nm, **Figure 5.1c**), which is attributed to $4f^6 5d^1 \rightarrow 4f^7$ transition of Eu^{2+} ions [15].

$SrAl_2O_4$:Eu is a highly hydrolytic material and is quickly reduced to constituent ions in an aqueous solution [15]. For bio-applications, we coated $SrAl_2O_4$:Eu nanoparticles with two layers of silica (**Figure 5.1b**). These include an inner, solid silica layer that prevents direct

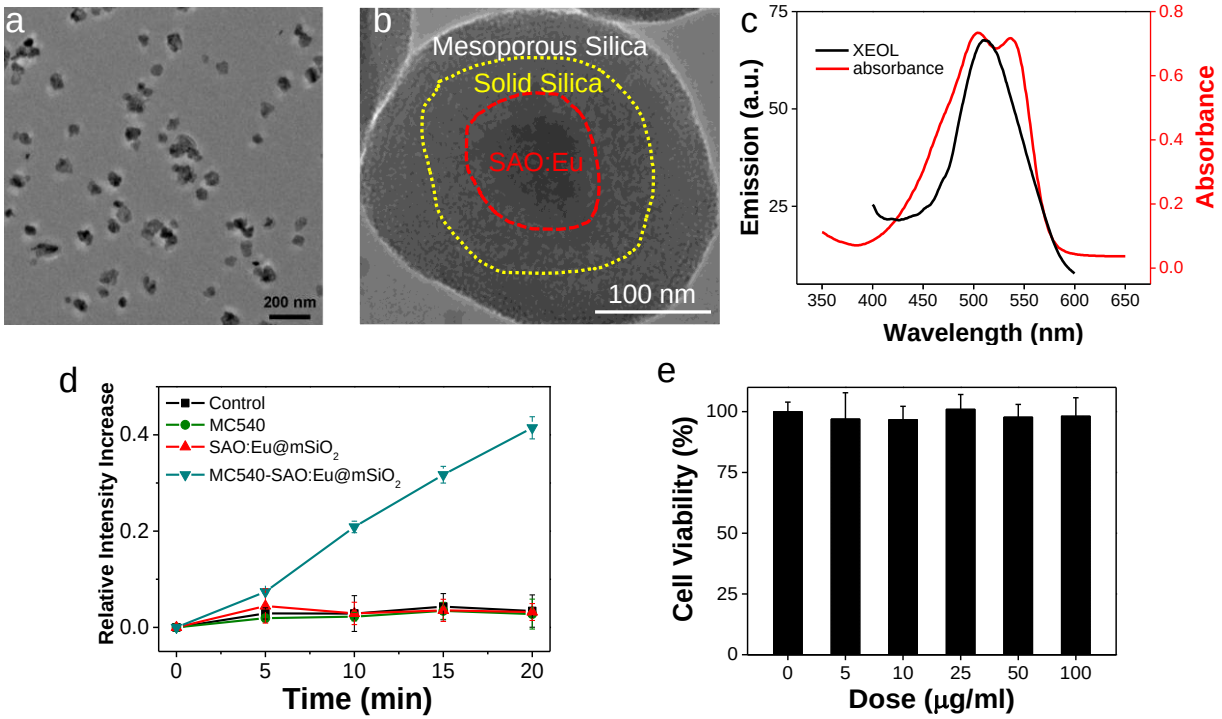

Figure 5.1. Characterizations of SAO:Eu@$mSiO_2$ nanoparticles. (a) TEM image of SAO:Eu nanoparticles. (b) TEM image of a representative SAO:Eu@$mSiO_2$ nanoparticle. (c) XEOL spectrum of SAO:Eu@$mSiO_2$ nanoparticles and the absorption spectrum of MC540. The excitation wavelength of photosensitizers and the emission wavelength of SAO:Eu match well. (d) Singlet oxygen generation under X-ray irradiation. (e) Cytotoxicity of SAO:Eu@$mSiO_2$ nanoparticles. Little toxicity was observed even at high nanoparticle concentrations.

contact with the aqueous surroundings, and an outer, mesoporous silica layer that provides a docking place for photosensitizers [87]. Into the resulting $SrAl_2O_4$:Eu@$mSiO_2$ nanoparticles, MC540 (**Figure S5.2**), a common photosensitizer that has been investigated in both pre-clinical

and clinical studies [153], was loaded. The absorbance wavelengths of MC540 well match the emission wavelengths of SAO:Eu (**Figure 5.1c, S5.3**). Using singlet oxygen sensor green (SOSG) assays, we studied the ability of X-PDT to producing $^1O_2$. It was found that X-ray alone (1-4 Gy) was not able to produce $^1O_2$, either with PBS, MC540, or $SrAl_2O_4$:Eu nanoparticles (Figure 1d). As a comparison, when both $SrAl_2O_4$:Eu@$mSiO_2$ (0.05 mg/mL) and X-ray were applied, efficient $^1O_2$ production was observed (**Figure 5.1d**).

Impact of X-PDT on cell viability and clonogenecity

We first investigated the impact of X-PDT on cell viability by MTT assays. Radioresistant NSCLC H1299 cells were used in the studies [154-156]. In the absence of radiation, SAO:Eu and SAO:Eu@$mSiO_2$ nanoparticles were not toxic to H1299 cells (**Figure 5.1e and 5.2a**). The low toxicity of SAO:Eu@$mSiO_2$ was also observed in our previous studies with other cell lines [157] and is not surprising because all the constituents of the nanoparticles, including MC540, SAO:Eu, and SiO_2, are not toxic in the dark [87]. Meanwhile, RT alone (0-5 Gy) did not induce significant cell death at 24 hours either (**Figure 5.2a**). As a comparison, when X-ray irradiation was applied after MC540-SAO:Eu@$mSiO_2$ (50 μg/mL) incubation (i.e. X-PDT), there was significant cell viability drop (**Figure 5.2a**). Specifically, when irradiation of 0.83, 1.67, 3.33, and 5 Gy was applied, the 24-hour cell viability was reduced to 31.4 ± 2.3%, 19.6 ± 4.6%, 18.6 ± 7.4%, and 17.5 ± 5.6%, respectively.

While MTT assay is adequate to measures short-term cell viability, it is suboptimal in assessing the reproductive capacity of cancer cells. For RT, however, reproductive capacity is a more relevant ending point. This is because ionizing radiation mainly targets DNA, most importantly double-strand DNA break [158]. This is often manifested not as immediate cell death but reduced clonogenicity in days or weeks [159]. To investigate, we performed

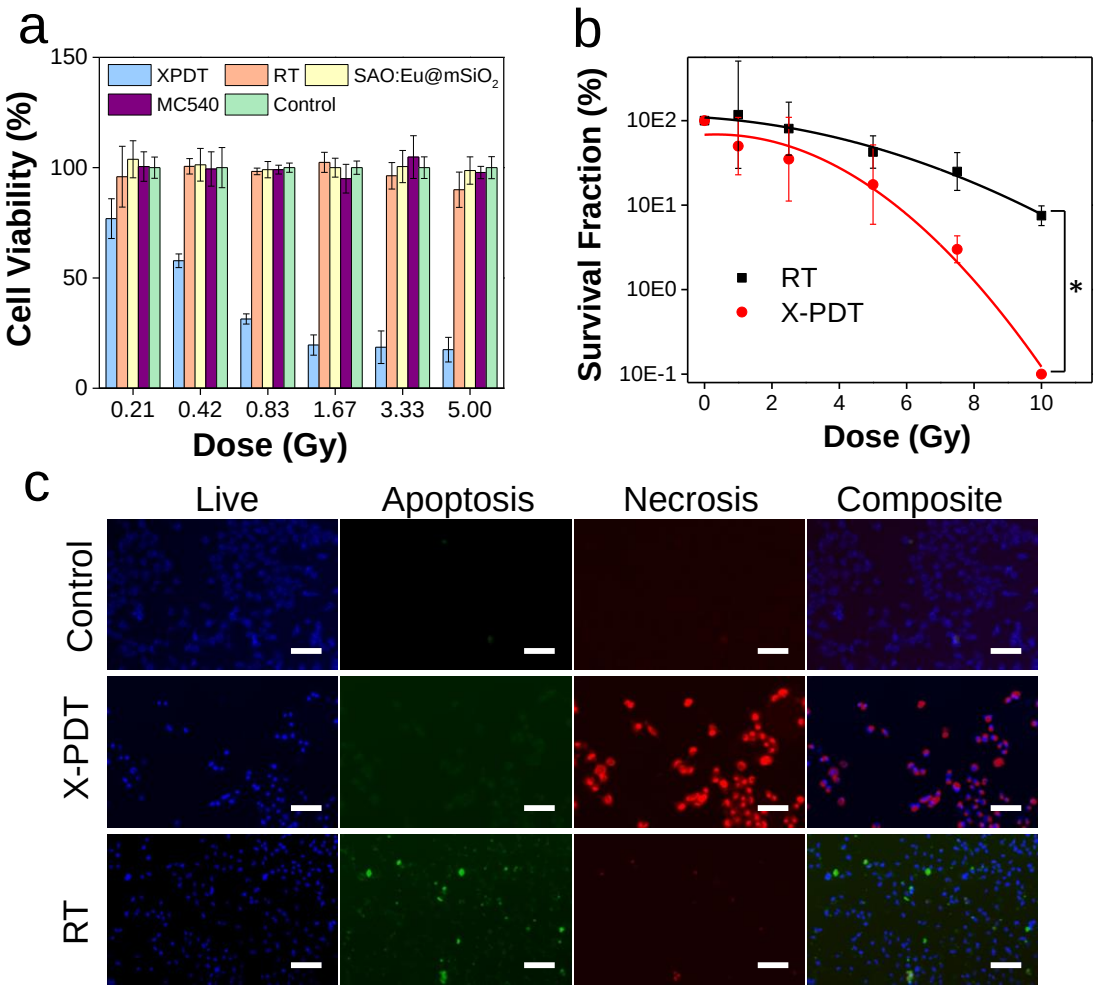

Figure 5.2. X-PDT induced cell death. (a) Cell viability, measured by MTT assays performed 24 h after X-PDT. In control groups, including RT alone and nanoparticles alone, there was no significant drop of viability. (b) Cell reproductive capacity, measured by clonogenic assays taken 14 days after X-PDT (* p-value < 0.01). (c) Apoptosis and necrosis assays, performed 24 h after X-PDT. Scale bars: 100 µm.

clonogenic assays with H1299 cells that received RT alone (0, 1, 2.5, 5, 7.5 and 10 Gy) or RT plus MC540-SAO:Eu@mSiO$_2$ (50 µg/mL). X-PDT was much more effective than RT alone at all doses (**Figure 5.2b**). Taking 5 Gy for instance, X-PDT was able to reduce the survival fraction

(SF) to 17.5%, compared to that of 42.5% for RT alone. The dose enhancement factor (DEF) was calculated to be 1.67 (Methods Section).

Impact of X-PDT on DNA and lipid membranes

To further investigate the cause of X-PDT induced cell death, we performed Apoptotic/Necrotic/Healthy assay (PromoCell, Heidelberg, Germany), again with H1299 cells. With RT only (5 Gy), cells showed a mediocre level of apoptosis at 24 h but no detectable necrosis (**Figure 5.2c**). On the contrary, when cells were treated with MC540-SAO:Eu@mSiO_2 (50 μg/mL) plus radiation, there manifests extensive cell necrosis (**Figure 5.2c**). This pattern resembles membrane-targeted PDT, which causes oxidative degradation of unsaturated lipids and surface proteins [160]. To confirm, we conducted lipid peroxidation assay (Lipid Peroxidation Kit, Life Technologies, Carlsbad, CA). Compared to the control (PBS only), the lipid peroxidation level was increased by 90.5 ± 23.0% after RT (5 Gy); meanwhile, X-PDT under the same irradiation dose led to an increase of 201.5 ± 34.0% (**Figure 5.3a**). Such lipid peroxidation is attributed mainly to the PDT component of X-PDT and is responsible for the short-term cell necrosis and viability drop.

Meanwhile, X-PDT also causes DNA damage. This was confirmed by comet assays in (also known as single cell gel electrophoresis assay, **Figure 5.3b**). Compared to the control, cells eceived RT alone (5 Gy) displayed a relatively long and intense tail, suggesting extensive DNA double-strand break [161]. Such a tail was also observed with X-PDT treated cells, but was shorter, less intense, and more discrete, likely associated with the extensive necrosis [161]. This suggests that there remains a RT component in X-PDT, which explains the reduced cell survival in clonogenic assays.

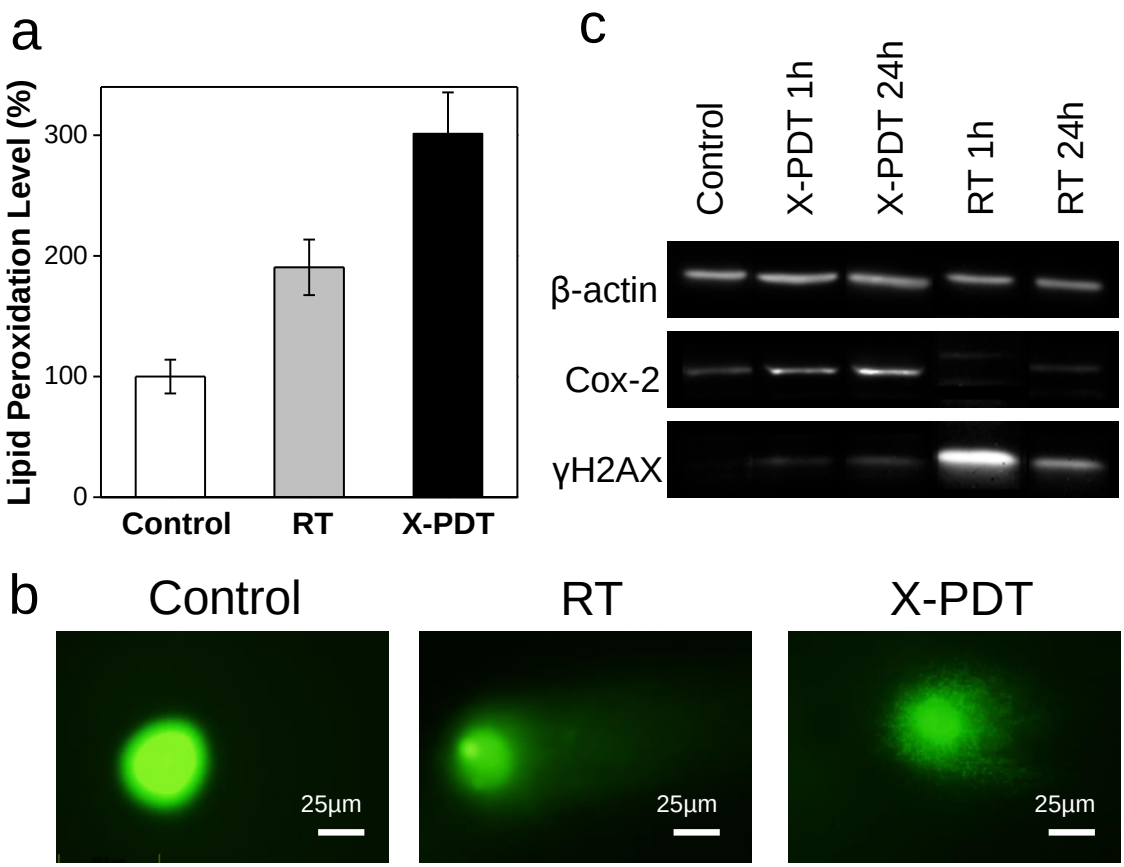

Figure 5.3. Impacts of X-PDT on cellular compartments. (a) Lipid damage assessment, measured by lipid peroxidation assays. (b) DNA damage, assessed by single cell electrophoresis assays. (c) Western blot assays, which further confirms the impact of X-PDT on DNA and membrane lipids.

To further assess the cellular impacts of X-PDT, we analyzed expression levels of histone H2AX and Cox-2 in X-PDT treated H1299 cells with Western blot (**Figure 5.3c**). Histone H2AX plays a critical role in recruiting repair- or damage-signaling factors to the sites of DNA damage [162, 163] and is thus an indicator of RT-induced DNA breakage. Cox-2, on the other hand, is involved in lipid peroxidation, and is often up-regulated after PDT-induced membrane damage [164, 165]. We found that X-ray radiation (5 Gy) alone induced expression of H2AX but minimally affected the level of Cox-2 (**Figure 5.3c**). With X-PDT, on the other hand, both Cox-2

and H2AX expressions were increased, although the H2AX level was lower than that after RT (**Figure 5.3c**). These results corroborate with the preceding studies, again confirming that X-PDT is essentially a combination of RT and PDT. It is postulated that because the two modalities target different cellular compartments (DNA and unsaturated membrane lipids, respectively), a synergy in treatment occurs that leads to much more efficient cancer cell killing.

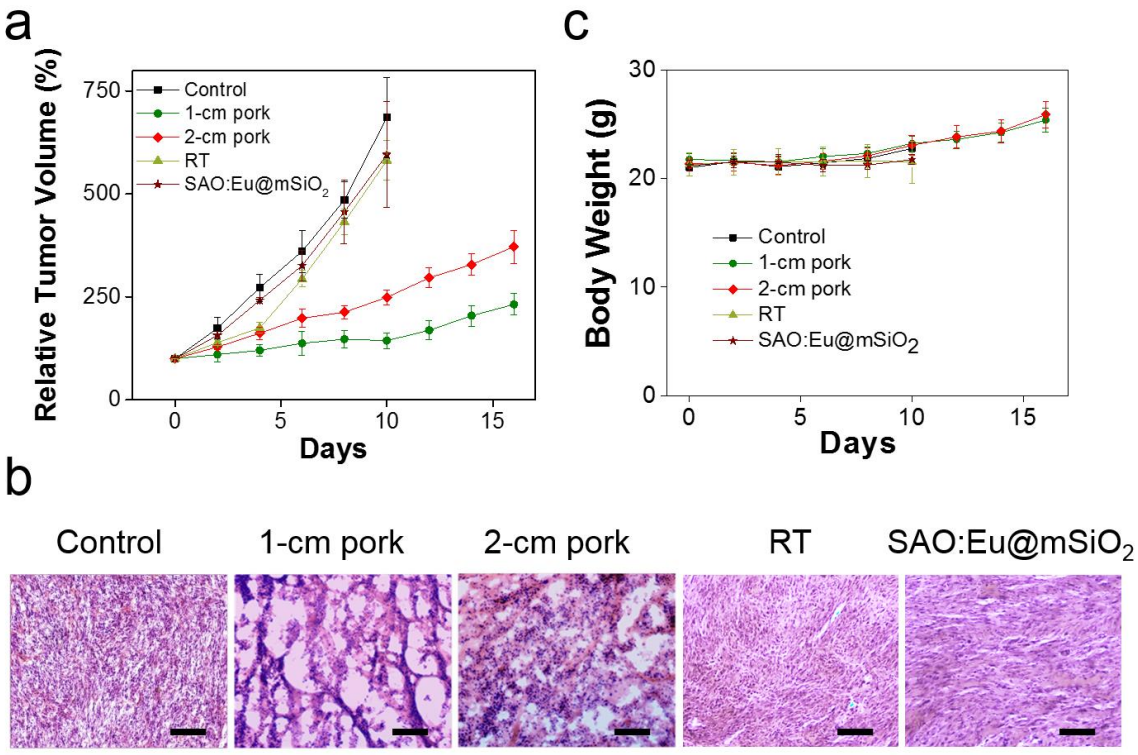

Figure 5.4. X-PDT to treat subcutaneously implanted tumors from above thick tissues. (a) Tumor growth curves. Despite of using thick pork as tissue blocks, X-PDT can efficiently suppress tumor growth. (b) H&E staining with tumor tissues. X-PDT caused extensive cancer cell death in H1299 tumors. Scale bars, 100 μm. (c) Body weight curves. X-PDT did not cause significant changes to the animal body weights.

Impact of tissue depth on the efficacy of X-PDT

We next studied the impact of tissue thickness on the treatment efficacy of X-PDT in vivo. This was first studied with mouse subcutaneous tumor models established with H1299 cells.

Briefly, we intratumorally injected MC540-SAO:Eu@$mSiO_2$ nanoparticles (4.25 mg/kg) to tumor bearing animals; we then irradiated the tumors (5 Gy, with the rest of the body lead-shielded), with pork tissues of 1- or 2-cm thickness lain on top. In control group, animals were injected with PBS and received no radiation.

Tumors in the control group grew very rapidly, and either died or reached an end point (tumor diameter > 1.7 cm) within 10 days (**Figure 5.4a**). As a comparison, in all the treatment groups, tumor growth was efficiently slowed. On Day 16, the tumor suppression rates were 54.2% and 33.8%, for the animals bore with 1-, and 2-cm thick pork, respectively. The results suggest that tissue thickness can still affect the efficacy of X-PDT; the impact, however, was much less severe than with PDT, which lost its efficacy beyond 1 cm thickness. Such tissue impact can likely be compensated by increasing radiation doses and is less of a concern in the clinical setting, where deep-penetrating megavoltage X-rays are used [166]. The efficiency in cancer cell killing was further confirmed with H&E analysis (**Figure 5.4b**). Compared with the control animals, where cancer cells were densely packed, X-PDT dramatically reduced cell density and disrupted connective tissues (**Figure 5.4b**). Meanwhile, we observed no signs of systematic toxicities to the surrounding tissues (**Figure 5.4c**).

Next, we investigated the X-PDT efficacy by injecting nanoparticles and cell mixture to the thorax of mice and irradiated the injection sites in vivo. Due to thick soft tissues and bones, diseases at this position are not accessible by conventional PDT [167]. Specifically, we injected MC540-SAO:Eu@$mSiO_2$ nanoparticles (4.25 mg/kg), along with 5×10^5 firefly luciferase expressing H1299 cells (H1299-Luc), into the left lateral thorax of nude mice (**Figure 5.5a**). Radiation (5 Gy) was applied to the tumor inoculation sites, with the rest of the animal body shielded by lead. Control group animals received radiation only or PBS only. The tumor growth

was then monitored in vivo by bioluminescence imaging (BLI). In PBS and RT only groups, the

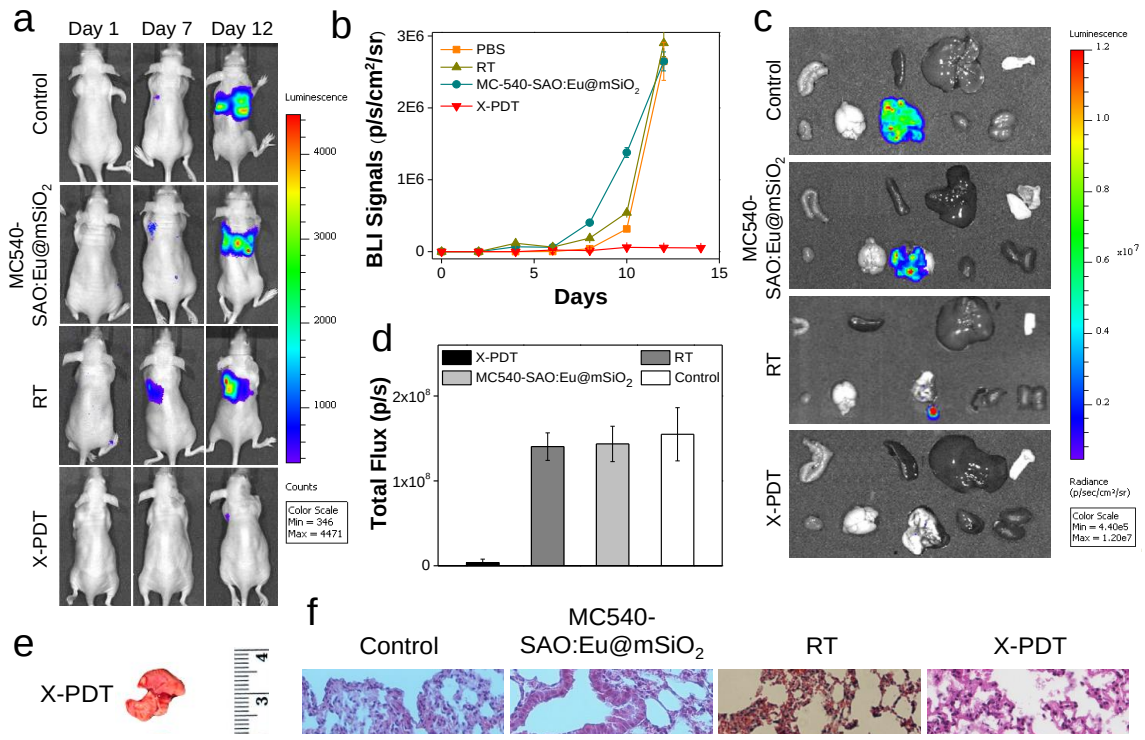

Figure 5.5. In vivo therapy studies. (a) Representative bioluminescence images of mice treated by X-PDT, RT, MC540-SAO:Eu@$mSiO_2$ and PBS on Day 1, 7, and 12. MC540-SAO:Eu@$mSiO_2$ nanoparticles were intrathoracically injected to the mice. In the RT and X-PDT groups, a single dose X-ray radiation of 5 Gy was applied to the tumor area, with the rest of the body covered by lead. (b) Tumor growth, measured by monitoring BLI signal changes at different time points. (c) Ex vivo bioluminescence images taken immediately after tissue dissection. The organs were organized in the following order: top row (from left to right): intestine, spleen, liver and skin; bottom row (from left to right): muscle; brain; lung; heart and kidneys. (d) BLI signals from the lungs. Based on ROI analyses on (c). (e) Representative photographs of lungs taken from the X-PDT and control Groups. (f) H&E staining with tumor tissues from different treatment groups. Scale bars, 100 μm.

BLI signals were detected in the lung areas on Day 7 and continued increasing afterwards (**Figure 5.5a**). In X-PDT treated animals, on the other hand, the BLI signals were significantly suppressed. By regions of interest (ROI) analysis, on Day 12, the average BLI signals were 5.6×10^5, 2.9×10^6, and 2.6×10^6 photons/sec/cm^2/sr for the X-PDT, RT, and PBS groups, respectively (**Figure 5.5b**). Ex vivo imaging confirmed the efficiency of X-PDT induced tumor suppression, finding strong residual signals in the lungs of control animals but close-to-background signals from the X-PDT group (**Figure 5.5c, d**). Moreover, we found multiple large tumors in the lungs dissected from control animals, but few detectable colonies in X-PDT treated mice (**Figure 5.5e**). Such reduced tumorigenicy by X-PDT was further confirmed by H&E staining (**Figure 5.5f**).

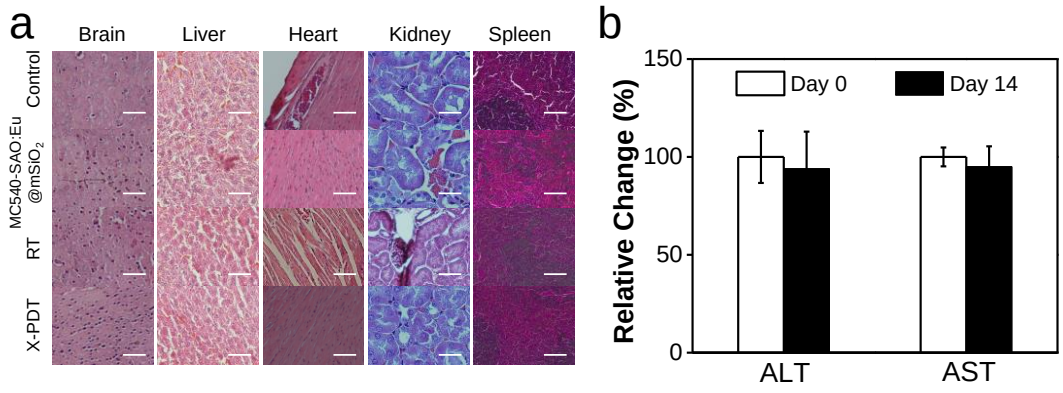

Figure 5.6. Systematic toxicities of X-PDT. (a) H&E staining with normal tissues taken from X-PDT, RT, MC540-SAO:Eu@mSiO$_2$, and control groups. Scale bars, 100 μm. (b) Hemodiagnosis. ALT and AST level showed no significant changes before and 14 days after X-PDT treatment.

Meanwhile, X-PDT did not cause detectable systematic toxicities. These include no signs of side effects to normal tissues from H&E staining (**Figure 5.6a**). Also, hemodiagnosis found that the serum aspartate aminotransferase (AST) and alanine aminotransferase (ALT) levels remained

unchanged over the course of the treatment, again suggesting low toxicities (**Figure 5.6b**). This is in accordance with our previous observations that i.v. injected MC540-SAO:Eu@mSiO_2 nanoparticles are degraded after the conclusion of therapy and efficiently cleared from the hosts [87].

Discussions

While initially developed as a PDT derivative, the current study suggests that X-PDT is essentially a PDT and RT combination. While a portion of X-ray energy was converted to activate PDT, ionizing radiation continues playing an important role in X-PDT. The PDT and RT components target different cellular components and the combination causes enhanced effect that is beyond the repairs of cells. This explains the greater cytotoxicity with X-PDT than with RT, especially for cells that are refractory to RT. In fact, previous studies have observed synergy between PDT and RT [168-171]. However, it was found that PDT and ionizing irradiation need to be given at the same time so as to override cell repairs [168, 169]. This requires photo-irradiation and X-ray irradiation to be applied simultaneously, which is difficult to achieve in the clinic, not to mention the shallow penetration of PDT. X-PDT, on the other hand, is an inherent PDT and RT combination, with both processes regulated by one deep-penetrating radiation. From this perspective, X-PDT represents a major advance for seamlessly integrating PDT and RT. In this sense, X-PDT should be viewed as not only a PDT derivative but also a RT derivative.

RT remains a major therapy option in clinical oncology. More than 50% of all cancer patients receive RT during their curative process [172]. One major limitation of RT is that not all cancer cells are well responsive to RT, and tumors that are originally responsive may develop resistance over the course of therapy [173]. Increasing radiation doses can, to a certain degree, address the issue, but will inevitably cause collateral damage to normal tissues [174].

Radiosensitizing agents of different types have been developed to sensitize cancer cells to RT; however, many radiosensitizers are cytotoxic agents [175]. As discussed above, X-PDT can be viewed as a RT derivative and as such a novel radiosensitizing technology. This was confirmed by our clonogenic assays, which observed a high DEF with X-PDT, even against cells that are refractory to RT. Unlike many conventional radiosensitizers, MC540-SAO:Eu@mSiO_2 nanoparticles are not toxic in the absence of radiation. Meanwhile, they are highly biodegradable, efficiently cleared out of the hosts after treatment, and causing no side effects to normal tissues (**Figure 5.6**). These properties suggest great promise of X-PDT in clinic translation to improve RT efficacy, reduce normal tissue radiation exposure, and battle with radioresistant tumors. In the present studies, nanoparticles were directly injected into tumors. In the future studies, it is worthwhile to reduce nanoparticle size, improve photosensitizer loading, and conjugating targeting ligands to the nanoparticle surface for achieve formulations that can be systematically injected to mediate tumor selective X-PDT treatment.

Conclusions

In summary, we investigated in this study the impacts of X-PDT on cancer cells. We found that X-PDT is not simply a PDT process; rather, it is essentially a RT and PDT combination. The combination leads to enhanced therapy effects that make the treatment much more efficient than RT alone, even when used against cells that are refractory to RT. We also show that X-PDT can be exploited to suppress tumors lain under deep tissues. The findings and advances are of great value to the developments of X-PDT as a novel treatment modality against cancer.

Materials and Methods

Nanoparticle synthesis and coating

SAO:Eu was synthesized by a carbo-thermal reduction and vapor-phase deposition method that was published previously [111]. To render SAO:Eu amenable to bio-related applications, bulk SAO:Eu was ground into nanoparticles with a diameter of ~ 80 nm. The bare SAO:Eu nanoparticles were coated with a layer of solid silica by following a previously published protocol [87]. In a typical synthesis, 10 mg of SAO:Eu nanoparticles were dispersed in a mixture of 25 mL of ethanol, 2 mL of H_2O, and 1 mL of ammonia (25%), and stirred for 10 min. Then, 75 µL of tetraethyl orthosilicate (TEOS) was added to solution and the mixture was stirred at room temperature for 12 hours. The resulting nanoparticles were subsequently coated with a layer of mesoporous silica. A mixture of 3-aminopropyltriethoxysilane and TEOS (5 v/v%) was used as silane precursors [157]. Solid silica coated SAO:Eu nanoparticles (10 mg) from the first step were dispersed in a mixture of 45 mL of H_2O, 0.3 mL of 2 M NaOH, and 10 mg of cetyltrimethylammonium bromide (CTAB) for 30 min. After heating to 70 ^oC, 50 µL of TEOS and 300 µL of ethyl acetate were added, and the solution was magnetically stirred for 2 h. The raw products were collected by centrifugation and washed with ethanol for three times. The resulting nanoparticles were re-suspended in ethanol (20 mL) and mixed with NH_4NO_3 (100 mg) at 60 ^oC for 2 hours to remove CTAB. For photosensitizer loading, MC540 (Invitrogen) were dispersed in ethanol with SAO:Eu@$mSiO_2$ nanoparticles. The mixture was incubated overnight at room temperature [87]. After centrifuging and washing several times, and the supernatant removed. The MC540-loaded nanoparticles were resuspended in PBS (Thermo Scientific) for further studies.

Characterizations of SAO:Eu and MC540-SAO:Eu@$mSiO_2$ nanoparticles

UV-Vis absorption spectra were recorded on a Shimdzu 2450 UV-Vis spectrometer. Photoluminescence measurements were performed on a Hitachi F-7000 fluorometer. A mini-X X-ray tube (Amptek Inc.) was used as the X-ray source, and was set at 50 kV and 70 μI for all the experiments in this study. TEM samples were prepared by dripping sample solutions onto carbon-coated copper grids and evaporating the solvent. TEM images were taken on an FEI Tecnai 20 transmission electron microscope operating at 200 kV.

Cell culture

H1299, a human NSCLC cell line, was used in in vitro and in vivo studies. The H1299 cells have been transfected to stably express firefly luciferase (i.e. H1299-Luc). The cells had been tested and were rodent pathogens free. H1299-Luc cells were grown in RPMI 1640 medium supplemented with 10% FBS, 100 units/mL of penicillin (ATCC) and 250 μg/mL hygromycin. The cells were maintained in a humidified, 5 % carbon dioxide (CO_2) atmosphere at 37 °C.

In vitro toxicity study

10^4 H1299 cells were seeded in 96-well plates (Corning) and cultured to 90% confluency. For cytotoxicity studies, the cells were then incubated with 0, 5, 10, 25, 50 and 100 μg/mL MC540-SAO:Eu@$mSiO_2$ nanoparticles for 24 h. Subsequently, they were washed with PBS for two times, and then were evaluated by MTT assay (Sigma Aldrich) by following the vendor's protocols.

In vitro viability study

10^4 H1299 cells were seeded in 96-well plates (Corning) and cultured for 24 h. The cells were then divided into 5 groups: 1) PBS group, 2) MC540-SAO:Eu@$mSiO_2$ nanoparticles only, 3) MC540 only, 4) RT only, and 5) X-PDT. For Group 2 and 5, the final concentration of

MC540-SAO:Eu@mSiO$_2$ nanoparticles was 50 μg/mL and the incubation time was 1 hour. All the cells were incubated in the dark. Cells in Group 4 and 5 were irradiated with 50 kV X-ray at 0.83, 1.67, 3.33 and 5 Gy while all the other cells received irradiation. After the treatment, all cells were washed with PBS for two times. Cell culture medium was replenished and the incubation was maintained for 24 h (5 % CO_2 and 37 °C). Cell viabilities were evaluated by MTT assays (Sigma Aldrich) following the vendor's protocol.

Apoptosis/necrosis/healthy assay

H1299-Luc cells treated with X-PDT (5 Gy), RT (5 Gy) and PBS were subjected to Apoptotic/Necrotic/Healthy assay (PromoCell GmbH, Heidelberg, Germany) following the vendor's protocol. Briefly, FITC-annexin V (green) binds to the apoptosis marker of phosphatidyl serine, and ethidium homodimer III (red) binds to DNA under the necrotic conditions. The cells stained with annexin V antibody alone or together with ethidium homodimer III were counted as early or late stages of apoptotic cells, respectively [34]. The cells labeled with ethidium homodimer III alone were counted as necrotic cells. In addition, membrane permeable Hoechst 33342 (blue) stains the nuclei. Healthy cells would only display blue staining. The resulted cells were then evaluated by fluorescent imaging on an Olympus IX71 fluorescent microscope (3 trials per group).

Clonogenic assay

Mono-layered H1299-Luc cells were prepared in 6-well cell petri-dishes one day before the experiments. On the experimental day, the 6-well cell petri-dishes were randomly divided into the control group, the X-ray radiation group, and the X-PDT group. The two treatment groups were treated by X-ray (50 kv) for a dose of 1, 2.5, 5, 7.5 and 10 Gy while the control group received no irradiation. The irradiated and un-treated cells were then harvested using

trypsin-EDTA and plated into 100 mm cell petri-dishes. Each petri-dish was seeded with 100 viable cells and was placed into a cell culture incubator (5% CO_2 and 37°C) for 14 days. After incubation for 14 days, the cells were fixed by formalin and stained with 0.5% Gentian Violet. Colonies containing more than 50 cells were counted and the survival fractions were calculated by comparing to the control. Dose enhancement factor (DEF) was calculated as the ratio between RT and X-PDT radiation doses at 10% survival fractions. All the experiments were repeated 3 times.

Lipid peroxidation assay

Lipid peroxidation levels were measured using Image-iT® Lipid Peroxidation Kit (Life Technologies Corporation, Carlsbad, CA) by following the vendor's protocol. Briefly, H1299-Luc cells seeded in 6-well petri-dishes were treated with RT or X-PDT under 5 Gy X-ray irradiation. Un-irradiated cells were used as control. The Image-iT reagent was incubated with cells for 30 min. The cells were washed three times with PBS and observed on an Olympus IX71 fluorescence microscope. Data were analyzed by ImageJ (NIH, Bethesta, Maryland, U.S.). The experiments were repeated 5 times.

Single cell gel electrophoresis (comet assay)

Mono-layered cells were prepared in 6-well cell petri-dishes one day before the experiments. On the experimental day, the 6-well cell petri-dishes were randomly divided into the control group, the X-ray radiation group, and the X-PDT (with MC540-SAO:Eu@mSiO_2) group. Then the two treatment groups were irradiated by X-ray (50 kV) for a dose of 5 Gy while the control group received 0 dose irradiation. The irradiated and un-treated cells were then harvested. 1×10^5/mL of the treated cells were immediately combined with molten LMAgarose (at 37°C) at a ratio of 1:10 (v/v). 50 μL of the solution was pipetted onto a CometSlide™

(Trevigen Inc., Gaithersburg, MD). The slide was then immersed in 4°C lysis solution for 1 hour or overnight. After that, ~850 ml 4°C 1× neutral electrophoresis buffer was added to the electrophoresis gel box and the slides were placed in a slide tray. The power supply was set at 21 volts. After 45 minutes, the slides were gently removed and immersed in DNA Precipitation Solution for 30 minutes, and then in 70% ethanol for 30 minutes at room temperature. The slides were dried and stained in SYBR® safe for 30 min in the dark. The slides were then ready for microscopic imaging.

Western blot

Approximately 5×10^5 H1299-Luc cells were seeded in a 6-well plate prior to radiation therapy. Cells were harvested 1 hours and 24 hours after the treatment. The cells were lysed in a lysis buffer. Proteins were separated by pre-cast 12% Bis-Tris NuPage™ SDS-PAGE (Life Sciences™), transferred to iBlot® polyvinylidene difluoride membrane (Invitrogen™, Grand Island, NY, USA), and immunoblotted using primary antibodies against COX2, H2AX, and β-actin. HRP-conjugated secondary antibody (Cell Signaling Technology, Danvers, MA, USA) was applied subsequently. The protein bands were then visualized with SuperSignal™ West Pico Chemiluminescent Substrate (Thermo Fisher Scientific) using a Fluorchem HD2 chemiluminescent imaging system (Protein Simple, Santa Clara, CA).

Animal studies

All the animal studies conformed to the Guide for the Care and Use of Laboratory Animals published by the National Institutes of Health, USA, and a protocol approved by the Institutional Animal Care and Use Committee (IACUC), University of Georgia. Nude mice (4–6 weeks old, Harlan) with a body weight of ~20 g were used for the animal model establishment.

The animals were housed in alternating lighting conditions under a 12 h dark and 12 h light regime.

Therapy studies with subcutaneous tumor models

15 nude 5−6 week athymic nude mice were randomly divided into three groups, 1) control group, 2) 1-cm thick pork group, and 3) 2-cm thick pork group. Animal models were established by subcutaneous injection of 5×10^5 H1299-Luc tumor cells onto the hind legs of mice. When tumor sizes reached 100 nm, 100 μL PBS solution containing MC540-SAO:Eu@$mSiO_2$ nanoparticles (4.25 mg/kg) was intratumorally injected in Group 2 and 3. The same amount of PBS was injected into the tumors of the control group. For therapy studies, irradiation (5 Gy) was applied to tumors, with the rest of the animal body covered by lead. The control group received no irradiation.

Therapy studies with cancer cells implanted into the lungs

20 nude mice were randomized to receive the following treatments group (n = 5): 1) PBS, 2) MC540-SAO:Eu@$mSiO_2$ only, 3) RT only, and 4) X-PDT (MC540-SAO:Eu@$mSiO_2$ plus RT). 5×10^5 H1299-Luc cells were injected into the left lateral thorax of anesthetized nude mice. For Group 1 and 3, PBS solution was premixed with the cells into a final volume of 50 μL. For group 2 and 4, nanoparticles were premixed with cells into a final volume 50 μL matrigel solutions (2.5 mg MC540-SAO:Eu@$mSiO_2$/mL, or 1.7 mg SAO:Eu/mL). Group 1 and 2 received no X-ray irradiation. Group 3 and group 4 received X-ray irradiation (5 Gy) 5 minutes after the injection. Only one therapy dose was given to each animal. The tumor growth was monitored BLI by an IVIS Lumina scanner (PerkinElmer Inc. Waltham, Massachusetts). Tumors and major organs from the euthanized animals were harvested, weighed, and cryosectioned. The tissue sections were then subjected to standard H&E staining to assess treatment outcomes and

side effects (BBC Biochemical). Hemodiagnosis assay was performed by withdrawing the blood before the treatment as well as before euthanizing the mice. The concentrations of AST and ALT were determined by using commercial kits from Thermo-Scientific.

Statistical analyses

Quantitative data were expressed as mean ± s.e.m. A two-tailed Student's t-test was used for statistically comparing the treatment group and the control group. $P < 0.05$ was considered statistically significant.

TOC

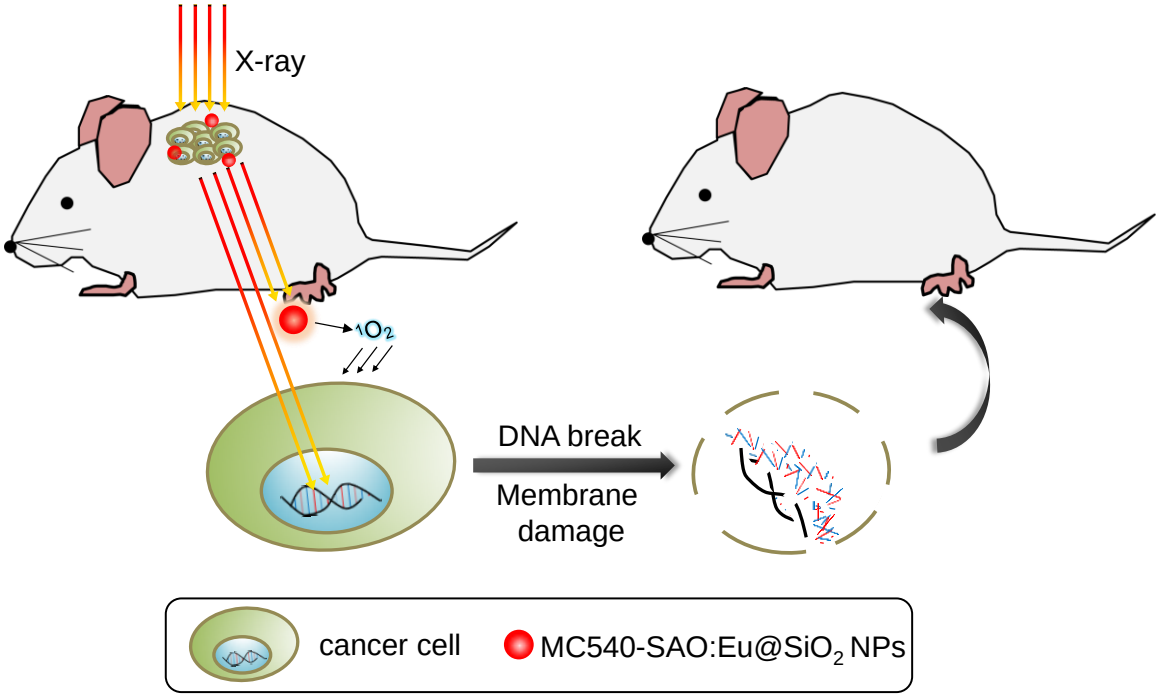
X-ray
$^1O_2$
DNA break
Membrane
damage
cancer cell
MC540-SAO:Eu@SiO$_2$ NPs

Supplemental Information

Singlet oxygen generation efficiency

The $^1O_2$ production efficiency was calculated based on a published method [176]. Briefly, the X-PDT process can be broken into three steps. Firstly, SAO:Eu nanoparticles were irradiated by X-ray to emit luminescence. Second, the XEOL activates near-by photosensitizers (MC540). Lastly, $^1O_2$ is produced. From energy transformation perspective, the whole process can be regarded as a conversion from the electromagnetic energy (the ionizing radiation) to chemical energy (the $^1O_2$). The conversion efficiency (η) can be calculated from the following equation:

$$\eta = \frac{E_c}{E_{em}}$$

where E_c is the chemical energy, i.e. the energy increase when oxygen molecules are converted to singlet oxygen molecules.

The energy difference between the lowest energy of O_2 in the singlet state and the lowest energy in the triplet state is about 94.3 kJ/mol (i.e. 0.98 eV) [177, 178]. Therefore, E_c can be calculated from:

$$E_c = 0.98 \times N_A \times Y(\mathrm{J}) = 0.94 \times 10^5 \times Y(\mathrm{J})$$

where N_A is the Avogadro's constant (6.02×10^{23}), 1 eV=1.6×10^{-19} J, and Y (mol) is the amount of singlet oxygen generated from the X-PDT process.

Y can be estimated from our singlet oxygen generation data (Figure 2b) using a published method [176]. When there is excess MC540, the ratio between the reactants is 1:1 in the O_2-$^1O_2$-

MC540 reaction [22, 176, 178-180]. Hence, Y is equal to the amount of the activated MC540 resulting from the photodynamic effect:

$$Y = \mathrm{n}_0 \times (\mathrm{b}_\mathrm{m} - \mathrm{b}_\mathrm{c}) = W_{MC540} / M_{MC540} \times (\mathrm{b}_\mathrm{m} - \mathrm{b}_\mathrm{c}) = 4.5 \times 10^{-9} \times (\mathrm{b}_\mathrm{m} - \mathrm{b}_\mathrm{c})(\mathrm{mol})$$

where n_0 is the initial content of MC540 (5 wt% of 1 mL solution of 50 mg/L, M_{MC540} = 553.6 g/mol), and (b_m-b_c) is the relative percentage change of SOSG fluorescence signals [176]. As shown in Figure 3b, the value of (b_m-b_c) is approximately equal to the difference between the control group and the MC540-SAO:Eu@mSiO_2 group in the ordinate value at a given radiation dose. From the above two equations, E_c can be rewritten as:

$$E_c = 0.94 \times 10^5 \times Y = 4.2 \times 10^{-4} \times (\mathrm{b}_\mathrm{m} - \mathrm{b}_\mathrm{c})(\mathrm{mol})$$

Meanwhile, E_{em} is the electromagnetic energy in the form of X-ray, which is dependent on the radiation dose (D, Gy). By definition, 1 Gy is equal to an absorbed dose of 1 J/kg. Considering that 1 mL (1 g) aqueous solution was used in the experiment, E_{em} can thus be calculated as:

$$E_{em} = 1 \times 10^{-3} \times D(\mathrm{J})$$

Hence,

$$\eta = \frac{E_c}{E_{em}} = \frac{4.2 \times 10^{-4} \times (\mathrm{b}_m - \mathrm{b}_c)}{1 \times 10^{-3} \times D} = 0.42 \times \frac{(\mathrm{b}_m - \mathrm{b}_c)}{D}$$

Using the above equation we computed $^1O_2$ production efficiency at different irradiation doses and the results were listed in Table S1.

Table S1. $^1O_2$ production efficiency (η) of X-PDT at different X-ray radiation doses (D) (X-ray dose rate is 0.2 Gy/min).

D/Gy	$\mathbf{b_m}$-$\mathbf{b_c}$	$\boldsymbol{\eta}$
1	7%	2.9%
2	20%	4.2%
3	32%	4.5%
4	41%	4.3%

It can be seen that η values at different D are comparable. An average of the η values in Table 1, 3.9%, was reported in the main text.

Supplemental Figures

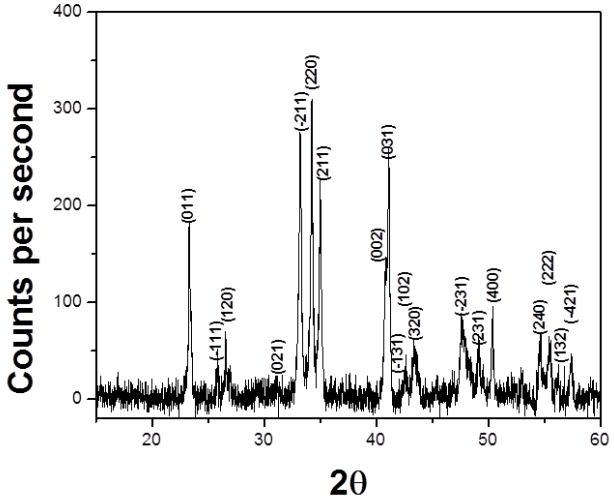

Figure S5.1. X-ray diffraction (XRD) analysis result. The main product is monoclinic $SrAl_2O_4$ (JCPDS #74-0794).

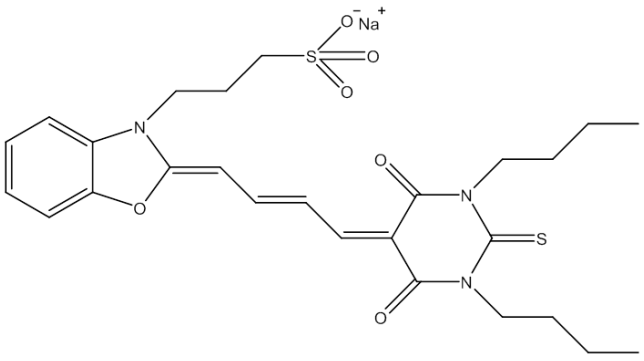

Figure S5.2. Chemical structure of merocyanine 540 (MC 540).

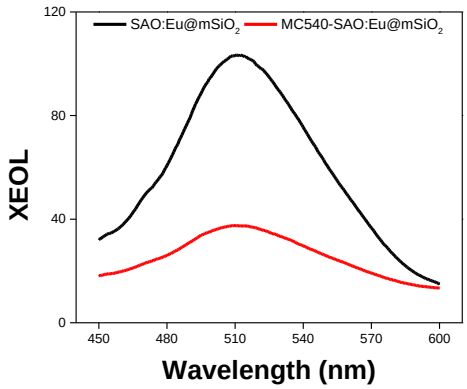

Figure S5.3. X-ray excited optical luminescence (XEOL) of SAO:Eu@mSiO$_2$ before and after loaded with MC540 photosenstizers.

REFERENCES

1. Shen, D., et al., *Biphase stratification approach to three-dimensional dendritic biodegradable mesoporous silica nanospheres.* Nano Lett, 2014. **14**(2): p. 923-32.
2. He, Q.J., et al., *The three-stage in vitro degradation behavior of mesoporous silica in simulated body fluid.* Microporous and Mesoporous Materials, 2010. **131**(1-3): p. 314-320.
3. Chaudhry, Q., et al., *Applications and implications of nanotechnologies for the food sector.* Food Additives and Contaminants Part a-Chemistry Analysis Control Exposure & Risk Assessment, 2008. **25**(3): p. 241-258.
4. de Azeredo, H.M.C., *Antimicrobial nanostructures in food packaging.* Trends in Food Science & Technology, 2013. **30**(1): p. 56-69.
5. Kim, J.E., et al., *Gold-based hybrid nanomaterials for biosensing and molecular diagnostic applications.* Biosensors & Bioelectronics, 2016. **80**: p. 543-559.
6. Lu, W.F., H. Hong, and W.B. Cai, *Radio-nanomaterials for biomedical applications: state of the art.* European Journal of Nanomedicine, 2016. **8**(3): p. 151-170.
7. Lu, J., et al., *The role of nanotechnology in the development of battery materials for electric vehicles.* Nature Nanotechnology, 2016. **11**(12): p. 1031-1038.
8. Holmes, A.B. and F.X. Gu, *Emerging nanomaterials for the application of selenium removal for wastewater treatment.* Environmental Science-Nano, 2016. **3**(5): p. 982-996.
9. Zhou, Q.X., et al., *Iron-based magnetic nanomaterials and their environmental applications.* Critical Reviews in Environmental Science and Technology, 2016. **46**(8): p. 783-826.
10. Kim, E.S., et al., *Emerging nanotechnology approaches in tissue engineering and regenerative medicine.* International Journal of Nanomedicine, 2014. **9**: p. 1-5.
11. WHO, *Estimates for 2000–2012 CAUSE-SPECIFIC MORTALITY*. 2012, World Health Organization: http://www.who.int/healthinfo/global_burden_disease/estimates/en/index1.html.
12. Siegel, R.L., K.D. Miller, and A. Jemal, *Cancer Statistics, 2016.* Ca-a Cancer Journal for Clinicians, 2016. **66**(1): p. 7-30.
13. Damadian, R., *Tumor Detection by Nuclear Magnetic Resonance.* Science, 1971. **171**(3976): p. 1151-&.
14. La Mar, G.N., W.D. Horrocks, and R.H. Holm, *NMR of paramagnetic molecules; principles and applications*. 1973, New York,: Academic Press. xv, 678 p.
15. Dwek, R.A., *Nuclear magnetic resonance (N.M.R.) in biochemistry : applications to enzyme systems*. Monographs on physical biochemistry. 1973, Oxford Eng.: Clarendon Press. xviii, 395 p.
16. Burton, D.R., et al., *Proton Relaxation Enhancement (Pre) in Biochemistry - Critical Survey.* Progress in Nuclear Magnetic Resonance Spectroscopy, 1979. **13**: p. 1-45.
17. Norek, M. and J.A. Peters, *MRI contrast agents based on dysprosium or holmium.* Progress in Nuclear Magnetic Resonance Spectroscopy, 2011. **59**(1): p. 64-82.

18. Fries, P.H. and E. Belorizky, *Electronic relaxation of paramagnetic metal ions and NMR relaxivity in solution: Critical analysis of various approaches and application to a Gd(III)-based contrast agent.* Journal of Chemical Physics, 2005. **123**(12).
19. Peters, J.A., J. Huskens, and D.J. Raber, *Lanthanide induced shifts and relaxation rate enhancements.* Progress in Nuclear Magnetic Resonance Spectroscopy, 1996. **28**: p. 283-350.
20. Aime, S., et al., *Lanthanide(III) chelates for NMR biomedical applications.* Chemical Society Reviews, 1998. **27**(1): p. 19-29.
21. Lim, C.K., et al., *Nanophotosensitizers toward advanced photodynamic therapy of Cancer.* Cancer Letters, 2013. **334**(2): p. 176-187.
22. Lovell, J.F., et al., *Activatable photosensitizers for imaging and therapy.* Chem Rev, 2010. **110**(5): p. 2839-57.
23. Sharman, W.M., C.M. Allen, and J.E. van Lier, *Photodynamic therapeutics: basic principles and clinical applications.* Drug Discov Today, 1999. **4**(11): p. 507-517.
24. Baban, D.F. and L.W. Seymour, *Control of tumour vascular permeability.* Advanced Drug Delivery Reviews, 1998. **34**(1): p. 109-119.
25. Dougherty, T.J., et al., *Photodynamic therapy.* Journal of the National Cancer Institute, 1998. **90**(12): p. 889-905.
26. McCaughan, J.S., *A Clinical manual : photodynamic therapy of malignancies*. 1992, Austin
Boca Raton, FL: R.G. Landes Co. ;
Distributed by CRC Press. vii, 248 p.
27. Etcheverry, M.E., M.A. Pasquale, and M. Garavaglia, *Photodynamic therapy of HeLa cell cultures by using LED or laser sources.* Journal of Photochemistry and Photobiology B-Biology, 2016. **160**: p. 271-277.
28. Nadine Barrie Smith, A.W., *Introduction to Medical Imaging: Physics, Engineering and Clinical Applications: 5 Magnetic resonance imaging MRI*. 2010: Cambridge University Press.
29. Perazella, M.A., *Gadolinium-contrast toxicity in patients with kidney disease: nephrotoxicity and nephrogenic systemic fibrosis.* Curr Drug Saf, 2008. **3**(1): p. 67-75.
30. Chrysochou, C., et al., *Low risk for nephrogenic systemic fibrosis in nondialysis patients who have chronic kidney disease and are investigated with gadolinium-enhanced magnetic resonance imaging.* Clin J Am Soc Nephrol, 2010. **5**(3): p. 484-9.
31. Perazella, M.A., *Nephrogenic systemic fibrosis, kidney disease, and gadolinium: is there a link?* Clin J Am Soc Nephrol, 2007. **2**(2): p. 200-2.
32. Thomsen, H.S., S.K. Morcos, and P. Dawson, *Is there a causal relation between the administration of gadolinium based contrast media and the development of nephrogenic systemic fibrosis (NSF)?* Clin Radiol, 2006. **61**(11): p. 905-6.
33. Thomsen, H.S., *Nephrogenic systemic fibrosis: A serious late adverse reaction to gadodiamide.* Eur Radiol, 2006. **16**(12): p. 2619-21.
34. Hellman, R.N., *Gadolinium-induced nephrogenic systemic fibrosis.* Semin Nephrol, 2011. **31**(3): p. 310-6.
35. Bridot, J.L., et al., *Hybrid gadolinium oxide nanoparticles: multimodal contrast agents for in vivo imaging.* J Am Chem Soc, 2007. **129**(16): p. 5076-84.
36. Vivero-Escoto, J.L., et al., *Biodegradable Polysilsesquioxane Nanoparticles as Efficient Contrast Agents for Magnetic Resonance Imaging.* Small, 2013. **9**(20): p. 3523-3531.

37. Zhou, Z., et al., *A synergistically enhanced T(1) -T(2) dual-modal contrast agent.* Adv Mater, 2012. **24**(46): p. 6223-8.
38. Cao, L., et al., *Competitive performance of carbon "quantum" dots in optical bioimaging.* Theranostics, 2012. **2**(3): p. 295-301.
39. Choi, H.S., et al., *Design considerations for tumour-targeted nanoparticles.* Nature Nanotechnology, 2010. **5**(1): p. 42-47.
40. Bourlinos, A.B., et al., *Surface functionalized carbogenic quantum dots.* Small, 2008. **4**(4): p. 455-8.
41. Chen, H., et al., *Label-free luminescent mesoporous silica nanoparticles for imaging and drug delivery.* Theranostics, 2013. **3**(9): p. 650-7.
42. Ren, X., et al., *Facile preparation of gadolinium(iii) chelates functionalized carbon quantum dot-based contrast agent for magnetic resonance/fluorescence multimodal imaging.* Journal of Materials Chemistry B, 2014.
43. Bourlinos, A.B., et al., *Gd(III)-doped carbon dots as a dual fluorescent-MRI probe.* Journal of Materials Chemistry, 2012. **22**(44): p. 23327-23330.
44. Li, W., et al., *Simple and green synthesis of nitrogen-doped photoluminescent carbonaceous nanospheres for bioimaging.* Angew Chem Int Ed Engl, 2013. **52**(31): p. 8151-5.
45. Bhunia, S.K., et al., *Carbon nanoparticle-based fluorescent bioimaging probes.* Sci Rep, 2013. **3**: p. 1473.
46. Sun, Y.P., et al., *Quantum-sized carbon dots for bright and colorful photoluminescence.* J Am Chem Soc, 2006. **128**(24): p. 7756-7.
47. Ding, C., A. Zhu, and Y. Tian, *Functional Surface Engineering of C-Dots for Fluorescent Biosensing and in Vivo Bioimaging.* Acc Chem Res, 2013.
48. Michalet, X., et al., *Quantum dots for live cells, in vivo imaging, and diagnostics.* Science, 2005. **307**(5709): p. 538-44.
49. Song, S., et al., *Functional nanoprobes for ultrasensitive detection of biomolecules.* Chem Soc Rev, 2010. **39**(11): p. 4234-43.
50. Kim, T., et al., *Mesoporous silica-coated hollow manganese oxide nanoparticles as positive T1 contrast agents for labeling and MRI tracking of adipose-derived mesenchymal stem cells.* J Am Chem Soc, 2011. **133**(9): p. 2955-61.
51. Kalavagunta, C., S. Michaeli, and G.J. Metzger, *In vitro Gd-DTPA relaxometry studies in oxygenated venous human blood and aqueous solution at 3 and 7 T.* Contrast Media Mol Imaging, 2014. **9**(2): p. 169-76.
52. Huang, C.H. and A. Tsourkas, *Gd-based macromolecules and nanoparticles as magnetic resonance contrast agents for molecular imaging.* Curr Top Med Chem, 2013. **13**(4): p. 411-21.
53. Corot, C., et al., *Structure-activity relationship of macrocyclic and linear gadolinium chelates: investigation of transmetallation effect on the zinc-dependent metallopeptidase angiotensin-converting enzyme.* J Magn Reson Imaging, 1998. **8**(3): p. 695-702.
54. Wu, X., et al., *Stability and biodistribution of a biodegradable macromolecular MRI contrast agent Gd-DTPA cystamine copolymers (GDCC) in rats.* Pharm Res, 2010. **27**(7): p. 1390-7.
55. Aime, S. and P. Caravan, *Biodistribution of gadolinium-based contrast agents, including gadolinium deposition.* J Magn Reson Imaging, 2009. **30**(6): p. 1259-67.

56. Ye, Y. and X. Chen, *Integrin targeting for tumor optical imaging.* Theranostics, 2011. **1**: p. 102-26.
57. Jokerst, J.V., et al., *Nanoparticle PEGylation for imaging and therapy.* Nanomedicine (Lond), 2011. **6**(4): p. 715-28.
58. Liu, D., A. Mori, and L. Huang, *Role of liposome size and RES blockade in controlling biodistribution and tumor uptake of GM1-containing liposomes.* Biochim Biophys Acta, 1992. **1104**(1): p. 95-101.
59. Choi, H.S., et al., *Design considerations for tumour-targeted nanoparticles.* Nat Nanotechnol, 2010. **5**(1): p. 42-7.
60. Gao, J., et al., *A novel clinically translatable fluorescent nanoparticle for targeted molecular imaging of tumors in living subjects.* Nano Lett, 2012. **12**(1): p. 281-6.
61. Liu, J.B., et al., *Renal clearable inorganic nanoparticles: a new frontier of bionanotechnology.* Materials Today, 2013. **16**(12): p. 477-486.
62. Wang, J., C.F. Wang, and S. Chen, *Amphiphilic egg-derived carbon dots: rapid plasma fabrication, pyrolysis process, and multicolor printing patterns.* Angew Chem Int Ed Engl, 2012. **51**(37): p. 9297-301.
63. Liu, S., et al., *Hydrothermal Treatment of Grass: A Low-Cost, Green Route to Nitrogen-Doped, Carbon-Rich, Photoluminescent Polymer Nanodots as an Effective Fluorescent Sensing Platform for Label-Free Detection of Cu(II) Ions.* Advanced Materials, 2012. **24**(15): p. 2037-2041.
64. Huang, J., et al., *Effects of nanoparticle size on cellular uptake and liver MRI with polyvinylpyrrolidone-coated iron oxide nanoparticles.* ACS Nano, 2010. **4**(12): p. 7151-60.
65. Zhou, Z., et al., *Engineered iron-oxide-based nanoparticles as enhanced T1 contrast agents for efficient tumor imaging.* ACS Nano, 2013. **7**(4): p. 3287-96.
66. Na, H.B., I.C. Song, and T. Hyeon, *Inorganic Nanoparticles for MRI Contrast Agents.* Advanced Materials, 2009. **21**(21): p. 2133-2148.
67. Chen, H.M., et al., *Nanoparticles for improving cancer diagnosis.* Materials Science & Engineering R-Reports, 2013. **74**(3): p. 35-69.
68. Chen, H.M., et al., *Gd-Encapsulated Carbonaceous Dots with Efficient Renal Clearance for Magnetic Resonance Imaging.* Advanced Materials, 2014. **26**(39): p. 6761-6766.
69. Yang, H., et al., *RGD-Conjugated Nanoscale Coordination Polymers for Targeted T-1- and T-2-weighted Magnetic Resonance Imaging of Tumors in Vivo.* Advanced Functional Materials, 2014. **24**(12): p. 1738-1747.
70. Chen, H.M., et al., *Mesoporous Silica as Nanoreactors to Prepare Gd-Encapsulated Carbon Dots of Controllable Sizes and Magnetic Properties.* Advanced Functional Materials, 2016. **26**(22): p. 3973-3982.
71. Caravan, P., *Strategies for increasing the sensitivity of gadolinium based MRI contrast agents.* Chemical Society Reviews, 2006. **35**(6): p. 512-523.
72. Corot, C., et al., *Recent advances in iron oxide nanocrystal technology for medical imaging.* Advanced Drug Delivery Reviews, 2006. **58**(14): p. 1471-1504.
73. Krupa, K. and M. Bekiesinska-Figatowska, *Artifacts in magnetic resonance imaging.* Pol J Radiol, 2015. **80**: p. 93-106.
74. Kircher, M.F., et al., *A brain tumor molecular imaging strategy using a new triple-modality MRI-photoacoustic-Raman nanoparticle.* Nature Medicine, 2012. **18**(5): p. 829-U235.

75. Kim, J., et al., *Multifunctional uniform nanoparticles composed of a magnetite nanocrystal core and a mesoporous silica shell for magnetic resonance and fluorescence imaging and for drug delivery.* Angew Chem Int Ed Engl, 2008. **47**(44): p. 8438-41.
76. Fan, W., et al., *Rattle-structured multifunctional nanotheranostics for synergetic chemo-/radiotherapy and simultaneous magnetic/luminescent dual-mode imaging.* J Am Chem Soc, 2013. **135**(17): p. 6494-503.
77. Yang, H., et al., *Targeted dual-contrast T-1- and T-2-weighted magnetic resonance imaging of tumors using multifunctional gadolinium-labeled superparamagnetic iron oxide nanoparticles.* Biomaterials, 2011. **32**(20): p. 4584-4593.
78. Li, Z., et al., *Ultrasmall Water-Soluble and Biocompatible Magnetic Iron Oxide Nanoparticles as Positive and Negative Dual Contrast Agents.* Advanced Functional Materials, 2012. **22**(11): p. 2387-2393.
79. Zhou, Z.J., et al., *A Synergistically Enhanced T-1-T-2 Dual-Modal Contrast Agent.* Advanced Materials, 2012. **24**(46): p. 6223-6228.
80. Choi, J.S., et al., *Self-confirming "AND" logic nanoparticles for fault-free MRI.* J Am Chem Soc, 2010. **132**(32): p. 11015-7.
81. Shin, T.H., et al., *T(1) and T(2) dual-mode MRI contrast agent for enhancing accuracy by engineered nanomaterials.* ACS Nano, 2014. **8**(4): p. 3393-401.
82. Della Rocca, J., D. Liu, and W. Lin, *Nanoscale metal-organic frameworks for biomedical imaging and drug delivery.* Acc Chem Res, 2011. **44**(10): p. 957-68.
83. Alley, M.C., et al., *Feasibility of Drug Screening with Panels of Human-Tumor Cell-Lines Using a Microculture Tetrazolium Assay.* Cancer Research, 1988. **48**(3): p. 589-601.
84. Lee, H.J., et al., *Synthesis and photoluminescence properties of Eu3+-doped silica@coordination polymer core-shell structures and their calcinated silica@Gd2O3:Eu and hollow Gd2O3:Eu microsphere products.* Small, 2013. **9**(4): p. 561-9.
85. Kuda-Wedagedara, A.N.W., et al., *Aqueous Eu-II-Containing Complex with Bright Yellow Luminescence.* Journal of the American Chemical Society, 2015. **137**(15): p. 4960-4963.
86. Liz-Marzan, L.M., M. Giersig, and P. Mulvaney, *Synthesis of nanosized gold-silica core-shell particles.* Langmuir, 1996. **12**(18): p. 4329-4335.
87. Chen, H., et al., *Nanoscintillator-mediated X-ray inducible photodynamic therapy for in vivo cancer treatment.* Nano Lett, 2015. **15**(4): p. 2249-56.
88. Luo, Y.X., et al., *Electric field induced structural color changes of SiO2@TiO2 core-shell colloidal suspensions.* Journal of Materials Chemistry C, 2014. **2**(11): p. 1990-1994.
89. Kang, J.G., et al., *Full characterization of Eu(OH)(3) and Eu2O3 nanorods.* Applied Surface Science, 2014. **314**: p. 158-165.
90. Peng, M.Y. and G.Y. Hong, *Reduction from Eu3+ to Eu2+ in BaAl2O4 : Eu phosphor prepared in an oxidizing atmosphere and luminescent properties of BaAl2O4 : Eu.* Journal of Luminescence, 2007. **127**(2): p. 735-740.
91. Wang, Z., et al., *Solid-state synthesis and luminescent properties of yellow-emitting phosphor NaY(MoO4)2:Dy3+ for white light-emitting diodes.* Luminescence, 2015. **30**(6): p. 842-6.
92. Cowger, T.A., et al., *Casein-Coated Fe5C2 Nanoparticles with Superior r2 Relaxivity for Liver-Specific Magnetic Resonance Imaging.* Theranostics, 2015. **5**(11): p. 1225-32.

93. Wartenberg, N., et al., *A gadolinium complex confined in silica nanoparticles as a highly efficient T1/T2 MRI contrast agent.* Chemistry, 2013. **19**(22): p. 6980-3.
94. Estelrich, J., M.J. Sanchez-Martin, and M.A. Busquets, *Nanoparticles in magnetic resonance imaging: from simple to dual contrast agents.* Int J Nanomedicine, 2015. **10**: p. 1727-41.
95. Ruoslahti, E., *RGD and other recognition sequences for integrins.* Annu Rev Cell Dev Biol, 1996. **12**: p. 697-715.
96. Cai, W. and X. Chen, *Multimodality molecular imaging of tumor angiogenesis.* J Nucl Med, 2008. **49 Suppl 2**: p. 113S-28S.
97. Moghimi, S.M., A.C. Hunter, and J.C. Murray, *Long-circulating and target-specific nanoparticles: Theory to practice.* Pharmacological Reviews, 2001. **53**(2): p. 283-318.
98. Canet, E., et al., *Influence of Bolus Volume and Dose of Gadolinium Chelate for First-Pass Myocardial Perfusion Mr-Imaging Studies.* Jmri-Journal of Magnetic Resonance Imaging, 1995. **5**(4): p. 411-415.
99. Kostler, H., et al., *Prebolus quantitative MR heart perfusion Imaging.* Magnetic Resonance in Medicine, 2004. **52**(2): p. 296-299.
100. Lim, C.K., et al., *Nanophotosensitizers toward advanced photodynamic therapy of Cancer.* Cancer Lett, 2013. **334**(2): p. 176-87.
101. Wang, C., L. Cheng, and Z. Liu, *Upconversion nanoparticles for photodynamic therapy and other cancer therapeutics.* Theranostics, 2013. **3**(5): p. 317-30.
102. Agostinis, P., et al., *Photodynamic therapy of cancer: an update.* CA Cancer J Clin, 2011. **61**(4): p. 250-81.
103. Kostron, H., *Photodynamic diagnosis and therapy and the brain.* Methods Mol Biol, 2010. **635**: p. 261-80.
104. Miyazaki, K., et al., *A novel homogeneous irradiation fiber probe for whole bladder wall photodynamic therapy.* Lasers Surg Med, 2012. **44**(5): p. 413-20.
105. Huang, Z., *A review of progress in clinical photodynamic therapy.* Technol Cancer Res Treat, 2005. **4**(3): p. 283-93.
106. Gu, Z., et al., *Recent advances in design and fabrication of upconversion nanoparticles and their safe theranostic applications.* Adv Mater, 2013. **25**(28): p. 3758-79.
107. Idris, N.M., et al., *In vivo photodynamic therapy using upconversion nanoparticles as remote-controlled nanotransducers.* Nat Med, 2012. **18**(10): p. 1580-5.
108. Chen, H.Y., M.M. Rogalski, and J.N. Anker, *Advances in functional X-ray imaging techniques and contrast agents.* Physical Chemistry Chemical Physics, 2012. **14**(39): p. 13469-13486.
109. Zhu, C.F., et al., *Photoluminescence and gamma-ray irradiation of SrAl2O4 : Eu2+ and Y2O3 : Eu3+ phosphors.* Journal of Physics and Chemistry of Solids, 2007. **68**(9): p. 1721-1724.
110. Li, X.F., et al., *New yellow Ba0.93Eu0.07Al2O4 phosphor for warm-white light-emitting diodes through single-emitting-center conversion.* Light-Science & Applications, 2013. **2**.
111. Liu, F., et al., *New Ternary Europium Aluminate Luminescent Nanoribbons for Advanced Photonics.* Advanced Functional Materials, 2013. **23**(16): p. 1998-2006.
112. Dorenbos, P., *Energy of the first 4f(7)-> 4f(6)5d transition of Eu2+ in inorganic compounds.* Journal of Luminescence, 2003. **104**(4): p. 239-260.
113. Poort, S.H.M., W.P. Blokpoel, and G. Blasse, *Luminescence of Eu2+ in Barium and Strontium Aluminate and Gallate.* Chemistry of Materials, 1995. **7**(8): p. 1547-1551.

114. Bao, G. and X.R. Bao, *Shedding light on the dynamics of endocytosis and viral budding.* Proc Natl Acad Sci U S A, 2005. **102**(29): p. 9997-8.
115. Marsh, M. and H.T. McMahon, *The structural era of endocytosis.* Science, 1999. **285**(5425): p. 215-20.
116. Martin, R.B., *The chemistry of aluminum as related to biology and medicine.* Clin Chem, 1986. **32**(10): p. 1797-806.
117. Korsic, M., Z. Giljevic, and D. Kastelan, *[Strontium ranelate--new paradigm in the treatment of postmenopausal osteoporosis]*. Lijec Vjesn, 2006. **128**(5-6): p. 180-2.
118. Sherbaniuk, R.W., et al., *Comparative study of cimetidine and Mylanta II in the 6-week treatment of gastric ulcer.* J Clin Gastroenterol, 1985. **7**(3): p. 211-5.
119. Xin, Y.C., et al., *Bioactive SrTiO3 Nanotube Arrays: Strontium Delivery Platform on Ti-Based Osteoporotic Bone Implants.* Acs Nano, 2009. **3**(10): p. 3228-3234.
120. Ogawa, Y., et al., *Toxicity study of europium chloride in rats.* J Environ Pathol Toxicol Oncol, 1995. **14**(1): p. 1-9.
121. Kim, S., M. Fujitsuka, and T. Majima, *Photochemistry of singlet oxygen sensor green.* J Phys Chem B, 2013. **117**(45): p. 13985-92.
122. Gollmer, A., et al., *Singlet Oxygen Sensor Green(R): photochemical behavior in solution and in a mammalian cell.* Photochem Photobiol, 2011. **87**(3): p. 671-9.
123. Ragas, X., et al., *Singlet oxygen photosensitisation by the fluorescent probe Singlet Oxygen Sensor Green.* Chem Commun (Camb), 2009(20): p. 2920-2.
124. Oh, S.B., et al., *Baicalein attenuates impaired hippocampal neurogenesis and the neurocognitive deficits induced by gamma-ray radiation.* Br J Pharmacol, 2013. **168**(2): p. 421-31.
125. Thariat, J., P.Y. Marcy, and J.L. Lagrange, *[Trends in radiation therapy for the treatment of metastatic and oligometastatic disease in 2010]*. Bull Cancer, 2010. **97**(12): p. 1467-76.
126. Chandler, D.L., *Explained: rad, rem, sieverts, becquerels: A guide to terminology about radiation exposure*. March 28, 2011: http://news.mit.edu/.
127. Alvarez-Lorenzo, C., L. Bromberg, and A. Concheiro, *Light-sensitive intelligent drug delivery systems.* Photochem Photobiol, 2009. **85**(4): p. 848-60.
128. Feldmann, C., et al., *Inorganic luminescent materials: 100 years of research and application.* Advanced Functional Materials, 2003. **13**(7): p. 511-516.
129. Chen, X.Y., et al., *Novel Necklace-like MAl2O4:Eu2+, Dy3+ (M = Sr, Ba, Ca) Phosphors via a CTAB-Assisted Solution-Phase Synthesis and Postannealing Approach.* Journal of Physical Chemistry C, 2009. **113**(7): p. 2685-2689.
130. Carpenter, C.M., et al., *Limited-angle x-ray luminescence tomography: methodology and feasibility study.* Phys Med Biol, 2011. **56**(12): p. 3487-502.
131. Liu, X., et al., *Mixed-Charge Nanoparticles for Long Circulation, Low Reticuloendothelial System Clearance, and High Tumor Accumulation.* Adv Healthc Mater, 2014.
132. Liu, L., et al., *Decreased reticuloendothelial system clearance and increased blood half-life and immune cell labeling for nano- and micron-sized superparamagnetic iron-oxide particles upon pre-treatment with Intralipid.* Biochimica Et Biophysica Acta-General Subjects, 2013. **1830**(6): p. 3447-3453.
133. Liu, Y.F., et al., *Investigation of water-soluble x-ray luminescence nanoparticles for photodynamic activation.* Applied Physics Letters, 2008. **92**(4).

134. Taylor, K.M., W.J. Rieter, and W. Lin, *Manganese-based nanoscale metal-organic frameworks for magnetic resonance imaging.* J Am Chem Soc, 2008. **130**(44): p. 14358-9.
135. Agostinis, P., et al., *Photodynamic Therapy of Cancer: An Update.* Ca-a Cancer Journal for Clinicians, 2011. **61**(4): p. 250-281.
136. Castano, A.P., P. Mroz, and M.R. Hamblin, *Photodynamic therapy and anti-tumour immunity.* Nature Reviews Cancer, 2006. **6**(7): p. 535-545.
137. Dolmans, D.E.J.G.J., D. Fukumura, and R.K. Jain, *Photodynamic therapy for cancer.* Nature Reviews Cancer, 2003. **3**(5): p. 380-387.
138. Juarranz, A., et al., *Photodynamic therapy of cancer. Basic principles and applications.* Clinical & Translational Oncology, 2008. **10**(3): p. 148-154.
139. Lucky, S.S., K.C. Soo, and Y. Zhang, *Nanoparticles in Photodynamic Therapy.* Chemical Reviews, 2015. **115**(4): p. 1990-2042.
140. Fink-Puches, R., et al., *Primary clinical response and long-term follow-up of solar keratoses treated with topically applied 5-aminolevulinic acid and irradiation by different wave bands of light.* Journal of Photochemistry and Photobiology B-Biology, 1997. **41**(1-2): p. 145-151.
141. Muroya, T., et al., *[Photodynamic therapy (PDT) for early cervical cancer]*. Gan To Kagaku Ryoho, 1996. **23**(1): p. 47-56.
142. Walther, M.M., et al., *Phase I trial of photodynamic therapy in the treatment of recurrent superficial transitional cell carcinoma of the bladder.* Urology, 1997. **50**(2): p. 199-206.
143. Lou, P.J., L. Jones, and C. Hopper, *Clinical outcomes of photodynamic therapy for head-and-neck cancer.* Technol Cancer Res Treat, 2003. **2**(4): p. 311-7.
144. Simone, C.B., et al., *Photodynamic therapy for the treatment of non-small cell lung cancer.* Journal of Thoracic Disease, 2012. **4**(1): p. 63-75.
145. Vrouenraets, M.B., et al., *Basic principles, applications in oncology and improved selectivity of photodynamic therapy.* Anticancer Research, 2003. **23**(1B): p. 505-522.
146. Brandis, A., et al., *Novel water-soluble bacteriochlorophyll derivatives for vascular-targeted photodynamic therapy: Synthesis, solubility, phototoxicity and the effect of serum proteins.* Photochemistry and Photobiology, 2005. **81**(4): p. 983-993.
147. O'Connor, A.E., W.M. Gallagher, and A.T. Byrne, *Porphyrin and Nonporphyrin Photosensitizers in Oncology: Preclinical and Clinical Advances in Photodynamic Therapy.* Photochemistry and Photobiology, 2009. **85**(5): p. 1053-1074.
148. Ma, L., et al., *X-ray excited ZnS:Cu,Co afterglow nanoparticles for photodynamic activation.* Applied Physics Letters, 2014. **105**(1).
149. Zou, X.J., et al., *X-ray-induced nanoparticle-based photodynamic therapy of cancer.* Nanomedicine, 2014. **9**(15): p. 2339-2351.
150. Zhang, C., et al., *Marriage of Scintillator and Semiconductor for Synchronous Radiotherapy and Deep Photodynamic Therapy with Diminished Oxygen Dependence.* Angewandte Chemie-International Edition, 2015. **54**(6): p. 1770-1774.
151. Karnkaew, A., et al., *Scintillating Nanoparticles as Energy Mediators for Enhanced Photodynamic Therapy.* Acs Nano, 2016. **10**(4): p. 3918-3935.
152. Chen, W. and J. Zhang, *Using nanoparticles to enable simultaneous radiation and photodynamic therapies for cancer treatment.* J Nanosci Nanotechnol, 2006. **6**(4): p. 1159-66.

153. Sato, Y., et al., *[Merocyanine 540-mediated photodynamic therapy inhibits P-glycoprotein (P-gp) activity in adriamycin-resistant K562 cells]*. Gan To Kagaku Ryoho, 1999. **26**(14): p. 2195-200.
154. Sung, H.Y., et al., *Dcr3 inhibit p53-dependent apoptosis in gamma-irradiated lung cancer cells.* International Journal of Radiation Biology, 2010. **86**(9): p. 780-790.
155. Kim, E.H., et al., *Global analysis of CpG methylation reveals epigenetic control of the radiosensitivity in lung cancer cell lines.* Oncogene, 2010. **29**(33): p. 4725-31.
156. Im, C.N., et al., *Characterization of H460R, a Radioresistant Human Lung Cancer Cell Line, and Involvement of Syntrophin Beta 2 (SNTB2) in Radioresistance.* Genomics Inform, 2013. **11**(4): p. 245-53.
157. Hu, J., et al., *Nanocomposite-Based Photodynamic Therapy Strategies for Deep Tumor Treatment.* Small, 2015. **11**(44): p. 5860-5887.
158. Rogakou, E.P., et al., *DNA double-stranded breaks induce histone H2AX phosphorylation on serine 139.* Journal of Biological Chemistry, 1998. **273**(10): p. 5858-5868.
159. Thrall, D.E., *Biologic basis of radiation therapy.* Vet Clin North Am Small Anim Pract, 1997. **27**(1): p. 21-35.
160. Girotti, A.W., *Photosensitized oxidation of membrane lipids: reaction pathways, cytotoxic effects, and cytoprotective mechanisms.* Journal of Photochemistry and Photobiology B-Biology, 2001. **63**(1-3): p. 103-113.
161. Yasuhara, S., et al., *Comparison of comet assay, electron microscopy, and flow cytometry for detection of apoptosis.* Journal of Histochemistry & Cytochemistry, 2003. **51**(7): p. 873-885.
162. Paull, T.T., et al., *A critical role for histone H2AX in recruitment of repair factors to nuclear foci after DNA damage.* Curr Biol, 2000. **10**(15): p. 886-95.
163. Rappold, I., et al., *Tumor suppressor p53 binding protein 1 (53BP1) is involved in DNA damage-signaling pathways.* J Cell Biol, 2001. **153**(3): p. 613-20.
164. Ferrario, A., et al., *Cyclooxygenase-2 inhibitor treatment enhances photodynamic therapy-mediated tumor response.* Cancer Res, 2002. **62**(14): p. 3956-61.
165. Agarwal, M.L., et al., *Phospholipase Activation Triggers Apoptosis in Photosensitized Mouse Lymphoma-Cells.* Cancer Research, 1993. **53**(24): p. 5897-5902.
166. Yoshizumi, T., et al., *Specific issues in small animal dosimetry and irradiator calibration.* International Journal of Radiation Biology, 2011. **87**(10): p. 1001-1010.
167. Idris, N.M., et al., *In vivo photodynamic therapy using upconversion nanoparticles as remote-controlled nanotransducers.* Nature Medicine, 2012. **18**(10): p. 1580-U190.
168. Montazerabadi, A.R., et al., *The effects of combined treatment with ionizing radiation and indocyanine green-mediated photodynamic therapy on breast cancer cells.* J Photochem Photobiol B, 2012. **109**: p. 42-9.
169. Kavarnos, G., R. Nath, and P. Bongiorni, *Visible-light and X irradiations of Chinese hamster lung cells treated with hematoporphyrin derivative.* Radiat Res, 1994. **137**(2): p. 196-201.
170. Prinsze, C., et al., *Interaction of photodynamic treatment and either hyperthermia or ionizing radiation and of ionizing radiation and hyperthermia with respect to cell killing of L929 fibroblasts, Chinese hamster ovary cells, and T24 human bladder carcinoma cells.* Cancer Res, 1992. **52**(1): p. 117-20.
171. Luksiene, Z., A. Kalvelyte, and R. Supino, *On the combination of photodynamic therapy with ionizing radiation.* J Photochem Photobiol B, 1999. **52**(1-3): p. 35-42.

172. Bernier, J., E.J. Hall, and A. Giaccia, *Timeline - Radiation oncology: a century of achievements.* Nature Reviews Cancer, 2004. **4**(9): p. 737-U15.
173. Begg, A.C., F.A. Stewart, and C. Vens, *GENOMIC INSTABILITY IN CANCER Strategies to improve radiotherapy with targeted drugs.* Nature Reviews Cancer, 2011. **11**(4): p. 239-253.
174. Prasanna, P.G.S., et al., *Normal tissue protection for improving radiotherapy: where are the Gaps?* Translational Cancer Research, 2012. **1**(1): p. 35-48.
175. Wardman, P., *Chemical radiosensitizers for use in radiotherapy.* Clinical Oncology, 2007. **19**(6): p. 397-417.
176. Zhang, C., et al., *Marriage of Scintillator and Semiconductor for Synchronous Radiotherapy and Deep Photodynamic Therapy with Diminished Oxygen Dependence.* Angew Chem Int Ed Engl, 2014.
177. Schweitzer, C. and R. Schmidt, *Physical mechanisms of generation and deactivation of singlet oxygen.* Chem Rev, 2003. **103**(5): p. 1685-757.
178. Bonnett, R., *Photosensitizers of the Porphyrin and Phthalocyanine Series for Photodynamic Therapy.* Chemical Society Reviews, 1995. **24**(1): p. 19-33.
179. Shopova, M., et al., *Naphthalocyanine complexes as potential photosensitizers for photodynamic therapy of tumors.* Journal of Biomedical Optics, 1999. **4**(3): p. 276-285.
180. Houas, A., et al., *Photocatalytic degradation pathway of methylene blue in water.* Applied Catalysis B-Environmental, 2001. **31**(2): p. 145-157.